INVESTIGATION OF GAS METAL ARC WELDING AS A POTENTIAL METHOD FOR ADDITIVE MANUFACTURING OF MAGNESIUM ALLOYS

by

Christoph Andreas Johann Kossack

A dissertation submitted to the faculty of
The University of North Carolina at Charlotte
in partial fulfillment of the requirements
for the degree of Doctor of Philosophy in
Mechanical Engineering

Charlotte

2023

Approved by:

____

Dr. Harish Cherukuri

____

Dr. Haitao Zhang

____

Dr. Youxing Chen

____

Dr. Vincent Ogunro

ABSTRACT

CHRISTOPH ANDREAS JOHANN KOSSACK. Investigation of Gas Metal Arc Welding as a Potential Method for Additive Manufacturing of Magnesium Alloys . (Under the direction of DR. HARISH CHERUKURI)

Gas Metal Arc Welding (GMAW) was investigated as a method for the rapid Wire Arc Additive Manufacturing (WAAM) of magnesium alloys. The GMAW deposition process that was tested was not modified with Cold Metal Transfer (CMT) or short-circuit deposition. High and low input-energy-rate (IER) parameters were established to deposit weld beads with limited spatter and good bead shape. Single-bead multi-layer walls were deposited by a GMAW-CNC using 1.2 mm diameter AZ61a welding wire. These walls were deposited at two different torch travel speeds (TTS) but with the same IER of 1,700 W. The walls were machined into thin walls and wire EDM (WEDM) was used to extract tensile test specimens. Half of the test coupons were extracted so that the tensile test pull force is in-line with the deposition direction and the other half were extracted with the pull force being applied normal to the print direction. For the samples printed at the same TTS, the Instron test results showed high repeatability and a material yield strength (YS) of 116 MPa. The YS for these samples was independent of print orientation, showing the isotropic behavior of the printed material. The samples that were printed at a faster TTS showed the same response to loading conditions, but had a lower YS of 106 MPa, demonstrating how an increase in TTS lowers the YS of welded material. The stress at fracture, however, was almost identical for all the samples, with fractures occurring between 260 MPa and 270 MPa.

Multi-row/multi-layer (MRML) blocks were also printed out of the same material and tested, also with half the samples being extracted normal to the Instron applied load and the other half in-line with the pull force. A higher IER of 2,700 W was implemented to ensure fusion between the overlappping beads. The same isotropic

behavior was observed in these samples but the YS increased in relation to the single wall, low IER samples by over 20 MPa to 139 MPa. Due to the presence of larger internal defects caused by bead overlap issues, the fracture strength range was very spread out, with some normal-to-force samples fracturing at less than 150 MPa and some in-line to force samples fracturing at around 220 MPa. The results for the elastic region, however, fit that of the thin-wall samples.

Scanning Electron Microscope (SEM) analysis was performed on the fracture surface, showing ductile behavior in the fused regions, but also uncovering material defects in the MRML samples such as trapped spatter, trapped air bubbles, and cracks. Optical micrographs were obtained to analyze the microstructure of the samples. A grain refinement from 38 μm pre-weld down to 12 μm post-weld for the MRML samples and a grain refinement down to 28 μm for the single-bead multilayer walls was determined, demonstrating how a reduction of degrees of freedom for conduction heat transfer to occur will result in a larger grain size due to decreased cooling rates.

Multi-layer hollow cylinders were printed to test the ability of the method to produce closed-shape parts. These cylinders were produced at both high and low IERs and yielded parts with post-machining wall thicknesses ranging from 1.5 mm to 4.5 mm. X-ray Computed Tomography (XCT) was performed to determine the porosity of these parts. The three sections analyzed showed a total part percent porosity of 0.04 %, 0.039 %, and 0.07%. Larger individual defects, particularly at the closure-of-bead zone were detected, resulting in maximum single layer %-porosity of 0.8 %.

Finally, a Finite Element Analysis (FEA) model was created to simulate the deposition of the beads and the heat transfer throughout the process. The element activation feature in COMSOL Multiphysics was coupled with the simulated torch path to model the deposition of the material. Heat transfer modes of conduction, radiation, and convection were conditionally assigned to the boundaries of the substrate and of the beads as functions of time and material deposition. The Goldak

double-ellipsoid heat source was used as the primary heating method of the substrate. To simulate the true-to-life GMAW process, where already molten material drops onto the substrate, a bead-heating function was created and applied to the inactive elements of the bead that is being deposited during the simulation. This was done to ensure that the temperatures of the simulated weld droplets are at the correct estimated temperature when they are first activated, after which only normal heat transfer modes impact the temperature of the now active elements. The inactive elements have the assigned properties of air until being activated. The model successfully simulates the thermal-load cycles the part undergoes during the deposition of a 3-by-3 beads block. The results show how in WAAM the layer height is directly correlated to the maximum temperatures seen in the part due to the reduction in directions for heat transfer to occur, with substrate height layers reaching 1300 K and layers 2 and 3 rising to 1500 K and 1700 K, respectively.

DEDICATION

To my wife Hilary and my daughter Sophia.

ACKNOWLEDGEMENTS

Firstly, I would like to thank my research advisor Dr. Harish Cherukuri for his guidance and mentoring of me in my research work and beyond. I am very honored to have been given the chance to work at UNC-Charlotte and make this university my second home.

I also would like to extend my gratitude to the members of my dissertation committee, Dr. Haitao Zhang, Dr. Youxing Chen, and Dr. Tobi Ogunro for their support and willingness to serve on this committee. My gratitude also goes out to my former research advisor, Dr. Joshua Tarbutton, for his guidance while working under his supervision. I also want to thank my future colleague, Dr. Jaime Berez, for his help in obtaining the XCT data for my research.

I also want to thank a group of very special people at UNC-Charlotte that have provided me with assistance while completing my dissertation. I am thankful to Geoffrey Heacock for always taking the time to meet with me when I needed assistance and for the great work he did in the preparation of the tensile test specimens with the wire EDM. I also want to thank Liuqing Yang for working with me in the materials lab on microstructure and tensile test data. Lastly, I want to thank my research partner and friend, Rafi Marandi, for years of support in-and-out of the workplace.

Lastly, I want to thank the Army Research Office for providing funding for much of this research.

TABLE OF CONTENTS

LIST OF TABLES

LIST OF FIGURES

LIST OF ABBREVIATIONS

AM Additive Manufacturing.

CMT Cold Meta Transfer.

CNC Computer Numerical Control.

DED Direct Energy Deposition.

FEA Finite Element Analysis.

GMAW Gas Metal Arc Welding.

GMAW-S Short-Circuit Gas Metal Arc Welding.

IER Input Energy Rate.

LPBF Laser Powder Bed Fusion.

MIG Metal Inert Gas.

MRML Multi-row/multi-layer.

PAW Plasma Arc Welding.

PCTIG Pulsed Current Tungsten Inert Gas.

SAW Submerged Arc Welding.

SEM AScanning Electron Microscope.

SM Subtractive Manufacturing.

SMD Shape Metal Deposition.

TIGW Tungsten Inert Gas Welding.

TTS Torch Travel Speed.

UTS Ultimate Tensile Strength.

WAAM Wire Arc Additive Manufacturing.

WEDM Wire Electrical Discharge Machining.

WFS Wire Feed Speed.

XCT X-ray Computed Tomography.

YS Yield Strength.

CHAPTER 1: INTRODUCTION

With a rapidly increasing global demand for manufactured metallic components, there is a high need for the development of new manufacturing methods that can meet this demand in a cost effective and efficient manner. Alongside these new manufacturing methods, new materials are also gaining increasing attention from manufacturers and industry alike. When it comes to the manufacturing aspect, one of the primary goals is to eliminate unnecessary material waste, which brings benefits in both financial and environmental forms. On the material side, there is great interest in the reduction of the mass of components. Making parts lighter is of great benefit to many industries, especially to the automotive and aerospace sectors, where mass is directly related to fuel costs. This research explores the combination of Wire Arc Additive Manufacturing (WAAM) in the form of Gas Metal Arc Welding (GMAW) and magnesium AZ61a to produce near final net-shaped parts.

The interest to incorporate more WAAM methods in the production process has rapidly increased over the past decade. What makes these methods so attractive is the ability to greatly reduce the amount of material waste that is part of traditional subtractive manufacturing methods. WAAM is a hybrid-manufacturing method and it is not intended to replace any subtractive manufacturing methods. By creating stock material that is almost the same size and shape as the final desired part, it can reduce both the material waste and reduce the amount of required machining, which in turn increases production rates and provides additional cost savings in the form of lower tool wear and machine maintenance.

GMAW is one of the most popular methods of WAAM, due in large part to its low equipment costs, rapid deposition rates, energy efficiency, and limitless achievable build volume. It has been used as a method of successfully additively manufacturing parts out of materials such as steel, aluminum, titanium, and more. When this method is applied directly to magnesium, however, the results have been largely unsuccessful. Even in the initial research stages where GMAW was tested for its usefulness as a simple joining method for magnesium alloys, the results were less than favorable. In order to achieve any usable results, modifications to generic GMAW were developed, such as Cold Metal Transfer Metal Inert Gas welding (CMT-MIG) and short circuit was metal arc welding (GMAW-S). Other methods, such as Tungsten Inert Gas Welding (TIGW) were also tested on magnesium alloys. While these methods showed good deposition results, they are slower than GMAW due to their dipping deposition method, as the wire does not continuously come out of the nozzle, but instead is moved back and forth as the beads are being put down. This makes them not suitable for mass production purposes. Furthermore, these methods have been primarily tested on very thin base metals with thicknesses between 1.6 mm and 3 mm. While base metals with those dimensions might work for single bead joining methods, they would not be usable as substrates for large printed parts due to the potentially very high level of distortion.

This work investigates the ability of standard/unmodified rapid pace DC-GMAW combined with a Computer Numerical Control (CNC) machine to successfully deposit multilayer structures out of magnesium AZ61a. All challenges involved in achieving this goal, of which there are many, are identified and addressed. Parameters for both high and low input energy rates (IER) were established for successful bead deposition on AZ31B substrates. Multi-layer structures in the forms of walls, hollow cylinders, and large multi-row/multi-layer (MRML) blocks were able to be printed, machined into final parts or test samples, and then inspected.

Finite element analysis (FEA) was also performed for parts of the welding process. Simulation of the entire welding process involves capturing the interactions of multiple different physics aspects including thermal, mechanical, and metallurgical analyses. The impact that these individual analyses have on one another is treated mostly as one-directional. That is to say, while the impacts that temperature and heat flow from a thermal analysis have on the displacements and stresses of a mechanical analysis are very high, the impact that mechanical results have on temperatures is very weak. Thermal analysis has the same relationship with metallurgical analysis, where thermal impact on microstructure and phase transformation is very strong, but metallurgical changes do little to the thermal state of a part of model. Lastly, metallurgical results will have a strong impact on mechanical analyses, but the reverse impact is weak. For this reason, to simplify models the weak impacts between these three are typically neglected when modelling the welding process.

The primary goal of this research is to establish a model that can accurately simulate the deposition of material and capture the thermal history of a welded MLMR part so that the resulting thermal analysis results can later be used as input parameters to a structural mechanics simulation, creating a sequentially coupled thermo-mechanical analysis. This type of model is typically created as a 2D simulation due to the many non-linearities that are involved in these models making computation time extremely high and often result in failure of the FEA model due to non-convergence [159]. The deposition-thermal analysis in this work was performed in COMSOL Multiphysics as a 3D model, simulating the deposition of nine weld beads as part of a 3 x 3 beads stacked block.

CHAPTER 2: LITERATURE REVIEW

2.1 Wire Arc Additive Manufacturing

The method of additively manufacturing components has received much attention in the last couple of decades with much research being dedicated to optimizing existing methods as well as developing new technologies. A wide variety of these AM methods are already being implemented by industry and feature a vast combination of material types/forms, heat sources, resolutions, deposition rates, and much more. While many of these methods will be discussed briefly in the following section about AM processes for magnesium, the primary focus of this section is on Wire Arc Additive Manufacturing (WAAM) as a whole. This is a process of the continuous stacking of layers to create a near-net shape final stock part that will require only minimal subsequent machining to get to the final part dimensions.

In the 1990s the utilization of wire-arc deposition processes for the purpose of additive manufacturing started to be investigated. One of the earliest industry applications for this was developed in the mid to late 1990s, when Cranfield University developed a high deposition rate wire-arc method for Rolls Royce, naming it Shape Metal Deposition (SMD) [1, p. 166]. Since then, multiple WAAM methods have been developed and studied, with the primary methods being Tungsten Inert Gas Welding (TIGW), Plasma Arc Welding (PAW), Gas Metal Arc Welding (GMAW), Submerged Arc Welding (SAW), and Skeleton Arc Welding. Some of the materials for these methods that have been studied include steel, titanium, magnesium, nickel, and tantalum. This work focuses exclusively on the combination of GMAW and magnesium to determine if this combination is a possibility to rapidly produce near final net shape parts with minimal defects for industry.

There are many benefits to WAAM, which explains the greatly increasing industry interest in this process. Traditional subtractive-manufacturing (SM) boasts the ability to achieve final part dimensions with incredibly high resolutions. The purpose of WAAM is not to replace these processes, but rather to reduce the cost of the parts by reducing the material that is wasted [2]. SM created parts begin with a standard stock shape, typically rectangular or cylindrical, and then all the unwanted material is removed and turned into chips. These chips are material waste that translates to a financial loss, an especially large financial loss if the component's raw material is very expensive. By creating a stock material that is almost the same final shape as the desired part, this waste of material and money is reduced. Decreases in machining time further increase the cost saving benefits as tool and machine life would be extended considerably.

A further cost saving aspect of WAAM is the required costs of the involved machinery. Especially when comparing WAAM to other AM processes it becomes evident that the costs are much lower due to the lack of requiring a vacuum environment and expensive heat source equipment [2,3,4]. Generic welding equipment can be used as the heat source for most of these processes. Due to the presence of shielding gas, there is no need for a permanent enclosure with environmental controls. Instead, the process provided shielding gas into the deposition area is all that is required to ensure that impurities do not cause porosity and losses in material strength. This also means that there are virtually no size limitations for parts. You are only limited to the size of available substrates and the range of the CNC machine or robotic system. Of course, one needs to keep in mind that the printed part size should not exceed the maximum volume availability of the SM machine that is being used to get the part to its final shape.

As previously stated, generic GMAW is the focus of this work. Modifications to this method, including short circuit GMAW (GMAW-S) and cold metal transfer MIG welding (CMT-MIG), will also be discussed, especially in relation to their use in Mg-AM. GMAW is typically the preferred method of WAAM. With the weld wire being the electrode and being extruded straight out of the weld nozzle, it makes deposition path planning less complicated than with other WAAM methods. The deposition also happens at a rapid pace, with Han et al. showing that material deposition rates of up to 4.71 kg/h are possible with GMAW [5]. Methods for controlling the arc via controlled short arc welding further improves the process by reducing the already low energy required for deposition [5,6].

The introduction of CMT-MIG welding by Fronius has greatly improved the control of deposition for GMAW-AM [2]. This method implements a dip transfer process, where the filler metal moves in and out of the weld pool at very low input current. This dipping method, as well as the very low current (almost zero at times), provide more control when depositing material. GMAW-S employs a similar strategy as the weld wire is plunged into the weld pool causing a short and is then retracted out of the weld pool as the arc is reestablished.

Much work is also going into the optimization of input parameters for these methods. For GMAW, these parameters include input voltage/amperage, distance to work offset, wire feed speed (WFS), travel speed, overlap percentages, layer heights, and more. Most of these input parameters are established through a method of trial and error, as modelling of these processes is extremely challenging. Some prediction models are still being developed though. A more knowledge-based approach for determining these parameters was created by Hu et al. [7,8], while working on determining the optimal distance for weld seams (overlap). The model predicts that an overlap of 0.63-0.77 times the weld bead's width would be optimal for multi-row deposition. A great paper summary of other parameter optimizations can be found in [1, p. 216]. It was shown that faster travel speeds, along with a constant heat source, will result in narrower melt regions, leading to lack of fusion due to melting no longer occurring.

The continuity of the weld pool is crucial to create fully dense parts. However, an increase in the size of the melt pool also means that the heat input could become excessive. This will increase the solidification stress and, by extension, the distortion of the part, resulting in further accuracy losses. Other defects and process interrupting occurrences such as voids, cold shut, spatter and vaporization can also be caused by too high of a power density. There is a very fine line between too hot and too cold, especially when it comes to magnesium, which will be discussed later in this section. The following paragraphs discuss the challenges that must be faced when working with WAAM processes.

There are many challenges that come with WAAM. Defects in the forms of distortion, porosity, cracks, and delamination can have a detrimental effect on the quality of the final part. All parameters must be perfectly matched with one another to ensure a part that will provide the desired properties. Residual stresses are always present in WAAM fabricated parts, but can be greatly reduced by optimizing weld paths and interlayer cooling rates. [4]. Post weld heat treatments can also be used for reducing these stresses even further. One of the primary culprits for these stresses is the uneven temperature field distribution and the inconsistent cooling during the solidification phase. Szost et al. [9] showed that the maximum residual stress appears at the bottom of the forming layer. When stacking multiple layers, each layer will have a second melting section where these stresses are added as well. The distortion due to these stresses can sometimes go unnoticed until the part is unclamped, which can lead to further complications. It is the shrinkage of the deposited material during cooling that pulls the material together [10]. Additional methods for reducing this distortion are summarized in [2] and include symmetrical building, back to back building, optimizing part orientation, and high pressure interpass rolling, the latter of which will be presented further down in this section.

Porosity shows up in small to medium size voids that are either internal or on the surface of the welding beads. These voids decrease the density of the part and decrease its strength as it is more likely to fail due to crack propagation. Many things can have an impact of the level of porosity in WAAM parts. Even the flow rate of the shielding gas can have a negative impact on pore diameters, as shown by Cong et al. [11]. It was also found that the pores were mainly distributed in the interlayer remelting area, but they can also be present in any portion of the beads. Porosity is an even greater problem when working with magnesium, which will be explained in detail in a later section.

Predicting the layer height of the deposited material is crucial in determining the nozzle offset but standards for predicting the required changes in the vertical build direction for each subsequent layer have yet to be established. Not only do additional layers not always add the same amount of material in the upwards direction due to inconsistent flattening effects in the bottom layers, but the horizontal height along the beads is not consistent as well. Zhang et al. [12] studied this behavior and noted a difference in height between the starting end and the arc extinguishing end. This difference increases as the number of layers go up, as will be seen in this research as well. A stagger pattern was proposed when building up multiple layers [12]. This, however, is only applicable in certain situations, as will be addressed in this study. Closed shaped prints require a different method, as stacking is not possible. Xu et al. [13] proposed another method to overcome uneven previous welds or substrates by choosing the deposition rate as the signal and the travel speed as the variable value. This is also not without challenge as the travel speed, energy input and filler feed rates need to be continuously balanced in real time. The previous examples dealt with deposition in the vertical build direction, but for thicker parts the horizontal spacing, or overlap, also greatly impacts the height of the combined layer, as shown by Plangger et al. [14] when working with deposition of high strength steel.

Choosing the appropriate weld speed not only impacts the power density input and layer penetration, but it also can result in unfavorable surface quality, intermittence, and humping of the weld bead. Particularly in high speed deposition, humping in a bead is very common and will result in an extremely uneven surface profile. It was shown by Soderstrom and Mendez [15] that it is the back flow momentum of the melt that causes this phenomenon to occur. The result is a large mass on the upstream side of the bead followed by a thin connecting section until the bead returns to its normal shape. The maximum allowable welding speed depends on the material and the method being used. Adebayo et al. [16] showed that 60 cm/min is the maximum travel speed that can be achieved without humping occurring.

Another crucial component in GMAW-AM is path planning. Not only does this impact the geometrical accuracy of the part, but also impacts thermal management and consequently can reduce residual stresses and distortion [17]. Incorrect movement from CNCs or robots can cause many problems and can cause large differences in layer heights. This is especially true around corner situations, as the travel speeds will vary [18]. Thermal management in AM parts is the primary difference between simple joining welds and creating multilayer parts [19-21]. When welding two plates together, the heat transfer is in multiple dimensions. However, if a part is being built upwards, the number of directions the heat can travel gets severely cut down [20]. The heat now does not immediately go into the larger substrate, but rather through the previously deposited layers, changing their thermal history.

The development of cracks in WAAM parts is a big possibility if all parameters have not been balanced with one another. Solidification cracks and liquefaction cracks are a frequent occurrence [4]. Some cracks occur during the solidification phase as the beads try to shrink but are restricted to do so. Warping in the substrate can further increase the cracks and even result in delamination from the substrate of from lower beads. Delamination, however, is most common only in the joining of dissimilar metals.

Other challenges include issues with arc wondering, surface finish, and many more. In WAAM, the arc is established between the base and the electrode. In the case of GMAW, the electrode is also the consumable. It is not guaranteed that the arc will always start pointing straight down underneath the torch. There is a possibility that it wonders across the part, especially if subsequent layers are not a consistent distance from the nozzle. This will of course also impact the surface finish of the part. Large weld pools from high deposition rates especially will provide coarse deposition features and irregular surfaces [1, p. 218]. The viscosity of the melted material also plays a large part in the quality of bead and surface finish one will obtain. This is especially true with magnesium and its very low sup-melting viscosity, as will be shown in this research.

Quality improvement methods have been developed by many researchers over the past decades to reduce these challenges. Reducing the residual stresses and improving mechanical properties is made possible by implementing the proper post weld head treatment (PWHT). Interpass cold rolling is another method that can break coarse columnar crystal structures and improve the strength and hardness of the part [4]. Interpass cooling is another parameter that needs to be taken into account, as it has one of the biggest impacts on the thermal history of the part. Finishing treatments post deposition in the form of peening and ultrasonic impact treatments are also commonly being applied to WAAM parts [4].

2.2 Magnesium in manufacturing

Magnesium has become a material of great interest due to its excellent strength-to-weight ratio. The demand for magnesium has been increasing on a yearly basis for the last couple of decades. With magnesium alloys having a density below 1.8 g/cm^3, it is far lighter than other metals used in industry. Compared to other commonly used metal alloys, it has a density 65% that of aluminum, 38% that of titanium, and 25% that of steel [22].

This quality makes the material especially attractive to the automotive and aerospace industry, where is it already utilized. Multiple auto manufacturers are already including magnesium in many of their components, including front end structures, transmission cases, cam covers, center consoles, bucket seat frames, instrument panels, and more [23]. Magnesium parts are also used in helicopters and airplanes. ZE41 castings of transmissions are included in the UH60 Family Blackhawk helicopter and EZ33A castings are used in the Rolls Royce RB211 airplane gearbox [24]. Even with highly increasing demand, there is limited research in the AM of magnesium, even though the number of published research papers per annuum is increasing drastically.

There are many methods available for the manufacturing of Mg alloys, including casting, laser-powder-bed-fusion (LPBF), sintering, friction-stir processing, inject methods, and WAAM [22]. It can be argued that due to the method of energy/heat input, the method closest to WAAM is laser-powder based AM. Mg-LBPF is not without its challenges either. One of the characteristics that makes magnesium difficult to work with is its very low evaporation temperature, which is around 1,091° C . That is less than half that of aluminum at 2,470° C and only a third that of titanium, which has a evaporation temperature of 3,287° C [22]. When working with alloys such as AZ91 for example, the difference in evaporation temperature of the two metals makes the process very challenging [25]. Even more challenging is establishing a trend between process parameters and porosity, and so far, no standard has been determined. There are also dangers involved with the handling of Mg powder [22]. Oxidation, evaporation and the reactive nature of Mg have raised many health concerns.

2.3 Mg-WAAM

TIGW and GMAW are the main contenders for Mg-WAAM. Both have been shown as possible methods, with Goe et al. [26,27] showing success with TIGW and Gneiger et al showing good results with the short-arc GMAW method for manufacturing AZ61

[28]. This section covers the current research and results for Mg-WAAM.

Just like with other materials, WAAM allows for high deposition rates, even for Mg alloys. This is especially true compared to LPBF, where the equipment costs are also considerably higher [22]. Safety risks compared to LPBF are also significantly reduced as the build mater is in wire form instead of powder. Lower costs in feedstock material production and its storage are also true for WAAM when compared to LPBF.

Interestingly, it has been determined in the review by [22] that MIG and TIG in their generic states are not suitable for Mg deposition due to excessive heat output and issues with warp and meltback. Instead, modifications to these processes must be used to achieve Mg deposition. While these concerns are indeed valid, this research will show that GMAW is still capable of achieving quality printed Mg parts. The CMT-MIG method is described as the most favorable method for this process.

Even with CMT-MIG showing promise, WAAM of Mg to date are not very common. One of the reasons for this is the simple lack of availability of magnesium wire, something which was an issue in this research as well. Very few papers exists on Mg-WAAM and the number of different filler materials is even lower. The most common researched magnesium wires are AZ31, AZ61, AZ80, AZ91, and AEX11, with AZ31 being the most studied [29,30,31,32,33]. Another challenge for Mg-WAAM is that it should be performed at relatively low currents as to not over-melt or vaporize the material. In MIG welding, the welding current and the wire feed speed (WFS) are coupled, leading to insufficient wire feed speed when attempting to deposit at currents under 60 A [22]. Additionally, humping defects are also more common at higher torch feed speeds [34,35]. This is especially true due to the fluidity of the metal. In order to prevent humping, lower torch speeds must be maintained. The low density that makes Mg so attractive to manufacturers is also another reason it makes its use in WAAM a problem. When the wire is melted, the globule does not want to separate from the wire and tends to form larger droplets than with conventional materials

[36], which leads to spatter problems and shorts when it finally does drop towards the substrate.

The limited data that does exist for Mg-GMAW is primarily for joining processes and not for AM purposes. Experiments on buck joints were performed in [37], where AZ31B was used as moth substrate and filler material. The substrates were 200mm x 80mm x 1.6mm, and the buck joint was used to weld these plates together. The mode of transfer in this experiment was spray transfer, the distance to the workpiece was 15 mm and the constant voltage was set to 26.5V. Experiments were performed with WFS between 100 to 200 mm/s and combined with torch travel speeds between 6.7 mm/s to 10 mm/s. Dogbone tensile test specimens were then machined out of the joined plates, making the buck joint the testing area, and tensile test results showed a tensile strength of 278 MPa. The authors also noted that at high travel speeds, porosity became an issue because due to insufficient time, the bubbles in the weld pool could not escape before final solidification. At lower travel speeds, the bubbles could escape, but conversely there was more evaporation of Mg and Zn, which increased the chance of more bubbles in the weld pool.

Mg-GMAW for joining purposes for AZ61a was examined in [38], making it the only paper attempting the same thing as this research. However, the author in this case was not successful in implementing GMAW and instead had to rely on CMT-MIG to achieve the desired results. The problem the author faced, however, are very valid and have been encountered in great amounts in this research as well. Another important thing to note is that in [38], as well as in [37] and all other Mg-WAAM papers, the substrates used for deposition are extremely thin, measuring from just above 1 mm to 3 mm. This allows for a much lower heat input as it is easier to penetrate the substrate, but will also lead to extreme warping when used in AM processes. The author in [38] notes the extreme spatter and irregular weld bead shapes encountered when using GMAW on Mg. They were unable to establish spray transfer of any kind without using very high welding current, which as previously stated is not desirable for Mg deposition. The author does note that generic TIGW could be used for this process, but it has a much lower production rate and requires a high level of skill.

The substrate used in [38] was a AZ61B-H24 plate measuring 203mm x 76mm x 1.6mm. The wire was a 1.2 mm diameter AZ61a feed wire. Both of these were examined in the current study. For their GMAW experiments, they chose a WFS of 122 mm/s, a torch travel speed of 7.6 mm/s, a working voltage of 19 V, and a nozzle to workpiece offset of 12.7 mm. The shielding gas they used was 100% argon flowing at a rate of 275 cm3/s. These experiments were completely unsuccessful. The process suffered from extreme spatter issues because it appeared that due to their parameters, the separation of the droplet from weld wire was not regular. Sudden current surges cause by this phenomenon were responsible for inconsistent bead shapes as well as the excessive spatter reported. The author does note that the volumetric heat of fusion and volumetric specific heat differences between aluminum and magnesium is very significant, due to the differences in specific heats, heat of fusion, and density between the two materials. The volumetric heat of fusion for Mg is 626 Jcm^{-3} while it is 1075 Jcm^{-3} for aluminum. The volumetric specific heat for Mg is 1.7 $Jkg^{-1}K^{-1}$ while it is 2.46 $Jkg^{-1}K^{-1}$ for aluminum. The authors also noted the issues with the purchase wire, as it was riddled with defects and oxidation problems. This was encountered in this research as well and required a considerable amount of pre-weld cleaning of the wire by hand. This also had a great effect on porosity, which was observed in both CSC-GMAW and GMAW in [38].

Ying et al. and Rose et al. [39,40] studied the impact that welding parameters have on AZ61a microstructures, porosity and tensile strengths, with Gas Tungsten Arc Welding being performed by [39] and Pulsed Current Tungsten Inert Gas Welding (PCTIG) being used by [40]. Pre-weld, AZ61a has a yield strength (YS) of 217 MPa, a ultimate tensile strength (UTS) of 271 MPa, and an elongation of 8.14% [40]. It should be noted that in most material reference catalogs, the YS of AZ61a is given to be more in the range of 227-230 MPa. Ying et al. performed their experiments by selecting a range of welding currents between 130 A and 160 A, in increments of 10 A, and coupled those with a range of weld voltages from 12.6 V to 15.6 V, in increments of 1 V. The experiment showed that as the heat input increased, the number of defects in the material also increased, with porosity rising from 0.029% at 130A/12.6V to 0.569% at 160A/15.6V. The size of the defects also showed the same trend. At 130A and 150A, the defects were around 0.02 mm-0.1 mm in diameter, while at 160A, the diameter size rose to between 0.02 mm to 0.2 mm. Their microstructure analysis showed that there were mainly equiaxed grains with different grains sizes. The smallest grain sizes were present in the lower current deposition methods, with the 130A and 150A currents producing grains sizes of 22.0 μm and 25.1 μm, respectively. The grain size rose to as high as 45.2μm with the 160A current. The strength of the material was tested next and revealed similar results. The YS of 130A and 150A currents was 105 MPa and 104 MPa, respectively with UTS values of 260 MPa and 256 MPa. The 160 A sample not only had the lowest YS, but also fractured at a much lower stress of around 185 MPa. As can be seen by these results, there is a considerable drop in material strength after undergoing the WAAM process. It should, however, be noted, that no post-weld material treatments were performed on the samples. These results are applicable for comparison to this research because even though a different welding method is utilized, the samples and tests were performed on specimens take out of a whole AM block, and not just from a joining operation. Ying et al. also utilized the same wire material as was used in this research, AZ61a.

Rose et al. [40] performed their analysis by creating tensile test specimens through the joining of two AZ61a plates via PCTIG. The plates and dogbone thickness for these tests was 6 mm. PCTIG is considerably different from GMAW, not just due to the fact that the filler material is not also the electrode, but also because the current in this process oscillates greatly. In this experiment, multiple peak/base currents were tested and at different frequencies. The peak currents ranged from 140 A to 180 A and the base currents had a range of 60 to 100 A. The pulse and base currents are coupled as they increase in increments of 10 A. Their tensile test results showed a wide range of current/frequency dependent YSs, going from 112 MPa all the way up to 195 MPa. These YS values far exceed those obtained by [39]. As will be seen in later section, the YS strengths obtained in this study are in between those results, at around 135 MPa. Unlike [39], it was found that a combination of peak current and base current right in the middle of the test range was the optimal solution to gain the highest YS: 160A/80A. The microstructure that yielded this superior YS also showed the smallest grain size.

2.4 Finite Element Analysis of the Welding Process

As stated in Chapter 1, modelling of the welding process is a complicated matter as it is a Multiphysics endeavor. As such, most simulations will model each of the three physics problems, thermal-mechanical-metallurgical, separately and then use the individual simulation results as input parameters for other models. Additionally, these models are typically 2D in order to simplify the model and reduce computational time. Most models that implement a 3D geometry focus on the deposition of single beads.

Adib Becker [41] provided a cumulative set of requirements and challenges for modelling welding operations in his National Agency for Finite Element Methods and Standards (NAFEMS) seminar series. Thermal material properties of conductivity, specific heat, coefficient of thermal expansion, and melting temperature, for latent heat of fusion, must be applied and their dependence on temperature should be recognized. Heat source geometries in the form of 2D Gaussian distribution, 3D conical distributions, and double ellipsoidal distributions have been implemented in past works. The limitation and validity of available data to successfully complete such simulations is also pointed out as a potential problem. The material properties must be accurate for large temperature ranges. The assumptions made for simplification purposes of the models must be highly scrutinized and hard to analyze experimental portions of the weld beads must be investigated to ensure realistic model results. Simulations of multi-bead depositions are especially difficult due to the cyclical thermal loading of the deposited material and the substrate.

Ogino et al. [42] created a 2D model that simulates the GMAW process from the applied heat source to the weld pool formation. This model was primarily interested in the physical formation of the weld pool and included the flow field in molten metal and the weld pool surface deformation. From the simulation they were able to extract the temperature impact from the weld pool had on the substrate in immediate vicinity of the heat affected zones (HAZ). The computed temperature ranged from up to 1800 K in the weld metal to 900 K at the edge of the HAZ a few millimeters away. The numerical model for this simulation was provided by [128]. The volume-of-fluid (VOF) method was used to keep track of the shape of the free surface by prescribing a fractional value to each cell in a grid, describing the percentage of fluid and/or gas in the cell. The continuum surface forces model was used to calculate the surface tension forces. For boundary conditions, they assumed both the substrate and the torch to be stationary.

Goldak et al. [43] created the heat source that was applied in this research. Many heat sources used in welding simulations feature a Gaussian distribution of energy density of a circular heat source, but the Goldak model proposes a double ellipsoidal geometry to more accurately capture the energy input. What makes this heat source so versatile is that the power density distribution can be adjusted for multiple parts of the heat source. Alterations can be made not only to the penetration depth, but different dimensions can be assigned to the front and the back of the heat source, as well as to its width. The result is a HAZ that has the shape of a typical weld bead when it penetrates the substrate. The validation of the model was achieved by comparing cooling time differences between simulation and experimental data for a single bead. Results showed that while other analytical models suffered from a 41 percent different when compared to experimental data, the Goldak model only resulted in a 5 percent difference. More detail on how this model is structured and is implemented is presented in Chapter 5.

A five module GMAW model was created by Grujic et. al [45] to simulate the deposition of martensitic steel. This model included independent module of the weld-gun, the electric-arc heat source, the thermo-mechanical process, microstructure evolution, and microstructure/property relationships. The heat source in this case was of a circular type with a assigned heat flux distribution that was a function of diameter and total energy input. It should be noted that no deposition was modelled in this simulation and all the material involved was active at all times and then had the heat source applied to it as it passed along the weld direction. Since no additional elements had to be created and only one bead was simulated, the boundary conditions for the model did not have to be time dependent as far as element activation was concerned. The final results of this model managed to clearly establish all zones of the weld region and even managed to identify separate zones with fine and coarse grain sizes.

Zacharia et al. [46] developed a 2D and 3D model for coupled conduction and convection heat transfer that are associated with both stationary and moving arc welding heat sources. Both heat and fluid flows in the weld pool were simulated for the weld pass. The model itself had three layers, with the middle layer being the metal and the top and bottom layer being argon gas. Boundary conditions for the bead and base were assigned to the side, top, and bottom surfaces of the model geometry. These thermal boundary conditions include radiation and convection. They keyhole development in the base material and the creation of the HAZ zone was successfully modeled, showing a direct impact on surface temperature up to 1.5 cm away from the heat source.

A WAAM process model was developed by Montevecchi et al. [47] in 2016. This simulation includes the Goldak model as a heat source as well. They go by the assumption that the power consumed for melting the weld wire is 50 percent that of the total input power. For deposition, they used the quiet-element method in which the elements are always present, but prescribed low values for thermal properties as to not interfere with the solid material surrounding it which is of interest. They activate elements as a function of temperature. Their solution to avoid simulation instabilities when activating elements is to allow the material and thermal properties to switch over a prespecified range of temperature. Boundary conditions of convective and radiative heat transfer were assigned to all surfaces of the model.

CHAPTER 3: MAGNESIUM GMAW-AM

3.1 Gas Metal Arc Welding

GMAW was developed in 1948 and has been one of the most popular forms of welding in history. This is largely due to its versatility and fast deposition rates. The process is relatively simple. A wire feeder pushes and/or pulls wire off a spool and into a weld hose. The wire can come in different materials and diameters. The weld hose connects the power source to the weld torch. The wire travels down a wire diameter specific PLA liner inside the hose, goes into the torch and gets fed through the contact tip. There are two additional lines inside the welding hose: the current conductor line and the shielding gas line. The former puts a charge on the contact tip, which transfers it to the wire, which is the consumable electrode for the process. The shielding gas line supplies user-controlled amounts of gas to protect the weld pool during the deposition process. The substrate, or base material, to be welded on is grounded back to the power source. When the welder is started, an arc ignites between the consumable electrode and the substrate once the wire gets close enough. The heat from the arc melts both the weld wire and the substrate. Most of the heat penetrates the substrate, creating a melted pool of material. The rest of the heat generated melts the wire itself. As melting occurs, the material turns into a droplet on the end of the weld wire, and when that droplet is heavy enough it falls into the weld pool below. The torch must be moved along at a constant speed to ensure even deposition. The combination of wire feed speed (WFS) and torch travel speed (TTS) determines the overall size of the bead. An image depicting the in-process GMAW deposition from this research is shown in figure 3.1.

Most commercial MIG welders come with a variety of optimized presets for different

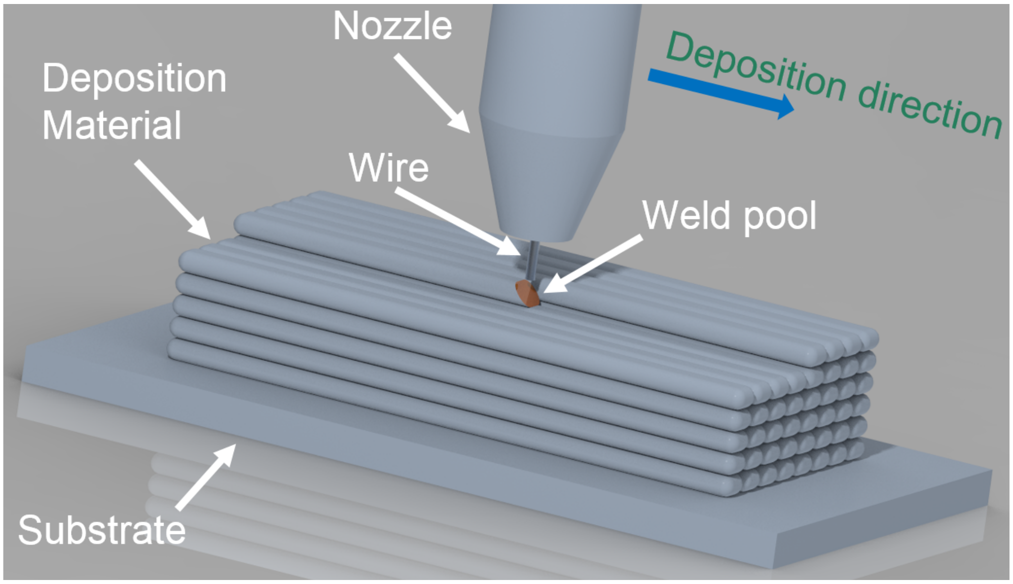

Figure 3.1: Gas Metal Arc Welding process showing the extrusion of the filler material out of the weld nozzle towards the weld pool.

combinations of wire material, welding methods, and wire diameters. Users can optimize these settings for any welding condition by raising or lowering the voltage and/or the current for the process.

3.2 GMAW-CNC

The unpredictable behavior of magnesium when deposited via the GMAW method poses many dangers to operators as well as machinery. The initial research proposal called for all deposition tests to be performed in the build chamber of a 5-axis Mori Seiki CNC machine. However, due to the potential risk to this machine due to severe spatter and potential fire, a prototype of a 3-axis CNC welding machine was built first. The lack of ventilation in the Mori Seiki was also not taken into account and could have resulted in severe physical damage to machine operators as there was no possibility of including a fume extractor inside the closed build chamber. Figure 3.2 depicts the welding CNC that was designed and built. The primary structure is composed of custom cut aluminum t-slotted extrusion framing. BK/BF12 support blocks and bearings were attached to the frame to support the RM1605 ball screws.

The ball screws, along with linear rails, enable motion of the weld torch in three dimensions. Two high torque Nema 23 stepper motors were installed to the primary axis (X-axis) to ensure a smooth and rigid ride of the main carriage during the welding operation. Two custom connectors were designed, and 3D printed to connect the ball screw to the primary carriage of the machine. The Y and Z axes were outfitted with one Nema 23 CNC stepper motor each.

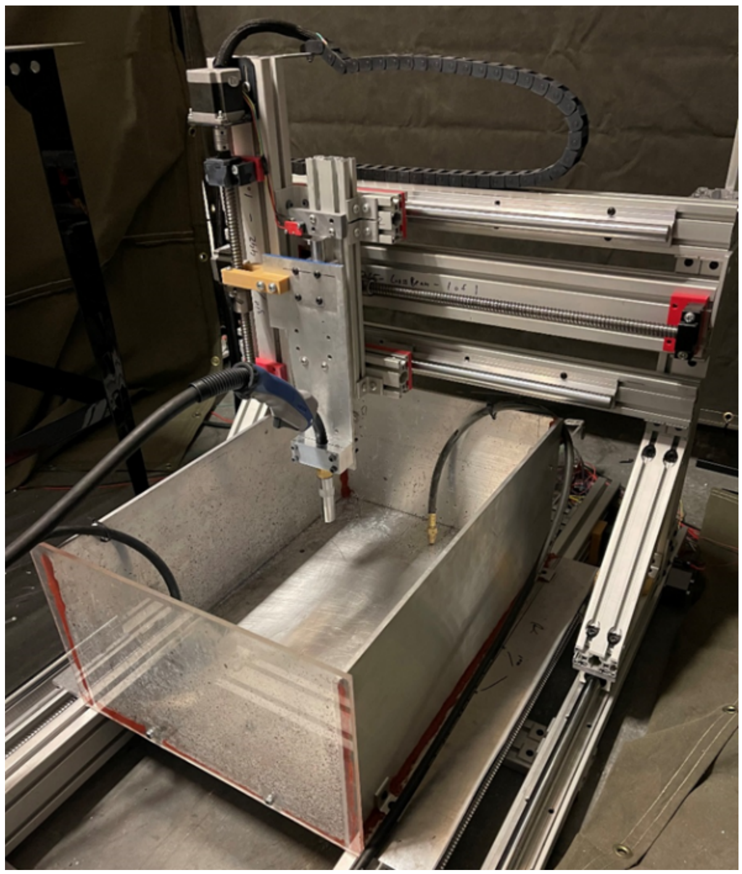

Figure 3.2: GMAW-CNC with protective enclosure, argon flooding hoses and integrated Blue Torch III welding torch.

A custom enclosure, measuring 90 cm x 50 cm x 40 cm, was built out of 6061 aluminum to protect the machine and surroundings from the expected spatter. The front panel of this enclosure was constructed out of acrylic in order to obtain direct video footage of the welding process while protecting any camera equipment. The bottom plate of the enclosure was designed oversized so that it extends over the ball screws of the X-axis as a protective cover in the case that violent spatter escapes the walls of the enclosure. The enclosure is also raised off the ground and supported by two isolated t-slotted crossbeams to ensure that there is no extreme heat transfer into the main machine and to allow for forced convection cooling on the bottom of the enclosure. Two hoses connected to a separate argon gas cylinder were also placed on opposite ends of the enclosure to enable the flooding of the build chamber with gas. These were used only in a couple of tests and did result in superior weld behavior. However, due to the process requirements it was deemed not financially feasible to include the gas for all the tests performed. A custom connection plate to mount the welding torch to the vertical Z-axis of the machine was fabricated out of a 6061-aluminum plate, along with a two-piece clamp block machined out of 6061 blocks. The block could be attached to the plate through multiple different hole-sets so that the torch angle could be manipulated. A perfectly vertical torch position, however, was the only tested method during this research. An additional clamping system was designed and built for a second torch attachment and is shown in figure 3.3 on the right.

The control box was designed and manufactured out of acrylic and installed behind the machine. During welding operations, it was also covered with a fire-proof blanket for extra protection. A Mach3 USB was used as the controller. In addition to the motor drivers, a manual emergency-stop and a relay trigger were wired to the controller. The relay trigger was wired into the welder to activate the deposition process by simulating a pressed torch trigger. This was easily activated with the correct G-code. An array of cooling fans was installed behind the machine as well, which provides the forced convective cooling as previously mentioned. A face plate is installed at the back of the control box to ensure that the fans don't pull air across the controller and covering it in dust and debris. The control box and the fan-array can be seen in figure 3.3 as it was being built.

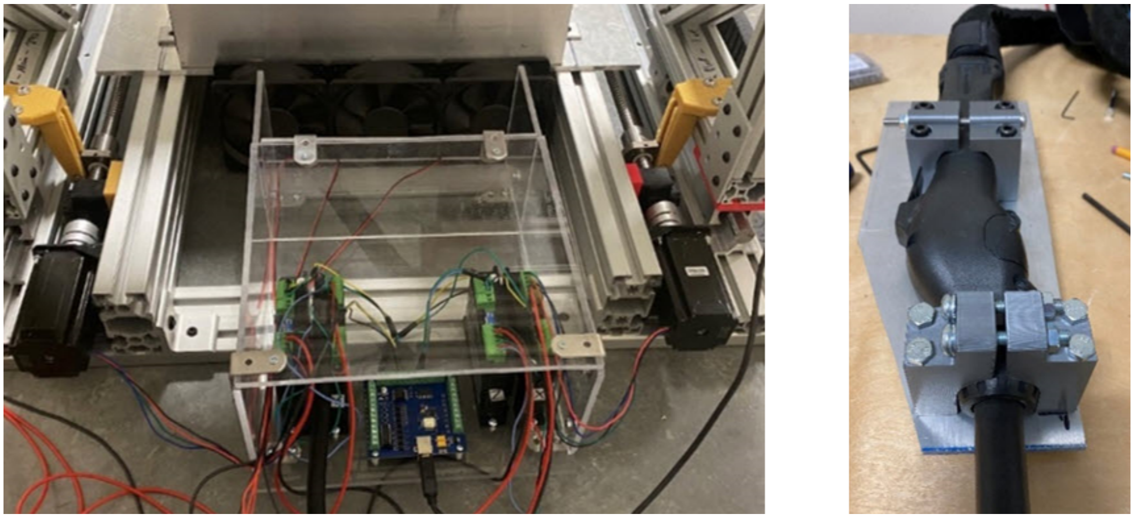

Figure 3.3: CNC acrylic controller box with stepper drivers and Mach3 USB control board and interpass cooling fan array behind it (left) and face-plate attachment brackets for the welding torch(right).

The substrate for deposition is clamped to the bottom enclosure by two 11 mm thick aluminum beams, which are bolted down to the desired grip strength. Grounding of the substrate can be achieved in a variety of ways. Initially, a grounding clamp post that was machined was placed between the clamps and the substrate. Later, grounding was also achieved by clamping directly to the substrate clamp crossbeams or to a grounding block attached to the bottom of the enclosure.

Two different welders were tested in this research. Initially, the MillerMatic Alumapro was used for base line test with aluminum and then experimental test with magnesium. While this machine performed perfectly for the aluminum alloys it was optimized for, it struggled greatly with the magnesium wires that were being tested. The Welbee P400 from Daihen OTC was then purchased and used for all subsequent tests. This machine was initial chosen due to it custom operational setting (OP) which allows for user specific parameter inputs for wire material. Unfortunately, it turned out that these OP settings are locked, and OTC was not willing to let us manipulate the system outside of the factory. For this reason, the Hard Magnesium material settings had to be used on the inverter, which as will be seen in the following sections, was problematic. The wire feeder was modified with an aluminum friendly set of rollers to ensure for better feeding of the material. The Welbee P400 setup and substrate clamping in the machine are depicted on the left and right side of Figure 3.4, respectively. CAD models of the machine are shown in Appendix D.

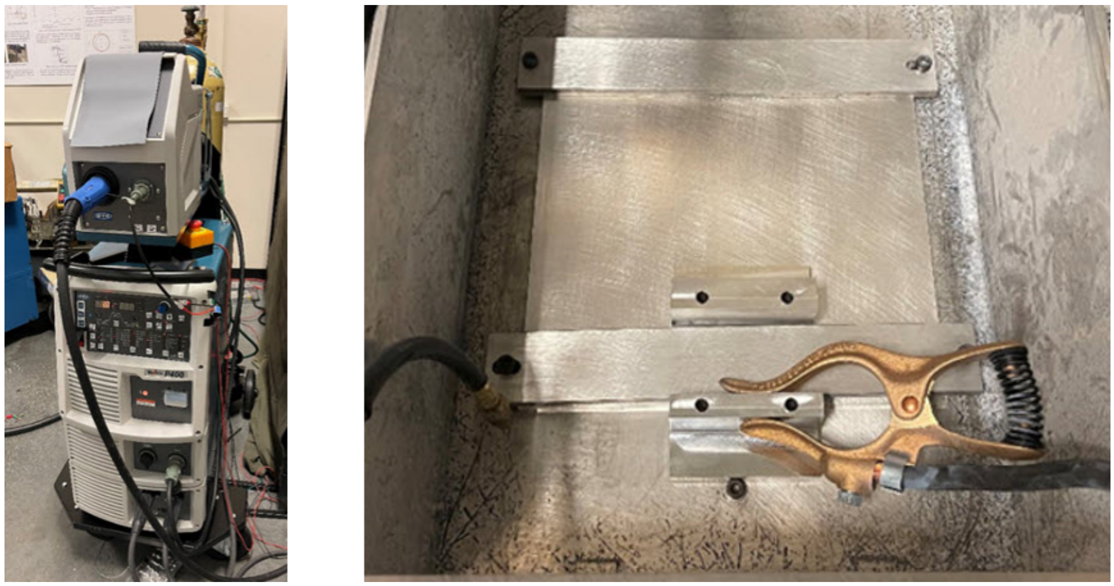

Figure 3.4: Daihen OTC Welbee P400 Inverter with attached wire feeder and argon cylinder (left) and clamped substrate inside the CNC enclosure with grounding clamp (right).

3.3 Magnesium deposition

3.3.1 Challenges in Mg deposition

The following paragraphs give detailed descriptions of all the challenges that are involved with applying GMAW to magnesium alloys, of which there are many. The most glaring problem in achieving this process successfully is the lack of properly calibrated equipment and the lack of quality deposition wire.

The lack of properly manufactured and stored magnesium wire has been a problem for many years, and has been noted by the welding research institute [101]. In fact, most research conducted with magnesium wire these days involves the in-house production of magnesium wire via the extrusion process. The limited availability of the wire, especially of AZ61a, made this research the most challenging. There are two main problems with the wire: 1.) it has been improperly stored and suffers from extreme oxidation, and 2.) the wire drawing process was not properly performed.

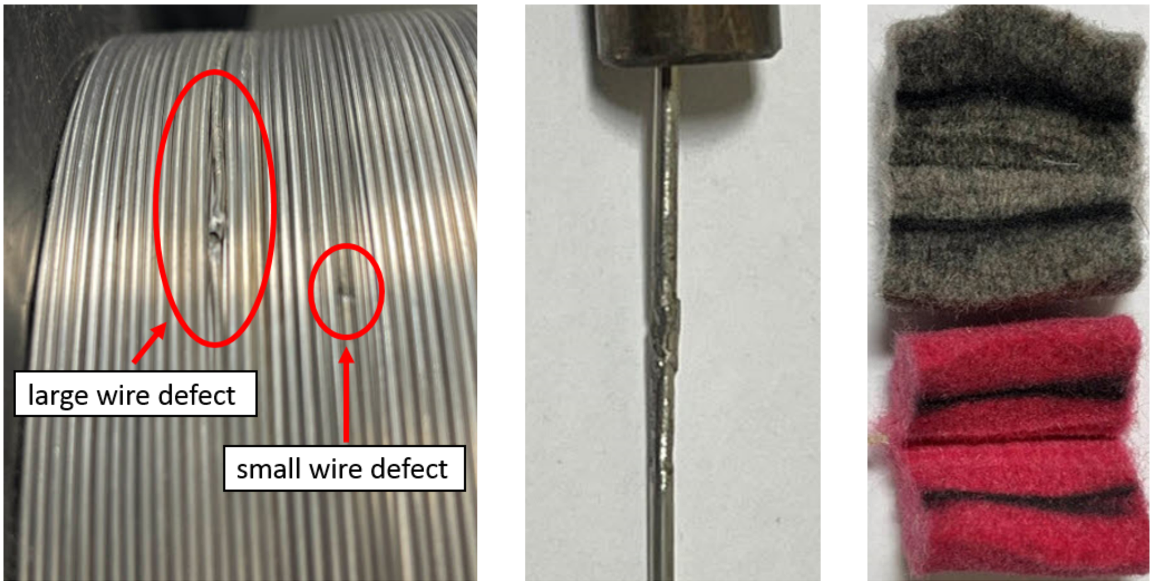

Figure 3.5: Heavy AZ61a wire oxidation along with small and large wire defects on the welding spool (left), wire defect shape that clogged the contact tip during extrusion (middle), and lubrication and cleaning pads that were installed between the wire feeder and the wire spool showing the considerable amount of oxidation that remains on the weld wire even after manual cleaning (right).

As can be seen in the left image of figure 3.5, the wire color is completely matte from oxidation. The wire was not properly stored before being sold to the consumer. It is of very high importance that welding wire be clean when it is being used. This is especially true for materials that suffer from high porosity issues, such as aluminum and magnesium. Without clean wire, the chance of trapping gas inside the weld pool after solidification increases drastically. Additionally, the vapor deposition on and round the weld bead also greatly increases. Before this wire could be used, it had to be extensively cleaned, which was a very time-consuming operation since it had to be done by hand. The wire was transferred to a second spool 1 meter at a time. Each meter of wire was cleaned carefully with 200 to 400 grit sandpaper and then rolled onto the second spool before the process repeats with the next meter of wire.

It is very important that as many contaminants as possible get removed, but without reducing the wire diameter of the wire. The charge to the wire comes from the contact tip inside the weld nozzle. These contact tips are precisely manufactured to ensure a close fit to the welding wire so that an uninterrupted transfer of electricity can take place. If too much of the welding wire material is removed, more problems will occur. The sandpaper cleaning process typically was performed for 100 m to 200 m of wire at a time. When the desired wire length was been cleaned with the sandpaper, a small stack of paper towels covered with acetone was used for further cleaning as the wire on the second spool was re-spooled onto the first, whipping away any remaining contaminants from the wire. This has to be done very carefully as to not tangle the wire on the welding spool because if there are any overlaps the wire feeder will not be able to push the soft magnesium all the way through the welding hose and through the torch. Even with this extensive cleaning process, not all contaminants were removed from the wire. Additional pads for cleaning and lubrication were attached to the wire before it entered the wire feeder, and as can be seen in the right image of figure 3.5, there was still a good amount of unwanted oxidation left on the wire.

The center image of figure 3.5 depicts another physical wire defect of the material. There were many sections of the weld wire where joining sections are not properly connected to one another. Some looked as bad as if they had been soldered together. This can cause problems in many areas. During the cleaning process, the wire was inspected for these defects so that these sections could be manually separated from one another as to not cause problems during the welding process. Sometimes during cleaning, these sections in the wire were so weak that they immediately rip apart when coming off the spool. Even though this resulted in losses in usable wire it is also brought with it the benefit of removing these sections before welding began, because these defects would have caused major issues during deposition. If a small wire defect was present during deposition, the wire would break in half while being pushed through the weld hose, which caused the deposition process to suddenly stop. A large defect will make its way through the welding hose, but then get stuck inside the contact tip. Both of these situations can render the currently printed part useless.

When the welding wire is stuck in the contact tip, the heat from the process will continue to melt the wire rapidly upwards toward the contact tip. The result is the filler material welding itself to the contact tip, and in some cases even melting the tip itself. This can be seen in figure 3.6.

Figure 3.6: Burn back and molten contact tips caused by wire defects clogging the weld nozzle and failure of weld droplet to detach itself from the weld wire.

As previously stated, the damage done is not just to the contact tip itself. While this occurs the deposition of the bead immediately stops as the CNC keeps moving the torch along the weld path. In multi-row deposition processes, the damage is typically so severe that it can't be fixed. Fortunately, depending on the severity the defect in the wire caused, in single bead multi-layer structures, it can be fixed if the proper steps are taken. Figure 3.7 depicts the result and fix for such a problem. The top image shows how the printing process has suddenly stopped during deposition, leaving a less than half finished bead with a sharp drop off slope at the end. This happened very frequently. It was imperative that a process be established to fix these layers, otherwise not a single final part would have been produced. With many trial and error attempts, it was determined that to fix this layer, the correction bead must be deposited starting from the opposite end of the original bead and must be deposited 3 mm past the last high point of the bead. Following this process, the two bead sections are fused together, and the result is a continuous layer height across the entire part.

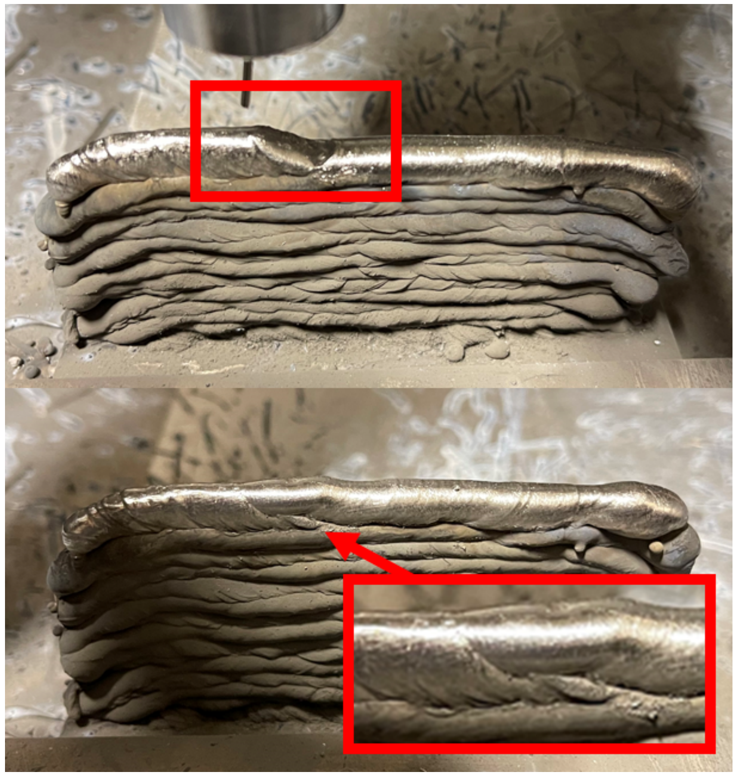

Figure 3.7: Bead profile at the location where deposition is abruptly halted due to a sudden stop of wire extrusion during deposition (top) and result of the developed correction method to fix such deposition errors (bottom).

In practice, establishing the correct welding parameters is achieved by starting with a pre-existing set of parameters based on wire material, wire thickness, and substrate thickness. The desired bead is then obtained by tuning the input parameters, voltage and amperage. For example, if the bead first appears to have too much of a caterpillar like shape, the user can slightly increase the voltage to flatten the bead. Voltage and amperage can be tuned independently of one another while keeping the other one fixed. This is done exclusively by trial and error in industry for every new operation. The problem in the case of this research is that presets for magnesium wire material do not exist on welders. Instead, it is suggested that Hard Aluminum should be used as the wire material of choice. However, the assumption that the aluminum presets would work well for AZ61a were incorrect. It was discovered that there was a very large difference between the welding parameters that were set on the machine, and the actual voltage and current that the welder output during deposition. Tables 3.1, 3.2 and 3.3 show samples of input vs output relationships for magnesium welding on the Welbee P400 for three different weld methods: DC, Pulse, and Synergic DC.

Table 3.1: DC Input (set) vs Output (actual) amperage and voltage.

A_{set}	A_{actual}	V_{set}	V_{actual}	P_{set}	P_{actual}
200	150	12	14	2,400	2,100
200	135	15	17.7	3,000	2,390
250	168	15	18.6	3,750	3,125

Table 3.2: Pulse Input (set) vs Output (actual) amperage and voltage.

A_{set}	A_{actual}	V_{set}	V_{actual}	P_{set}	P_{actual}
250	193	15	31	3,750	5,983
250	175	10	30.5	2,500	5,338

Table 3.3: Synergic DC Input (set) vs Output (actual) amperage and voltage.

A_{set}	A_{actual}	V_{set}	V_{actual}	P_{set}	P_{actual}
180	134	0	21.3	-	2,854
180	142	-100	13.5	-	1,917
250	175	-100	13.5	-	3,500
100	122	-100	16.7	-	2,037

In all cases, the output voltage greatly exceeded the desired input voltage. The opposite was true, in most cases, for the input vs. output current tests. An attempt was made to establish a relationship between input and output parameters in order to trick the machine into providing the output parameters that were desired. This was not possible, however, due to another large problem with the behavior of the welder.

As previously stated, when tuning welding parameters, either amperage or voltage gets altered while the other remains constant. This was not possible to achieve with the used inverter. Changes in voltage or current would result in the welder automatically changing the other parameter as well, making it impossible to tune. Figures 3.8 and 3.9 show how the welder behaves while adjusting a single parameter.

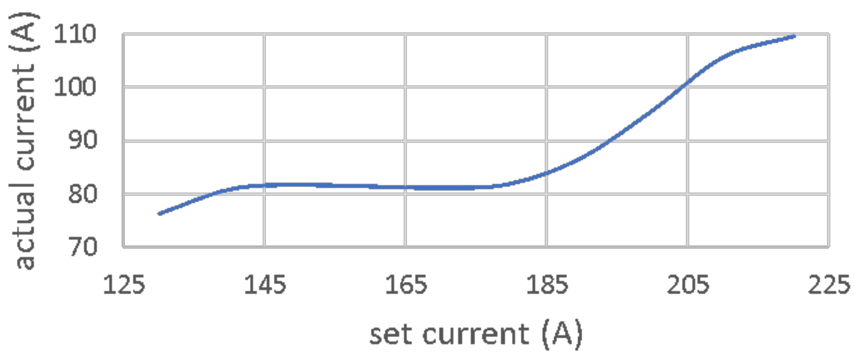

Figure 3.8: Relationship between welder input (set) current vs output (actual) current at constant voltage as the current is increased from 130 A to 220 A in increments of 10 A.

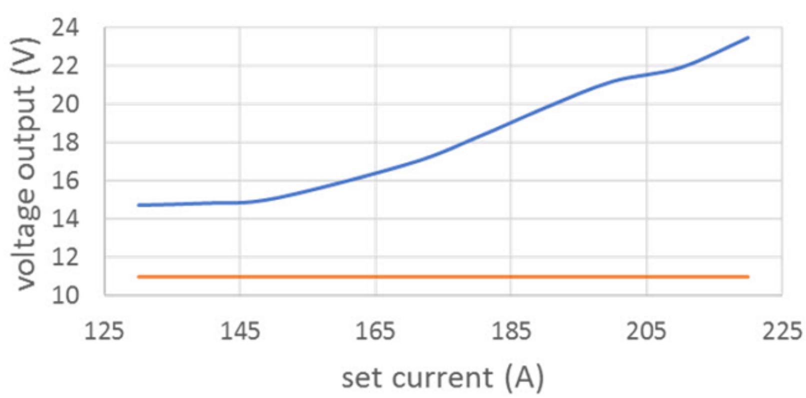

Figure 3.9: Welder voltage output behavior as the welder input current is increased in increments of 10 A from 130 A to 220 A.

At a constant voltage, the welding current was increased from 130 A to 220 A in 10 A increments. As can be seen in figure 3.8, not only was the output current much lower than desired, but it also increased in an erratic fashion. Figure 3.9 depicts the output voltage response when the current is increased along the same range as before. Even though the voltage was kept constant at 11 V, the output voltage was not only drastically larger but also increased continuously with increasing set current. DC Pulse welding showed by far the largest difference between input and output, especially with respect to voltage. This rendered DC pulse unusable for this research as the heat was so high that it vaporized much of the material and resulted in virtually no deposition of material. DC deposition was therefore the only method that could be investigated with this setup. Trial-and-error was the only available method to attempt to find usable parameters, and after a very large number of attempts, some decent parameters were obtained, which will be covered in the following section.

Interestingly, even though the machine output of voltage and current do not match those that are being input, the WFS, on the other hand, is exactly that of the coupled set input current. Welding current and WFS are locked together in MIG welders. Given that the welder produces a far lower current in actuality than was set, it would follow that it would also drop to the WFS that matches the lower output current. This is not the case. Instead, it outputs the exact same WFS as was originally requested. This adds further problems to the deposition process, as the heat input drops through the lower current, but the feed of the material stays at a higher level.

There are two material properties of magnesium that are also problematic for GMAW: the low evaporation temperature and the low viscosity of melted magnesium. Figure 3.10 shows a comparison between the viscosity of magnesium and aluminum above melting temperatures. Unfortunately, not much data exists, but even with the limited data available it can be seen that the viscosity of magnesium is much lower than that of aluminum, especially as temperatures increase. This low viscosity causes magnesium to tend to flow more rapidly across and out of the weld pool, leading to side flow and uneven beads. This problem gets compounded as multiple beads are overlapped with one another to create a wide base layer for a printed structure. This can be seen in figure 3.11, where an example of how this side flow occurs when looking at a single bead and a set of 2 beads overlapped. Adding to this fluidity problem is the low thermal conduction heat transfer coefficient of magnesium alloys. The AZ31a substrate and AZ61a wire have a thermal conduction coefficient of 70 $Wm^{-1}K^{-1}$. By comparison, the thermal conduction coefficients of the 6061 aluminum substrate and 5356 aluminum wire that were used for initial testing are 167 $Wm^{-1}K^{-1}$ and 116 $Wm^{-1}K^{-1}$, respectively. Thus, not only is the viscosity much lower than that of aluminum, but the heat removal rate is also must lower, increasing the transition time of the magnesium back to a solid state.

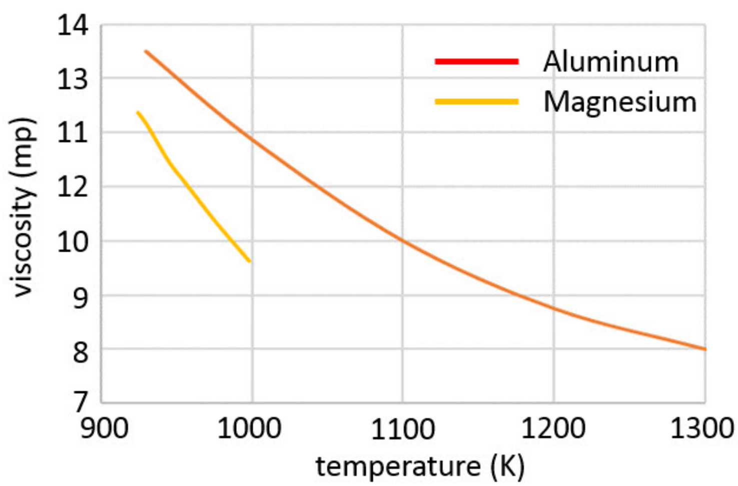

Figure 3.10: Viscosity comparison between magnesium and aluminum at melting point and beyond [160,161].

Figure 3.11: Example of how the low viscosity of melted magnesium causes severe side flow out of the weld pool during the deposition of overlapping beads.

The fluidity of the molten magnesium also increases the risk that humping will occur. Typically, this phenomenon is only an issue when welding at very high torch speeds ($>$ 1000 mm/min), but due to the low viscosity, it can happen at much slower travel speeds with magnesium. The result is a bead that features multiple different widths and heights, and is therefore not acceptable for AM purposes.

It has been shown that the deposition temperatures can't be too high for this process. But lowering the process temperature leads to additional problems, including delamination from the substrate and lack of fusion between layers. After much research, an easy way to deposit magnesium structures while maintaining good part shape was determined, but inspection of these parts after machining proved that the lack of fusion renders these parts unusable. This can be seen when building low heat input, cross-bead stacked blocks. Figure 3.12 shows how each additional layer is barely, if at all, fused to the layer below, but is instead just laid on top of it. Additionally, given that thicker substrates are needed when building large structures, the low heat will also not allow for any substrate penetration to ensure that the part remains on the base. When it comes to finding the proper set of parameters for this type of deposition, the window for usable parameters is very small.

Figure 3.12: Lack of fusion between deposited magnesium layers caused by insufficient heat input.

Adding to the concern of cracking and delamination is the warping of the substrate that occurs during the deposition process. Every deposited layer wants to shrink as it goes through the solidification process but is hindered to do so by the substrate and by the layers beneath it. What ends up happening is that all the material on the substrate is trying to pull the substrate inward, which in turn can cause distortions in the part. The warping in the substrate can of course be reduced by simply using thicker material, but due to the expensive nature of the material, the maximum thickness that was used in this work was 12.7 mm. To give some perspective on these costs, a 12 in. x 4 in. x 0.5 in. plate of 6061 aluminum costs $30, while a plate of the same dimensions of AZ31B costs $130. The difference in cost of the magnesium wire compared to aluminum wire is even more extreme, with a 10-pound 3/64 inch wire-diameter spool of 5356 aluminum costing around $100, and the same amount and type of AZ61a wire costing almost $1,200.

During multi-layer block deposition, the amount of stress experienced in the substrate was so large that it not only deformed itself, but also managed to severely deform the clamps used in the enclosure, as shown in the left image of figure 3.13. Once removed from the machine, the substrate continues to deform, in some cases by over 2 cm from end to end. It is therefore recommended that thicker substrate be used for this process.

Figure 3.13: Severe substrate distortion inside the holding clamps of the CNC during the deposition of a large magnesium block (left), and final distortion of the substrate after having been removed from machine (right).

Vapor deposition, even with cleaned wire and substrate, is much greater than with other materials. The left image in figure 3.14 shows the state of the bead and substrate after the deposition of a single bead. Given the state of the material, it must be cleaned before any additional beads can be deposited on top of or next to the bead. Additionally, additive manufacturing of magnesium brings with it the risk of potential fire. This risk can be mitigated by limiting the heat input and by ensuring that the correct interpass cooling time is implemented. One magnesium fire occurred in this research during initial testing while different weld parameters were being tried by hand. The combination of too high of an input temperature from pulse welding, along with a very low interpass cooling time, resulted in the bead and substrate igniting and burning. Fortunately this occurred on a welding table and no parts of the CNC were damaged. Figure 3.14, middle and right images, depicts where the fire occurred and how it burned all the way through the substrate.

Figure 3.14: Magnesium oxide vapor layer around the AZ61a weld bead after deposition (left), top view crater left behind in substrate after AZ31b substrate ignited due to insufficient interpass cooling time and excessive heat input (middle), and bottom of substrate view at the crater location where molten magnesium flowed through the base (right).

Spatter, as stated in [101], was one of the primary reasons this method was deemed not possible for magnesium deposition. This is a very valid point as it is very much an issue. A few figures displaying the severe spatter encountered in the beginning phases of thie research and be found in Appendix E. It took a very long time to find weld parameters coupled with travel speeds that were able to reduce and almost eliminate this problem. The occasional occurrence of spatter, especially when dealing with wire defects, remains present, but only at the higher heat input parameters that will be discussed.

3.3.2 Deposition parameters

For single bead deposition, several criteria must be met in order for a bead deposition process to be considered successful. The bead must retain its shape for its entire length and not suffer from excessive side flow or humping . For bottom layers, the bead must show decent adherence to the substrate by providing sufficient penetration. There should be little to no spatter involved in the process. There should be no visible defects on the outside of the weld bead.

Several parameters were determined that resulted in deposited beads that satisfy all the set criteria. These parameters fall into two groups: low input-energy-rate (IER) and high input-energy-rate. IER is defined as the power (current x voltage) the welder puts out during the deposition process. IER is also referred to as heat-input rate in many publications. It is important to note that in most cases, the torch travel speed at different power levels is different to account for changes in the wire feed speed at different welder currents. Therefore, the input energy per unit length for a bead or layer is dependent on both welder output power and torch travel speed.

The low-IER set currents ranged from 130 A to 165 A, and were combined with set voltages between 13 V and 15 V. As previously mentioned, in MIG welding the current is coupled to the WFS, and even though the current the welder outputs is considerably lower than the magnitude that was set by the user, the WFS that the welder puts out is the same as the set WFS.

In the range of a set current from 130 A to 165 A, the output powers that were measured were between 1,300 W and 1,800 W. On the lower end, a set current/voltage combination of 130A/13V resulted in an output of 90A/14.2V (1279 W) that was of decent quality, but the deposition suffered from occasional physical pushback of the wire as the heat was not melting the wire fast enough. The best results for the lower end of the low-IER parameters came with a set current/voltage combination that lead to an output of 78.5A/16.5V. Interestingly, since the welder decreased the supplied current even though only the voltage was increased, this resulted in the same power as the previous test of 1296 W. For both these tests, the WFS stayed the same at 8.36 m/min. On the upper end of the low-IER parameters, the set input current/voltage combinations of 165A/13V and 165A/15V resulted the measured outputs of 100A/16V and 97A/18.1V, respectively, providing an energy input rate of 1606 W and 1756 W at the same WFS of 10.5 m/min. The TTS setting for these tests was between 300 and 500 mm/min, leading to upper and lower energy input per mm results of 153 J/mm to 351 J/mm. These low-IER parameters, though much slower in deposition than the high-IER parameters, exhibited no spatter problems at all. Shielding gas in the form of 100% ultra-pure argon was supplied at a flow rate of 16.5 L/min in all experiments. Figure 3.15 shows the quality of weld beads deposited at a low-IER (left) and demonstrates the stability of the deposition process (right).

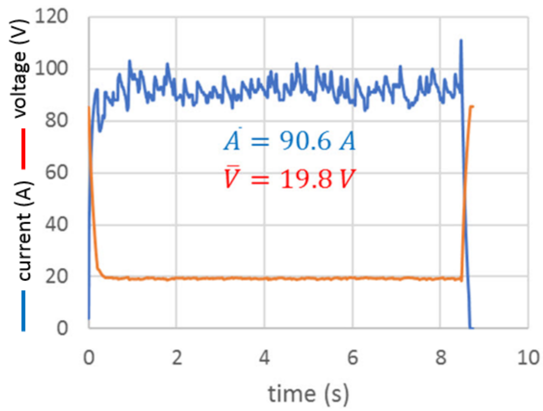

Figure 3.15: Low-IER (1300 W to 1800 W) deposited AZ61a beads with uniform shape and height (left) and low-IER measured inverter outputs demonstrating arc stability for the process (right).

For the high-IER input parameters, the range of a set current from 200 A to 250 A, resulted in measured power outputs between 2,400 W and 3041 W. The heat input for these parameters is at the limit for where vaporization and weld bead deformation take place. Excellent results were obtained with a set input combination of 220A/15V (2550W), which provided an output of 136.7A/18.7V, with a WRF of 14.8 m/min on average. The upper limit for these high-IER parameters was found to be a set combination of 250A/15V, yielding a power output of 3041 W with a current of 159A and a voltage of 19.1 V. The WFS for those settings is an impressive 16.6 m/min. The TTS for this set had to be increased to the range of 500 mm/min to 850 mm/min, resulting in energy input per mm magnitudes between 191 J/mm at high TTS and 364 J/mm at low TTS. Figure 3.16 shows the quality of the weld beads obtained at high-IER on the left, and the measured output demonstrating its stability. These beads took on a more traditional shape, with complete substrate adhesion along the edges and a flatter profile, making them ideal for overlapping and stacking of additional beads. Measured output plots for other successful high and low-IER deposition parameters as well as plots showing the severe instabilities that occur when moving even just a little bit outside these ranges is shown in Appendix A and Appendix B, respectively.

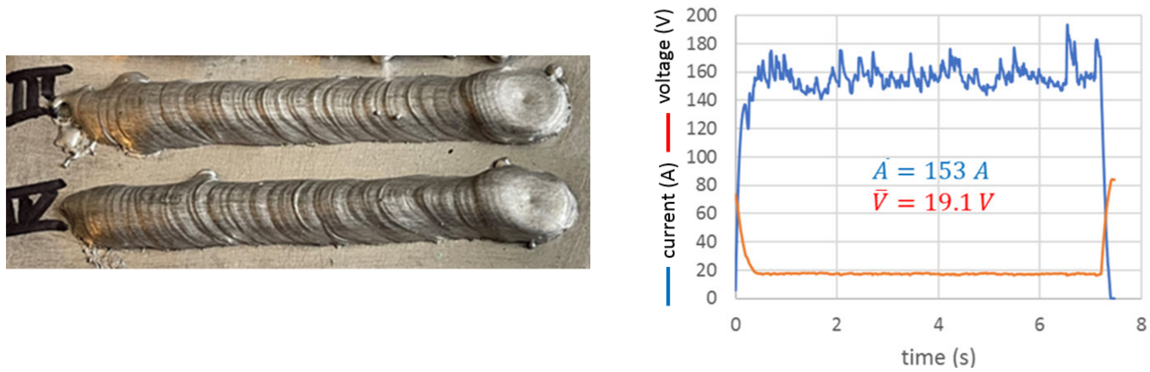

Figure 3.16: High-IER (2400 W to 3000 W) deposited AZ61a beads with uniform shape, height and base penetration (left) and high-IER measured inverter outputs demonstrating arc stability for the process (right).

These established parameters were used to print magnesium samples in the forms of single-stacked multi-layer walls, closed shape parts in the form of hollow cylinders, and multi-row/multi-layer (MRML) blocks. The following subsections describe these processes.

3.3.3 Single-wall deposition

Weld beads have a different shape at their end as they do at their start. While the start of the weld bead has a more rounded shape and is raised high off of the substrate, the tail end of the bead is much flatter and, in many cases, even has a crater like shape. When building multiple layers, this must be considered. When building single bead walls or any other multilayer structure, there must be a rotation between starting and ending position. If this is not done, the tail end of the layered part will quickly slope away from the rest of the part. This can be clearly seen in figure 3.17.

Figure 3.17: Gradual deterioration of multilayer block profile at the end point of bead deposition.

Simply alternating between the start and end of the bead does not solve every problem. As the number of layers starts to increase, differences in height along the beads will become more and more prevalent. This is especially detrimental for maintaining a constant nozzle to workpiece offset. Experiments in this study found the optimal nozzle to workpiece offset to be 10 mm to 12 mm. The wire coming out of the nozzle is not perfectly straight and will curl away from the centerline. This means that the position of the wire directly above the previously deposited beads cannot be guaranteed if the offset distance continues to change. Additionally, the timing between the weld start and the beginning of the torch movement must be carefully synced. Ideally, a sensor should be incorporated that triggers the motion of the CNC as soon as the arc is established. This, however, cannot be accomplished with G-code on the current machine. In order to compensate for this shortcoming, multiple height measurements were taken at three positions after the deposition of every bead. Based on these heights, the vertical Z position in the G-code for the next layer was established so the the overall offset changes are minimized. In order to keep the top layer of these structures as flat as possible, different dwell times at start and end of the bead were determined, which depend entirely on the structure of the bead last deposited. Low heat deposition proved to be the most consistent as its impact on the base layers was very small.

Figure 3.18: Stacked layers of low-IER printed wall during the deposition process (left) and bead profile from the top view (right).

Figures 3.18 shows the layer progression and bead profile of a low IER printed magnesium wall. Layer orientation and thickness was well controlled up to a height of 70 mm. Due to one of the wire defects discussed in an earlier section, the top layer for this wall suffered from intermittence, which was too severe to fix on the CNC. The final part is depicted in figure 3.19. The impact the wire defect had on the top layer can be seen from the front view.

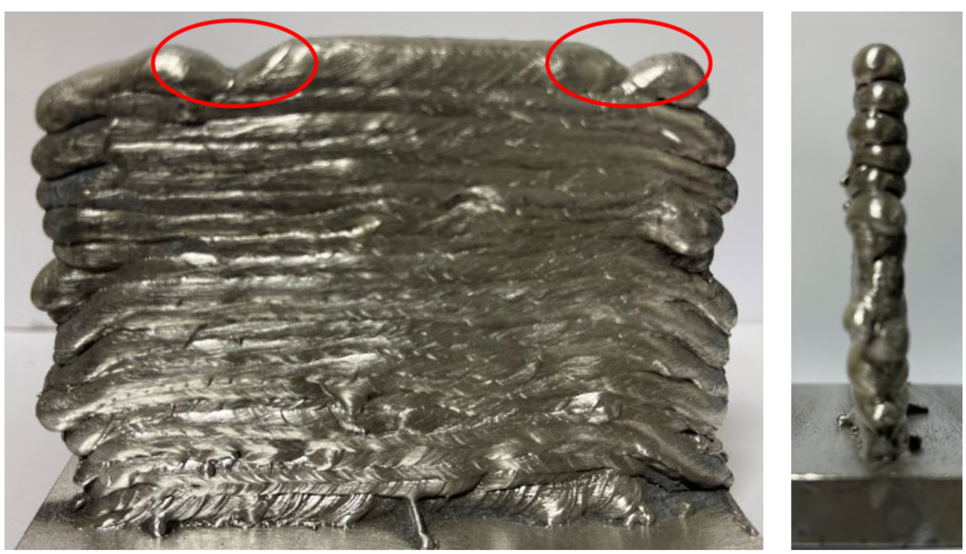

Figure 3.19: Finished low-IER printed multilayer wall with two bead defects on the top layer caused by wire defects temporarily clogging the weld nozzle during deposition (left) and side view of low-IER printed wall (right).

The following plots give a detailed look at the process performance as well as the forming of the part. The left plot in figure 3.20 shows the average welder outputs during the thin wall deposition process. The average current output during deposition was 99.2 A, with a standard deviation of 4.3 A, while the average output voltage was 16.9 V with a standard deviation of 0.2 V. This makes the IER 1683 W. With a TTS of 450 mm/min, the energy input per unit length for all these layers was 224 J/mm. Even though this method was mostly stable, occasional current surges would occur. Fortunately, only minor alterations to the weld shape profile were caused during these interruptions. An example of a current spike during the deposition of the thin wall is shown in the right plot of figure 3.20.

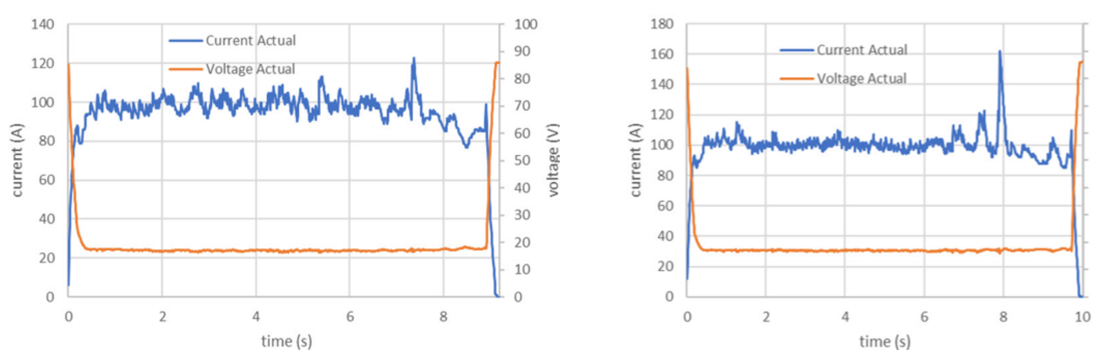

Figure 3.20: Measured low-IER inverter output during single wall deposition (left) and example of current spike during deposition resulting in minor defects to the surface profile of deposited beads (right).

Loafing is a common issue that occurs in many additive manufacturing processes, especially for those with large heat inputs. The added heat tends to flatten the previously deposited layer, which can cause inconsistent buildup of the part. Figure 3.21 shows how the part height per layer of all walls built with these parameters compare to one another, with the red bars giving the standard deviation for the layer height. The part height increases consistently per layer, with an average of 2.6 mm being added in height per pass. After each layer was deposited, height measurements were taken at three locations on the new bead. As can be seen in the figure, the part height progression remained consistent for the duration of the process.

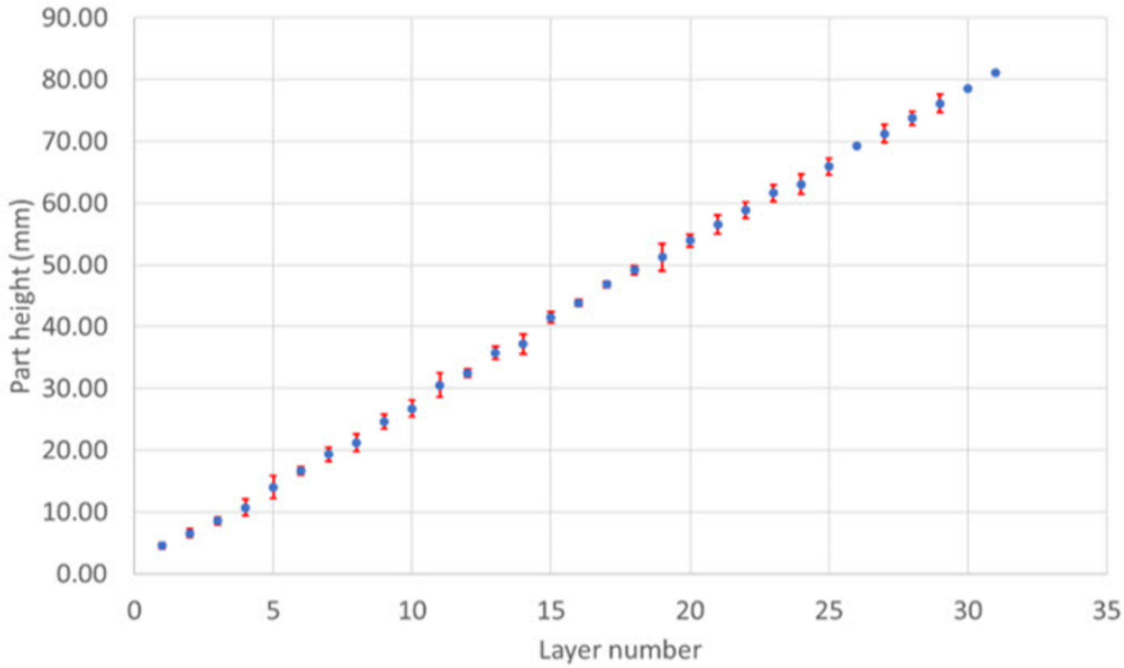

Figure 3.21: Comparison of part height by layer in identically printed walls (left) and average part height per layer with 2 standard deviation bars (right).

Figure 3.22 shows the layer progression and bead profile of a wall that was printed using the same IER as the example above, but with a higher energy per mm due to a lower TTS of 300 mm/min. This makes the energy per unit length 337 J/mm, a 50% increase from the previous case. Flat layer deposition was possible, but more challenging than with the previous low heat method. This was due to the increase of loafing, but was not severe enough to make controlling the process unmanageable. The primary physical benefit of this method is that thicker walled parts can be created at a faster pace. With this method, final wall thicknesses of up to 5 mm after machining can be achieved, while with the slower torch travel method the maximum attainable thickness was 3 mm. How these thicknesses were established will be discussed in the next chapter.

Figure 3.22: Bead profile of walls being deposited with high-IER (left) and width measurement of the beads as the layers were added (right).

Figure 3.23 shows how the part height increases per layer and two standard deviation bars. Each layer was measured in the same manner as previously explained. Even with the increased loafing, the increase in layer height remained consistent, adding 3.5 mm per bead. The right plot in figure 3.23 shows the build rate per layer of the two travel speeds. Figure 3.24 shows three of the sample walls on a substrate about to get machined down to walls for the extraction of tensile test specimens.

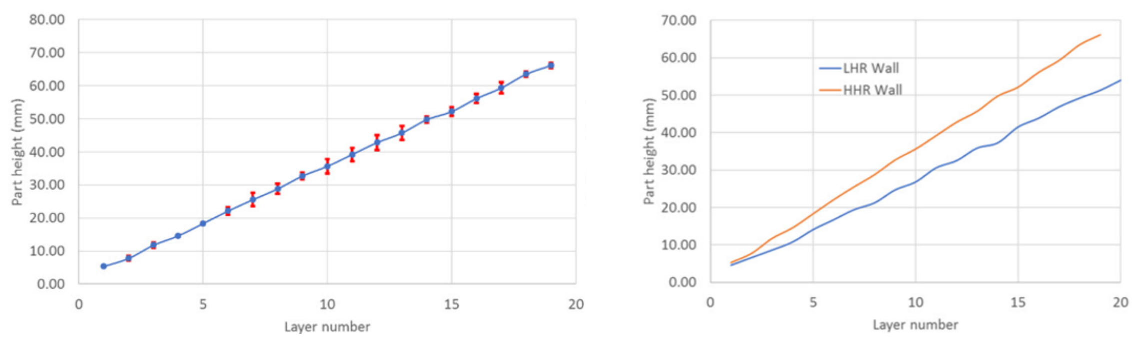

Figure 3.23: Build height per layer using low IER and low TTS with 2 standard deviations bars (left) and comparison of layer heights between high and low TTS at same IER wall depositions (right).

Figure 3.24: AZ31b substrate with AZ61a printed multilayer walls prepared for thin-walled machining.

3.3.4 Hollow-cylinder deposition

Hollow cylinders were printed with the two different parameter windows to test the manufacturing of closed form shapes. The first cylinder that was printed was deposited with the low-IER parameters. The base layers of this cylinder are shown in figure 3.25. The base retains a great shape on the substrate, and a consistent layer height remained as more layers were added, as seen in figure 3.26.

Figure 3.25: First layers of low heat input hollow cylinder print.

Figure 3.26: Layer fusion and shape retention during low-IER cylinder print (left) and closure problem evolution as layers are added to the printed part (right).

The deposition was stopped after 10 layers due to the closure problem encountered, as can be seen in figure 3.26 on the right. As previously stated and discussed in the literature review, connecting shapes using welding operations can be problematic. In the case of this cylinder, the start and end positions were the same for every layer, resulting in the growth of a tail-like connection between the two ends of the beads. Altering the welder parameters to resolve this issue was not an option due to the limited range of usable combinations of voltage and current. Instead, another method was developed to ensure that the shapes are properly closed. First, the start/end positions of the cylinder were rotated by 180 or 90 degrees for each additional layer. Second, when the torch got its final position, it dwelled for 1 second before the arc was extinguished. The same method as demonstrated in making corrections to intermittent layers in single wall structures was used to close the shape. This resulted in the ability to continuously build layer upon layer without a large gap going down the part. Figure 3.27 shows the evolution of how a hollow cylinder that was built using the high-IER parameters.

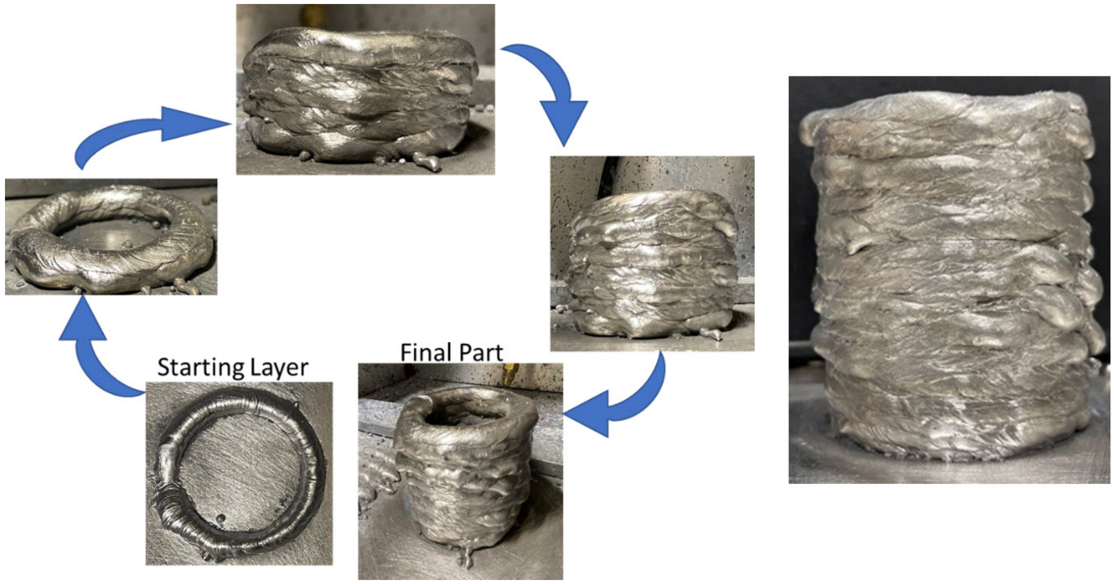

Figure 3.27: Print of hollow cylinder with high-IER from start to finish demonstrating consistent part height as layers are being added (left) and final printed and cleaned cylinder ready for finish-machining (right).

The deposition of the layers using this method was stable for every layer, with a sample of welder output shown in the left plot of figure 3.28. The parameters set on the welder were a current of 250 A with a welding current of 11 V. The average output current and voltage were 161 A and 16.2 V, respectively. The measured wire feed speed for this deposition was 16.6 m/min, making it one of the fastest deposition methods attempted in this research. The TTS was kept constant at 600 mm/min. Given this data, an energy-input rate of 2608 W and an energy per unit length of 261 J/mm were applied.

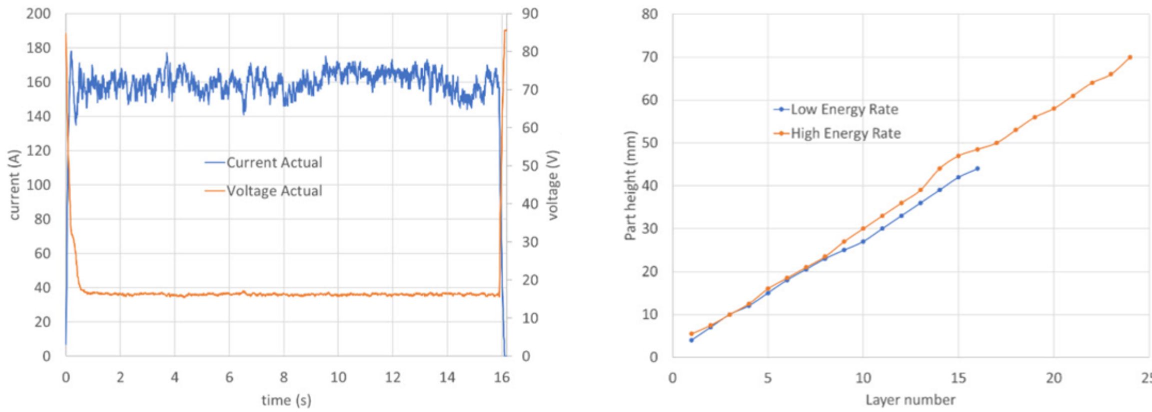

Figure 3.28: Stable inverter output at high-IER during cylinder deposition print (left) and comparison of part height of printed cylinders by deposition layer of high and low-IER prints (right).

The same process was repeated for the low input heat method, as can be seen in figure 3.29. After depositing 16 layers of the cylinder depicted in that figure, the part was again impacted by a wire defect, and deposition had to be stopped. The cylinder, however, still consisted of enough layers to be machined and investigated. Figure 3.29 depicts the bottom layer print (left) and the final print, ready for machining (right). As can be seen, a decent shape was retained for the layer by layer deposition. The set welder current and voltage in this case were 130 A and 14 V. The actual current and voltage were 74 A and 15.4 V, making the energy input rate 1140 W. With a TTS of 500 mm/min, the energy input per mm was 137 J/mm. This was the lowest energy input per unit length attempted in this project. The resulting cylinder retained decent shape but was very thin, and due to the extremely low heat input, pushback was discovered frequently while examining the output data from the welder, indicating the wire is not melting fast enough and gets rammed into the surface of the build, causing a current surge. An example of this is shown in figure 3.30. A minor increase in power resolved this issue. The final part dimensions after machining will be discussed in chapter 4.

Figure 3.29: First two layers of printed cylinder with low-IER input parameters (left) and final printed hollow cylinder printed with low-IER with the top layer indicating pushback occuring during the deposition (right).

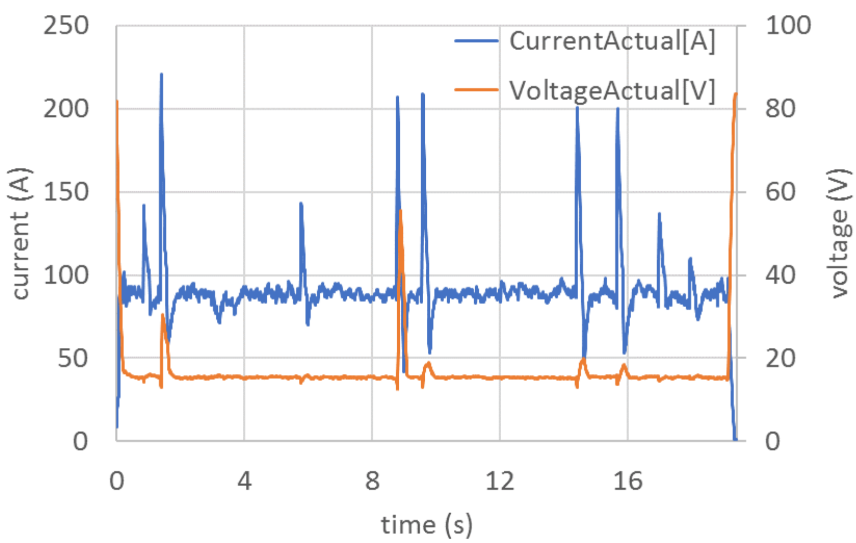

Figure 3.30: Measured inverter data during very low-IER deposition indicating shorting caused by pushback due to insufficient heat in relation to WFS.

3.3.5 Multi-row/multi-layer deposition

For magnesium, multiple overlap percentages were tested to determine the maximum amount of overlap before side flow of the beads became too much to continue. It was determined that when building a layer by depositing beads continuously next to one another, 40% overlap was the cutoff. It is important to note that side flow is present at even the smallest percentage of overlap when depositing beads in this manner. Using a low-IER for this process does not work as there is simply not enough fusion of adjacent beads, and the caterpillar like shape of these beads result in long internal air channels. The first multilayer block of AZ61a magnesium that was manufactured can be seen in the images of figure 3.31. This block consists of 65 individual 175 mm long beads that were deposited with a machine set amperage of 220 A and a voltage of 15V. The actual output was measured at 150 A and 18 V. The beads were spaced 5.5 mm apart, resulting in an overlap of around 40%. As can be seen in the figure 3.30, this overlap caused significant flow on the sides of the block, but a rough net block shape was still retained. Between each bead deposition the workpiece was brushed and cleaned. The block itself was 175 mm in length, 80 mm in width, and 25 mm in height. The length and width were slightly narrowed for each of the subsequent layers, of which there were 7 in total. At the start of the fifth layer the first bead failed halfway through the deposition process. This bead was fixed by running a second bead from the other side into the end of the failed bead. Figure 3.30 shows multiple angles of the final block that was created. The bottom right image in figure 3.30 shows the warp that occurred in the substrate, with an end-to-end deflection of 22 mm.

Figure 3.31: Images of the first AZ61a block printed on the AZ31B substrate showing dimensions as well as substrate distortion and side flow caused by bead overlapping during deposition.

The deposited material was then machined into a block, as can be seen in figure 3.32. Upon inspection it was found that minor voids were occurring in select areas across the sides of the block. Numerous additional settings were tested following this experiment to reduce these voids, including welding parameter changes, layer orientation, overlap percentage changes, and clamping methods. It was determined that the most likely cause of these voids were pockets in the deposited layer caused by melted material that was flowing off the bead during overlapping depositions. An example of such pockets is shown in the right image of figure 3.32. As can be seen, even though the previously deposited layers appear to be nicely fused together, they are still most likely suffering from internal voids due to such pockets not being entirely removed when the subsequent bead is being deposited on top of them. Resolving this issue was the biggest challenge moving forward.

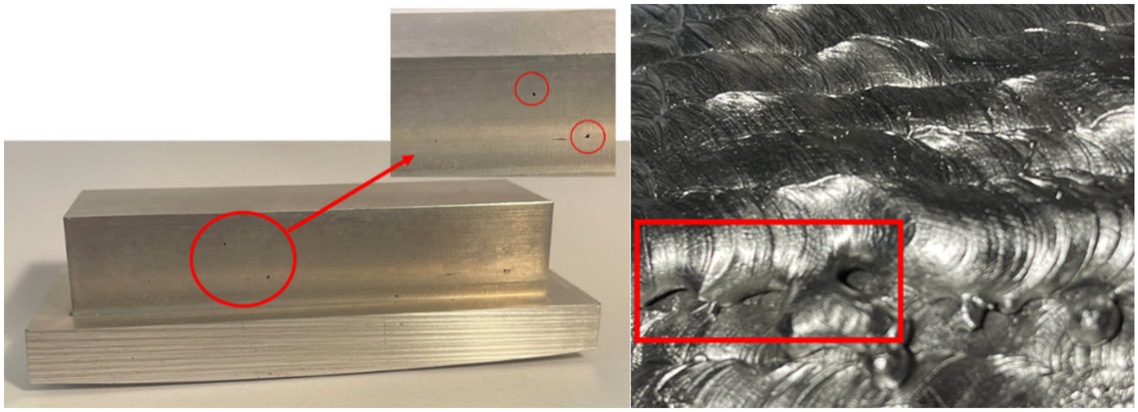

Figure 3.32: Post deposition machined AZ61a block with small defects (left) and pocket formation due to side-flow and wire defects (right).

Instead of building each layer by using different percentages of overlap for immediately adjacent beads, it was decided to space deposited beads apart from one another, creating a channel of empty space between them, and then depositing an additional bead into the empty channel. The first test using this method was done by utilizing a zero percent overlap for adjacent beads. This can be seen in the left picture of figure 3.33. The next layer would be deposited into the channel between the beads. The problems with excessive flow caused by overlapping the beads was immediately reduced, resulting in layers that kept their shape much better than before. The downside of this approach is that naturally the final part will have a pyramid like shape, as every subsequent layer will be deposited with a shift of half the width of the bead. The first small test result of this staggering approach can be seen in the right-side picture of figure 3.33.

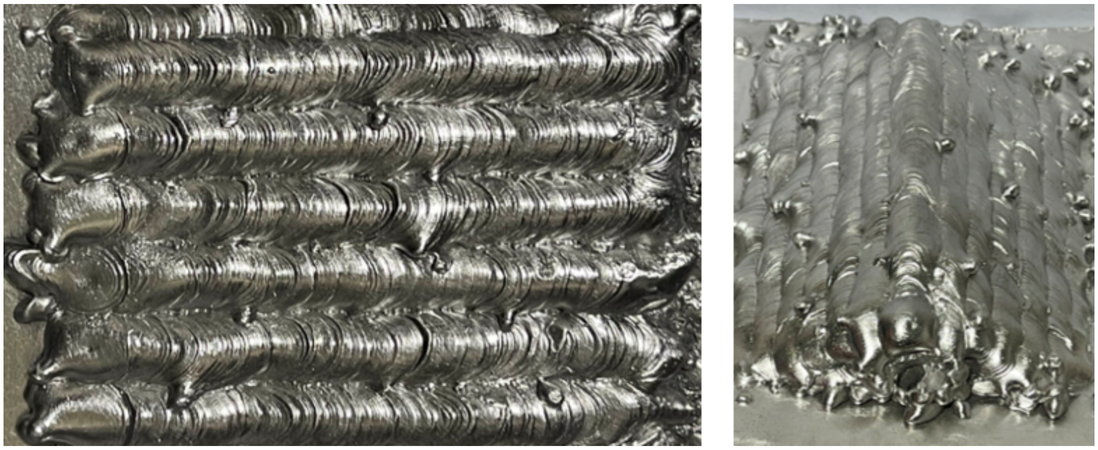

Figure 3.33: Zero percent bottom layer overlap staggered pyramid base resulting in a 50 percent second layer overlap (left) and final pyramidal shape of this print strategy (right).

Following the success of this method, multiple layer bead spacing approaches were tested, increasing the space between beads up to 80% of the bead width. It was determined that a bead gap of 30% of the bead width resulted in the best final shape of the deposited block. Figures 3.34 to 3.36 display how different patterns were investigated for both low and high heat input beads, as well as short and long deposited beads.

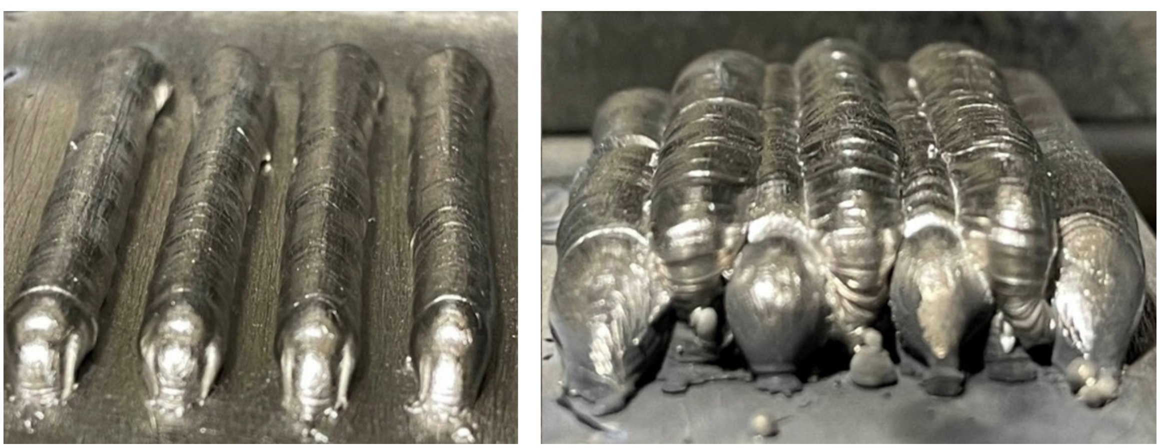

Figure 3.34: Base layer (left) and subsequent deposited layers with a stagger-channel approach using low-IER input parameters, indicating possible lack of vision between layers due to insufficient heat input(right).

Figure 3.35: Long bead base layer deposition with channels resulting in a 50% overlap.

Figure 3.36: Short bead base layer channel deposition which will result in a 40% overlap.

Due to the pyramid like structure of the final parts, the first large block that was manufactured was done so using short beads that were deposited across the width of the substrate instead of long beads deposited across the length of the substrate. This was done to ensure that there would be more usable material for extracting tensile test specimens. This also meant that the total heat input per bead was less than half than what it would be if long beads were deposited. Given the lower final temperature of the beads, side flow caused by overheating was also reduced. This, however, also meant that the deposition print direction would be normal to the direction later to be applied during the tensile test. Therefore, any cracks/voids due to pockets would most likely cause the material to fracture at a lower load.

The first large block using the new stagger method was created and can be seen in figure 3.37. The layers retained a decent shape and excessive flow was almost entirely controlled. This block consists of 137 individual 80 mm long beads. After each bead was deposited, the substrate and deposit were thoroughly brushed and wiped clean manually. The block was then cut via WEDM to create tensile test specimens, which will be discussed in the next chapter.

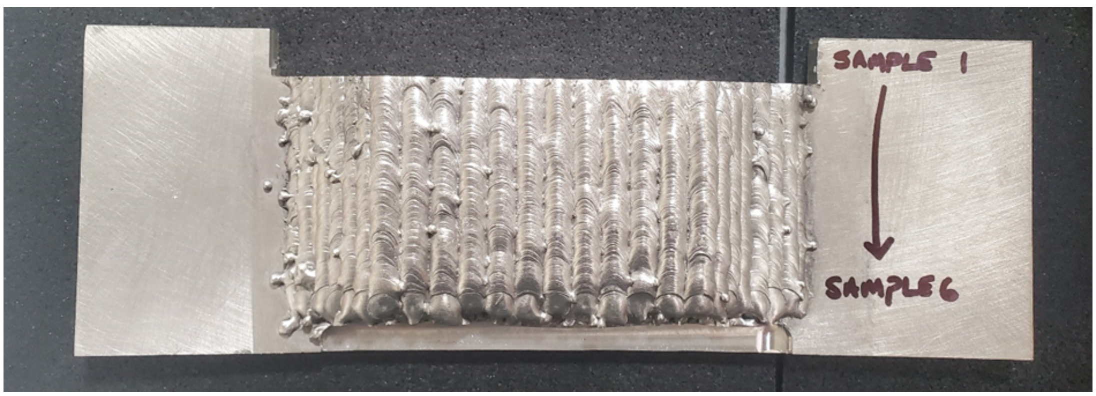

Figure 3.37: MRML block printed using staggered short beads to be used for tensile test specimen extraction and microstructure analysis.

The same staggered pattern was then used to print more magnesium blocks, but now in the long direction. An example of this is shown in figure 3.38. Due to the required stagger shape, the final number of tensile test specimens that could be extracted out of these blocks was much lower than that of the previous block. In addition, arc wandering was more pronounced and had a greater impact on the shape of the beads. The increasing temperatures during the deposition most likely had an impact on this as well. These blocks will provide insight to how the print direction impacts yield strength as well as fracture strength. One of the most detrimental problems during this research was how the defective weld wire impacted the build of these blocks, with many builds having to be abandoned because sudden intermittent issues caused by the wire resulted in layers that could not be fixed.

Figure 3.38: MRML block printed using staggered long beads to be used for tensile test specimen extraction and microstructure analysis.

These large blocks were printed with a set current/amperage of 200A/15.5V, resulting in an average output of 131A/18.5V, as can be seen in figure 3.39 which depicts the data for the deposition of a 175 mm long bead located on the third layer of the block shown in figure 3.38. The WFS during deposition and the TTS were 13.6 m/min and 750 mm/min, respectively, leading to a bead energy input of 248 J/mm.

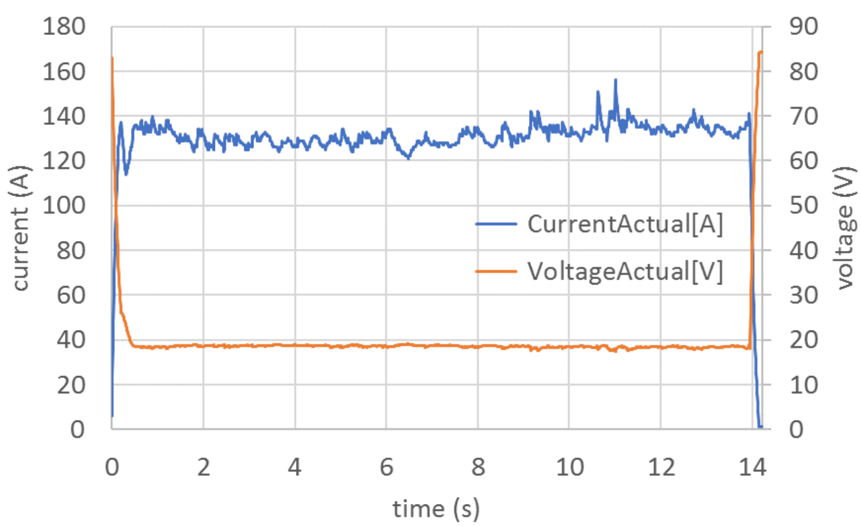

Figure 3.39: Measured inverter output parameters for the printing of a large block with long beads, indicating a stable arc throughout the process.

CHAPTER 4: EXPERIMENTAL METHODOLOGY

This chapter explains how the final deposition successes presented in Chapter 3 were attained. The setup of all the equipment is explained along with the modifications made to it. Furthermore, strategies for how to obtain desired magnesium deposition results are discussed, along with usable build strategies for multiple types of structures. These strategies can be applied with any inverter and utilizing any automated CNC or robotic gantry system

4.1 Equipment and material

The experiments conducted in this work can be repeated on any 3 to 5-axis CNC that has a build chamber of sufficient size to accommodate the welding torch that is being utilized. A custom collet attachment will need to be designed so that the welding torch attachment can be fastened inside the spindle. An enclosure with a minimum wall height of 30 cm should be fastened to the CNC build table to ensure that the spread of spatter inside the machine is limited. For added safety, a fume extractor should be placed within 50 cm of the deposition area to remove the toxic weld fumes. Additionally, the build table should be isolated from the bottom of the enclosure to reduce the chance of heat transfer and electrical charge into the machine occurring, both of which could damage the CNC.

The inverter welding power source used in these experiments was the Daihen OTC Welbee P400. The torch was a Blue Torch III 50% MIG duty cycle with a 10 feet long weld hose. K980C37 contact tips designed for a wire diameter of 1.2 mm and a 10 feet long PLA liner were used. The Welbee 4-drive roll wire feeder was installed on top of the inverter. Due to the soft nature of magnesium, it is notoriously difficult to push through the welding hose, so the included wire feeder gears and rollers were removed and the aluminum kit for soft wires was installed, as can be seen in figure 4.1.

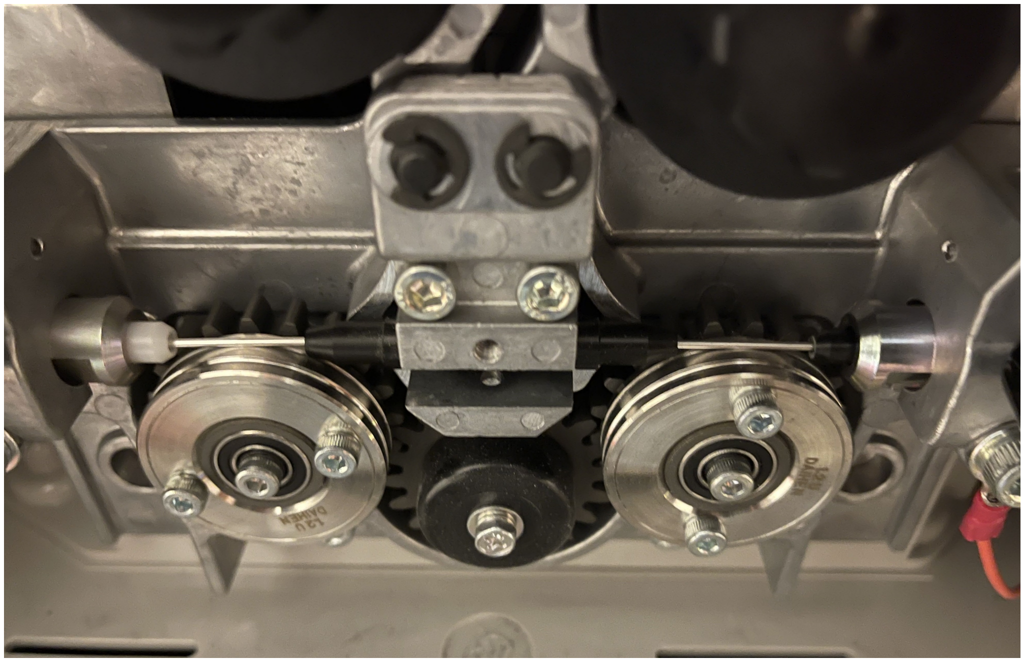

Figure 4.1: Aluminum kit for soft wire material installed in the wire feeder to ensure smooth feedrates during deposition.

All tests were performed using 10 pound spools of 1.2 mm (3/64 in) diameter AZ61a welding wire. It is imperative that the wire being used is inspected for oxidation and material defects. The wire should be cleaned with sand paper and subsequently wiped down with acetone before being used. Care must be taken not to remove too much of the material so that good contact between the weld wire and the contact tip can be maintained. For additional wire cleaning, Lube-matic cleaning and lubrication pads were installed between the wire spool and the wire feeder.

The substrates used were AZ31b-H24 plates with dimensions of 300 mm x 100 mm x 12 mm and 300 mm x 300 mm x 12 mm. The substrate corners were filed down to ensure that the plate will make complete contact with the grounded weld enclosure. The top and bottom surface were first cleaned with an electrical sander until no visible oxidation remained. The part was then vigorously cleaned with a stainless-steel brush and then wiped down with acetone before being clamped in the machine.

The impact that grounding locations have on arc stability and repeatability was tested by grounding the welder to a custom built installed grounding post (as seen in figure 3.4), grounding it to the baseplate of the enclosure, and grounding it to the clamps holding the substrate down. While each of these methods worked, it was found that there was more apparent arc stability in deposition, especially when building taller parts, when grounding is performed at the clamps, close to the substrate.

Keeping every part of the equipment clean was very important for successful magnesium deposition. The contact tip and weld nozzle should be cleaned after every 10 minutes of welding by wiping the parts down with a rag to remove any soot and spatter that attached to them. If a thick layer of soot or any metal deposits are attached rigidly to the contact tip, the part must be replaced. The PLA liner should be removed from the weld hose after every hour of welding, be inspected for internal debris, and then blown clean with high pressure air. The Lube-matic pads need to be inspected frequently and changed out as needed.

4.2 Determination of functional parameters

When welding magnesium it is important to make sure that the weld hose is as straight as possible so that it is easier for the wire feeder to push the material through the weld hose and torch. An excessive number of bends in the weld hose will lead to slipping of the feeder rollers and result in weld failure. The inverter needs to be placed a safe distance away from the deposition area.

Establishing the initial parameters was best done manually off of the CNC and on a certified weld table. This ensured that the unpredictable outputs by the welder will not result in damage inflicted to the CNC being used. Proper safety gear in the form of welding shirts, gloves, and helmets need to be worn to prevent serious injury. A

Class-D fire extinguisher must be readily available to put out any magnesium fires that could occur.

There are no dedicated magnesium material settings on commercial welders, which is why aluminum material settings are used as the starting point for finding functional parameters for magnesium. As has been demonstrated in chapter 3.3.1, the inverter outputs were drastically different than the inputs. Furthermore, the weld parameters of voltage and current could not be tuned independently without changing one another. Therefore, a different approach had to be taken to find usable settings.

Numerous tests were performed where either voltage or current was held constant on the machine, and the other parameter was increased incrementally while output measurements were performed. Voltages were increased in increments of 0.5 V with currents held constant, and currents were increased in increments of 10 A with voltages held constant. For these experiments, the resulting quality of the weld bead was not of concern, but rather the output parameters alone were of interest.

Through the literature review it was seen that in TIG welding of magnesium, a heat input rate of around 1800 W worked well. Using the collected welder output data, a voltage/current combination that would yield 1800 W was determined. Since the parasitic voltage increase at increasing set currents displayed a more linear trend than the current output, the current was locked in place and the voltage was adjusted to obtain parameters that resulted in decent deposition of the bead. Bead deposition success for these initial tests was determined by inspecting the surface of the bead for porosity, examining the penetration to the base plate, and the overall consistency of the weld bead shape.

It was quickly discovered that low watt deposition parameters would yield caterpillar shaped beads with excellent bead continuity and high watt deposition parameters would yield flatter beads suitable for overlap for wider base layers. Once two sets of parameters were established, the tuning of the beads was then no longer achieved with inverter settings but instead with torch travel speeds and workpiece offsets, as from this point on all continued testing was performed on the custom CNC that was built in this research. The initial low-IER parameters that were first tested on the CNC were a set current/voltage of 165A/13V, which resulted in an inverter output of 100A/16V. The initial high-IER parameters that were first tested on the CNC were a set current/voltage of 220A/15V, which resulted in an inverter output of 160 A/19V.

As previously stated, the WFS in MIG welding is coupled to the set current, so it was very important to have the correct TTS for deposition. For the found settings, the appropriate TTS was established first. This was done with a nozzle to workpiece offset of 10 mm. A 2-inch gauge was placed on top of the substrates to correctly set the G54 zero for the z-axis in the G-codes that were used. With the found parameters, different torch speeds were tested between 200 mm/min to 800 mm/min for the low-IER settings and between 400 mm/min to 1,200 mm/min with the high-IER settings. These tests were performed in increments of 50 mm/min. After each test the bead was inspected.

By this method it was determined that for low-IER setting a TTS between 300mm/min to 500mm/min would yield good weld beads for multilayer single wall structures, and for high-IER a TTS between 500 mm/min to 850 mm/min would yield result in the desired bead shape. A TTS outside these ranges yields to intermittent deposition when moving too fast or severe burn back due to rapid material build up when moving too slow. With the newly established inverter parameters and TTSs, now the inverter parameters themselves were tuned with minor adjustments. The heat input was lowered and increased for both IER ranges until there was severe pushback on the lower heat input side, and excessive side flow due to overheating on the high heat input side. The final functional coupled parameter ranges for low and high-IER were established in this way via a very large number of test runs. Low-IER settings resulted in weld heat inputs of 153 J/mm to 354 J/mm within the specified power/TTS range, and high-IER settings resulted in weld heat inputs of 191J/mm to 364 J/mm within the specified test range.

Once successful deposition parameters have been established, the nozzle to workpiece offset should be optimized. Offset distances between 8 mm and 16 mm were tested in increments of 1 mm. If the deposited bead at a given offset was of high quality, the nozzle was removed and the contact tip and inside of the nozzle were inspected for vapor sediment or attached spatter. If potential clogging or burn back at a specific offset seemed critical, the offset was deemed too close to the part. Any offset less than 10 mm was found to be too close to the weld pool. Figure 4.2 shows how a too small offset results in spatter accumulation inside the nozzle. If this buildup gets too large, additional arcs can form between the contact tip and the nozzle.

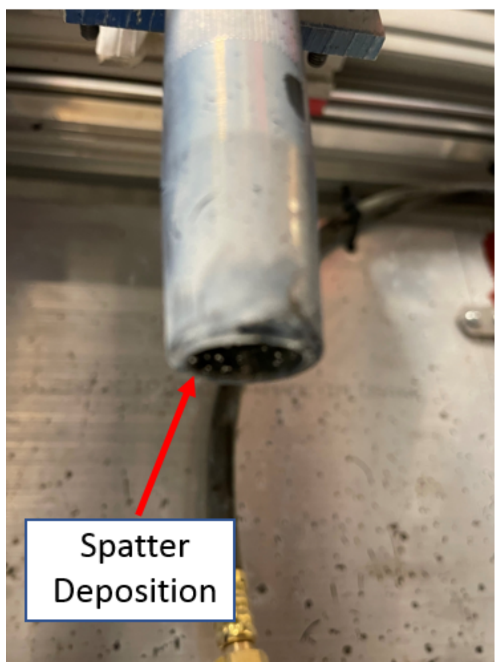

Figure 4.2: Spatter deposition inside the weld nozzle when the nozzle to workpiece offset distance is too small.

However, if the offset is too large, then the natural bend in the wire will result in curvy beads being deposited instead of straight beads. As the wire leaves the contact tip, it quickly starts to curl up and move off the centerline of the bead. This is especially dangerous when building multilayer structures. Results showed that a offset distance of above 14 mm can already have a negative impact on bead straightness, especially when deposition occurs on the uneven surface of a previously deposited bead. It was eventually determined that a nozzle to workpiece offset of 12 mm is the perfect distance to limit contamination of the contact tip and nozzle as well as for ensuring welding arcs to consistently form on the torch's traveling deposition axis, ensuring straight beads. Figure 4.3 shows how incremental changes in TTS impact the bead profile. Bead A shows lots of intermittence, indicating the TTS is far too fast. The TTS is the decreased by 50 mm/min resulting in slight improvements of the bead profile until a solid deposited bead shape is obtained in bead D. Figure 4.4 shows part 1 of the tests performed on the CNC to establish the starting deposition parameters. This is a very slow process and patience is required when starting this process with a different inverter.

Figure 4.3: Improved bead continuity as TTS is decreased in increments of 50 mm/min from bead A to bead D while providing the same IER.

Figure 4.4: Initial TTS tests performed on CNC to determine the correct deposition parameters for high and low-IER magnesium deposition.

Lastly, it is important that a consistent stick-out length be used for all the tests. As the name suggests, the stick-out is the length of the wire that sticks out of the weld nozzle at the beginning of deposition. Deposition begins with the spark of the weld arc, not with the starting motion of the weld torch. It must therefore be determined how long after the welder is engaged the wire will get close enough to the part to start the arc. This will depend on the WFS that is being used during the tests, but does not vary all too greatly even between 8 m/min and 17 m/min WFS due to the short distance of travel. The torch should also not start moving as soon as the arc is formed. The initial penetration to the substrate is key in the formation of the rest of the weld bead. The proper dwell time needs to be established to ensure even deposition. This is particularly important when adding layers on top of each other. It was found that for all tested WFS values, a dwell time of 1 second can be coded into the G-code to ensure ample start penetration of the bead. Additionally, a pre-weld 1.5 second argon purge is set on the welder to blow out any dust, as well as a 10 second post-weld argon purge time to provide additional cooling of the contact tip.

4.3 Determination of build patterns

4.3.1 Multilayer single wall build methodology

The simplest multilayer structures to print are stacked single bead walls. Using the previously discovered printing parameters, a single bead was deposited on the substrate. The height of the bead was measured at 3 points along the length of the bead. If the three measurements are within 3 mm of each other, the next layer can be deposited. It was determined that the locations of the start and the end of the beads should be switched as layers are built up to ensure a uniform wall height. The second bead of the wall will flatten the bottom layer and add 2 to 3 mm less material in the build height direction. The remainder of the beads will stay as flat and wide as the second bead deposited. The exact layer addition and bead width of the walls depend on the inverter parameters and the TTS that is being tested. Results for optimal settings have been presented in chapter 3.

Intermittence caused by droplet detachment problems or weld wire defects need to be expected. It was therefore necessary to be prepared to shut down the machine immediately via an emergency stop when any irregularities were observed during deposition. The sound and light coming from the weld region is an indication of deposition problems, and it took much practice to identify those issues quickly. If the machine is immediately stopped, the layer can be fixed with the proper method. It was found through many trials that the best way to fix a layer is by running a correction bead into the defect from the opposite side and continue the deposition until the torch has passed 3 mm past the start of the defect. This was also shown in the beginning of chapter 3.

4.3.2 MRML block build methodology

For thicker wall structure, the beads needed to be overlapped. As was previously discussed, the low viscosity of the melted magnesium makes this typically easy process impossible as severe side flow out of the weld pool occurs, rendering the layers uneven and useless. Even overlap percentages as low as 10% were still suffering from this problem, so it was decided to build each layer utilizing a stagger, channel creating method. Layers were spaced apart of one another creating channels of different widths that would result in eventual bead overlap percentages between 50% and 20% when the channel was filled. The seams between the staggered weld beads needed to be examined for fusion to determine if the method will result in a dense work piece. The layer height also needed to be examined to make sure there can be a constant z-height for each subsequent layer. This layer height can vary depending on the stagger pattern that is used. A downside of this method is that the part will need to be built with a ramp-like side in order to reduce loafing off the edges of the part. However, the excellent shape retention makes this a viable method for long, thick walled parts with reasonable heights.

Another great benefit of these channel welds is the elimination of arc wandering. A big problem during the overlapping of beads in current WAAM methods is that the arc has a tendency to form at different locations on the workpiece. With these channel welds, there is no surrounding material that could pull the arc away from the center of the deposition line.

It should be repeated that only high-IER parameters should be used for the MRML depositions. The bead profile of low-IER beads does not lend itself to overlap of channel welds, and the lack of heat also results in severe lack of fusion away from the considerably smaller weld pool. The best way of determining the optimal pattern is by printing small pyramids with short, 50 mm long, bead base layers, consisting of eight beads, and channels of varying widths for each pyramid. The final printed pyramid should then be machined by incrementally removing 2 to 5 mm of material across the triangular face. After each layer removal, the exposed face should be examined visually for any large defects. This is not as exact as performing a XCT scan, but it is much faster and will result in a much shorter time to arrive at the final desired settings.

4.3.3 Hollow cylinder build methodology

Establishing the correct building strategy for hollow cylinders, or any closed form structure, required the same initial steps as those tests performed for building stacked single bead walls, with the only difference being the closure of the shape. Extensive testing was performed to determine what the best method is to create a closed shape with uniform bead thickness and height throughout each layer. Multiple start/stop deposition locations and dwell times were tested. If the weld stops at the same position as it started, the layer will not be evenly connected as the crater at the end of the weld bead will result in a tail-like connection that gets more prominent with each added layer. If a crater-fill or dwell operation is applied at the same start/end point, the previously deposited start of the bead gets extremely flattened and starts flowing off the side of the part. The best method discovered was to run the end of the bead 3 mm past the original start point at a constant TTS. Doing so will result in a good closure of the bead and lead to a almost uniform layer height.

In addition to this method, every additional layer should be started at a different location than the previous one. Tests were performed for rotating the start/stop position by 90 degrees and by 180 degrees, with both methods resulting in excellent layer height retention. For both hollow cylinder and wall prints it was also discovered that while increases in TTS at a constant IER will lead to virtually no part thickness increases and only layer height increases, an increase in IER can be used to print thicker parts, even with increased TTS. This is of course due to the strong flattening effect that the high-IER heat source has on the layers it is being applied to.

CHAPTER 5: MATERIAL TESTING AND RESULTS

5.1 Sample preparation

Several tests were performed to analyze the quality of the printed magnesium parts, including tensile tests, SEM analyses of the fracture surface, microstructure analysis via micrographs, and X-ray Computed Tomography (XCT) of the printed cylinders to analyze internal defects such as porosity. This chapter summarizes how the test specimens were prepared, how the testing processes were completed, and the final results.

5.1.1 Thin-wall tensile test specimens

Before tensile test specimens could be machined out of the single-bead multi-layer walls, it first had to be determined how much material needs to be removed from the sides until the loafing zone has been completely removed. This had to be done incrementally, making this a relatively slow process. Two approaches were tried to get the printed walls machined into flat pieces: vertical thin-wall milling and face milling.

For the thin-wall milling approach, thickness measurements of the walls were taken as well as measurements to estimate the depth of the loafing region. The substrate was then placed in a vice in the Mori Seiki. Due to the warp of the substrate, the walls would not stand straight inside the vice on top of the parallels. To adjust for any tilt, the B and C axes in the Mori Seiki were unlocked, the cutting tool was lowered next to the wall, and the B and C rotations were manually manipulated until the proper orientation was established. Thin-wall milling techniques for aluminum were used to create a tool path that would result in the least amount of chatter. This strategy requires for the part to be machined to the final dimensions at each Z-level to keep it as stiff as possible throughout the machining process to avoid chatter. The part was created in Fusion 360, the stock dimensions were estimated based on measurements, and the G-code was created. The tool paths and final machined first block in this manner are shown in figure 5.1.

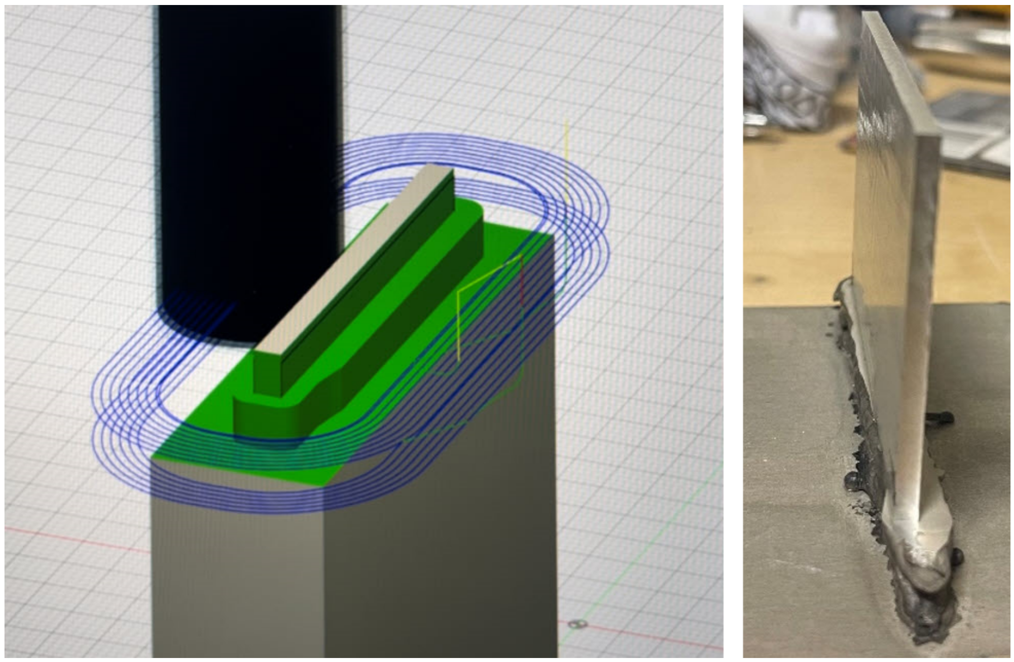

Figure 5.1: Thin-wall machining tool path for removal of loading regions (left) and final machined magnesium wall with 4 mm thickness (right).

As can be seen in figure 5.1, even though great care was take in finding the center of the part, the actual centerline of the wall was missed. If the entire process of deposition and machining were done on a thicker substrate and on a machine with integrated milling capabilities, this of course would not happen. Additionally, it was fortunate that in the case of this first sample, all loafing zones were completely removed, and tensile test specimens could now be produced. The second wall that was machined with this method encountered the problem of still showing divots from the loafing zones. This required additional machining of the now even thinner wall. The very low elastic modulus of the material, along with a very small required depth of cut, made the danger of severe chatter even higher. As expected, chatter was unavoidable. Figure 5.2 displays the severity of the chatter.

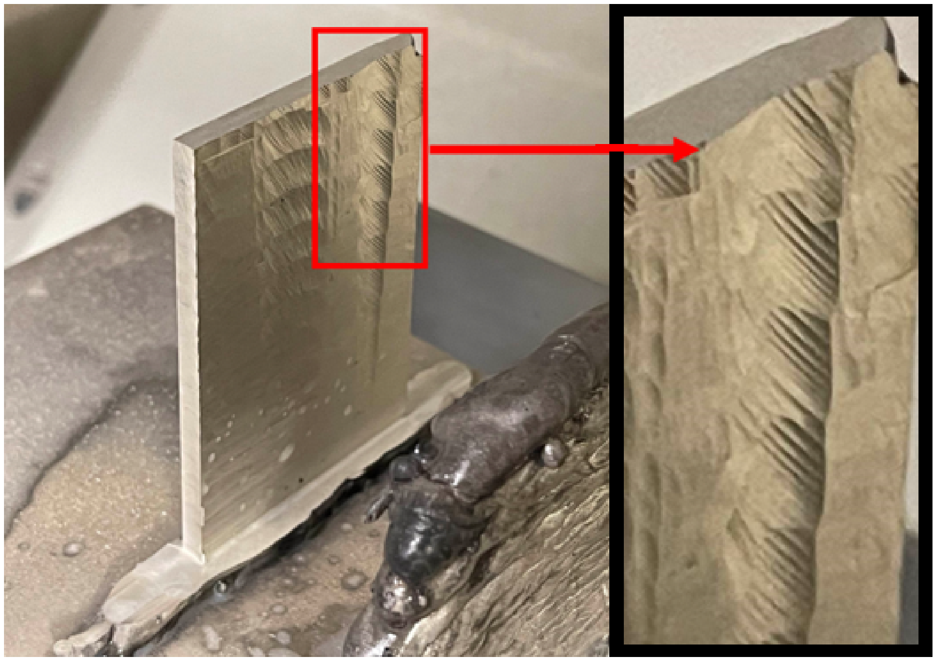

Figure 5.2: Severe chatter marks caused by insufficient depth of cut during thin wall machining of AZ61a.

Fortunately, most of the part could later be saved and used for tensile test coupon production. To avoid potentially losing any additional samples due to chatter, the remaining walls were machined differently. The walls were removed from the substrate, secured in a machine vice oriented on their sides, and then face milled until no loafing zone defects remained. This method completely removed the presence of chatter instabilities.

For continuity in tensile testing, all printed walls were machined down to a thickness of 3 mm each. Subsized tensile test specimens were then removed from these blocks using Wire Electrical Discharge Machining (WEDM). These samples were machined in two orientation: normal to the tensile test pull force and in-line with the pull force. Figure 5.3-left shows the dimensions of the 3 mm thick samples, having a total length of 40 mm and a gauge length of 12.5 mm. The right image of figure 5.3 shows the extracted samples from wall A. The lines on the left-most sample indicate the print direction of the wall. The middle 5 samples show how the samples looked directly after WEDM and the far-right sample depicted shows a cleaned specimen ready for testing.

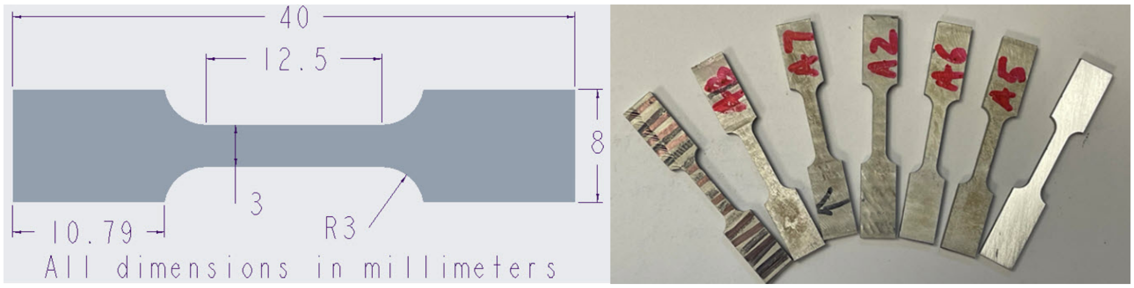

Figure 5.3: Subsized tensile test coupon dimensions for printed wall samples (left) and example of extracted samples from wall A (right).

Samples from walls B, C, and D were extracted in the same manner. Samples from walls A and C were extracted with layers deposited normal to the tensile test pull force direction while samples from wall B and D will had the load applied in-line with the printed direction. Figure 5.4 depicts the samples extracted from walls B and C in the left and middle images, respectively. The right image in figure 5.4 shows how the samples were directly extracted from staggered wall D and were prepared to have the tensile test pull force in line with the deposition direction. In the case of walls A and C, the samples were extracted vertically.

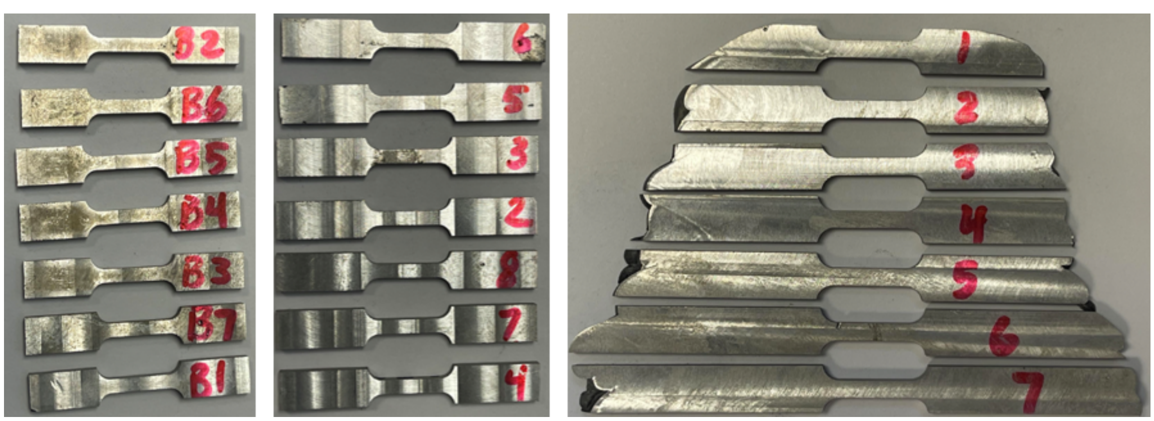

Figure 5.4: Tensile test coupons extracted via wEDM from wall B (left), wall C (middle), and wall D(right).

5.1.2 Multi-row/multi-layer tensile test specimens

The tensile test specimens were removed slightly different from the large blocks. Instead of milling the printed blocks down to the desired thickness first, WEDM was used to cut out the outline of ASTM E8 standard tensile test coupons that were the thickness of the entire block plus the substrate. The resulting parts were then further cut using WEDM to the desired thickness of 6 mm. Figure 5.5 displays the dimensions of the specimens in the right image and the obtained samples from the top layer (A) of the block in the left image. Figure 5.6 shows the extracted samples along with their block of origin.

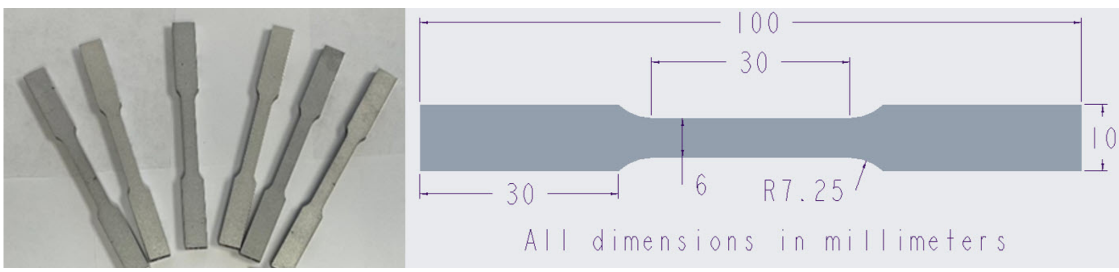

Figure 5.5: Tensile test specimens extracted from large magnesium block printed with short beads (left) and dimensions for ASTM-E8 subsize tensile test specimens (right).

Figure 5.6: Example of wEDM tensile test coupon extraction from large WAAM printed magnesium blocks.

The same method was applied to the block that was printed in-line with the tensile pull force direction. The block and tensile specimen examples from that block are shown in Figure 5.7 on the left and right, respectively. As can be seen in the right image, this method did result in visible defects, as expected. The fluidity of the material during these long deposition paths led to the lack of fusion between parts of layers, which resulted in voids. However, these samples were still tested and provided good results.

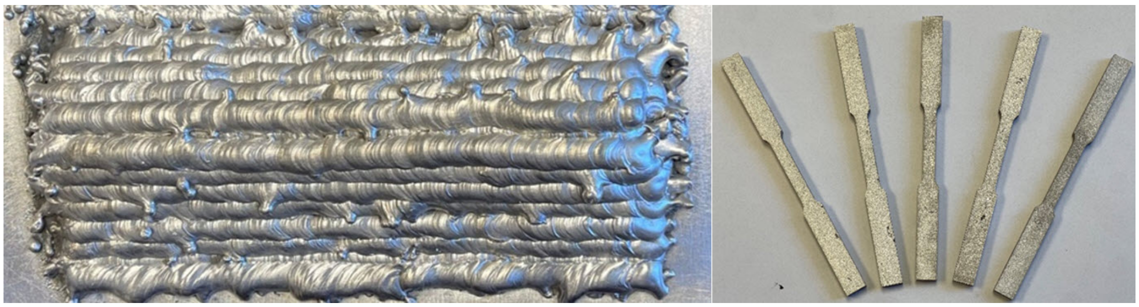

Figure 5.7: Long-bead printed magnesium block (left) and resulting tensile test samples after being extracted via wEDM (right).

5.1.3 Hollow-cylinder machining

The printed hollow-cylinders were machined in a similar method used in the preparation of the thin-wall samples. The substrate was clamped in the Mori Seiki using toe-clamps. The substrate was only slightly warped in this case and the forces applied by the clamps flattened it out in the machine. The center of the cylinders was determined by inspection. Due to the uneven surface of these printed parts, probes can'y be used to find the exact center, thus a manual method was employed. Once the center was set, the outside walls of the cylinders were incrementally reduced until no defects from the loafing zone were visible. The process was then repeated for the internal walls of the cylinders. The threat of chatter in these cases was not present due to the shape of the part being machined. No chatter was encountered, even during the machining of the smallest cylinder, which had a wall thickness of only 1.5 mm. The left image in figure 5.8 shows two of the printed parts in the Mori Seiki, and the right image shows the final machined cylinders.

Figure 5.8: AZ31b Substrate with high and low-IER printed AZ61a cylinders fastened in the Mori Seiki ready for outer layer removal (left) and finished machined parts (right).

The parts were then removed from the substrates with a vertical band saw. Before machining, the larger cylinder had height of 7.5 cm, and inner and outer diameters of 6 cm and 4.2 cm, respectively. The final machined cylinder had a height of 6 cm, a wall thickness of 4 mm, and an outer diameter of 5.4 cm. The smaller cylinder started with a height of 5.4 cm and an outer and inner diameter of 5.3 cm and 4.7 cm, respectively. A final machined height of 3.5 cm, with a wall thickness of 1.5 mm and an outer diameter of 5.1 cm were obtained. It should be noted that the final wall thicknesses of both these cylinders could have been more if the center of the prints could have been more efficiently established. Figure 5.9 shows the parts removed from the substrate. By visual inspection no surface defects were found.

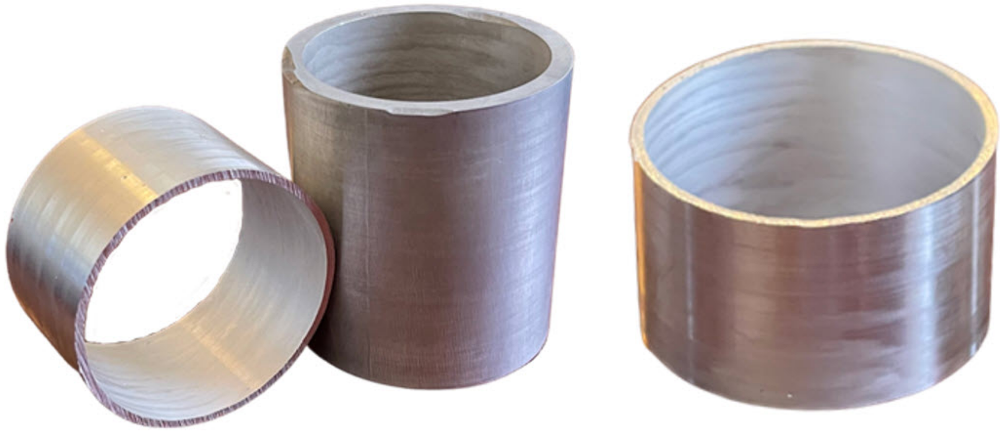

Figure 5.9: Final machined hollow-cylinders printed from AZ61a magnesium after being removed from the substrate.

Porosity and other internal defects were to be examined for the thicker walled cylinder via XCT scans. To ensure that a small enough voxel size can be used on the test machine, this large cylinder had to be cut into further sections. The cylinder was placed in a lathe and parted to create one continuous section with the height of 23 mm. This part can be seen in the right image of figure 5.10. The remainder of the cylinder was then cut into sections on a vertical band saw in 30-degree increments. The smaller size of these samples will ensure that the smallest voxel size possible can be used while still capturing the whole piece. These cut sections are displayed in the right image of figure 5.10.

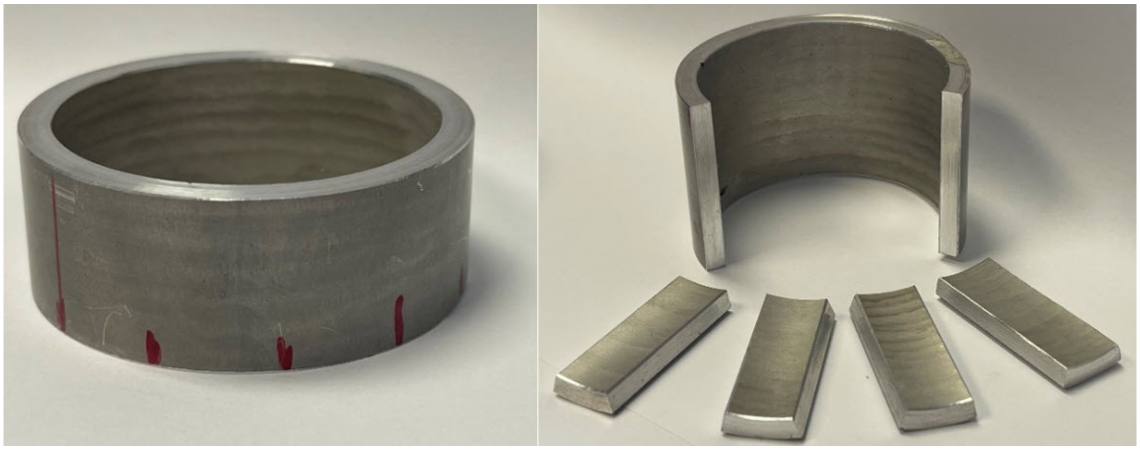

Figure 5.10: Whole cylindrical magnesium sample for XCT scan (left) and cylinder segments extracted from AZ61a printed cylinder for higher resolution XCT scan (right).

5.2 Tensile test results

5.2.1 Thin-wall tensile test results

Tensile testing of the subsized samples extracted from the printed magnesium walls was performed on an Instron 5582. The samples were cleaned prior to testing to remove any surface material and to inspect for any surface defects that might be present. Tests were performed at a standard testing rate of 5.08 mm/min. A total of 13 tensile tests were performed for the normal-to-pull-force test group from walls A and C, with 6 samples coming from wall A and 7 from wall C. The combined stress-strain curves for all these samples is shown in figure 5.11.

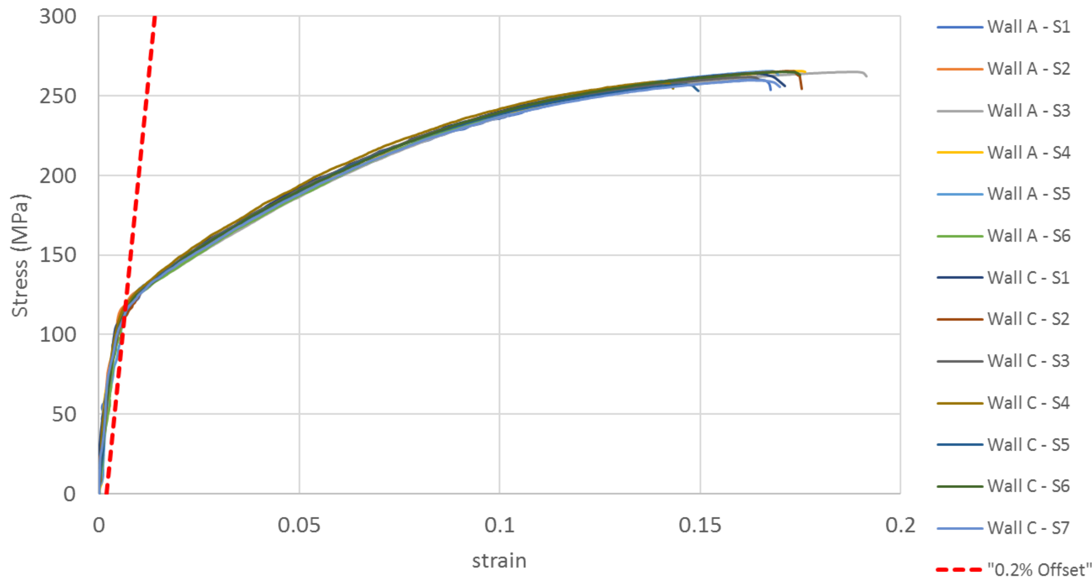

Figure 5.11: Stress-strain curves for 13 samples extracted from different magnesium walls with build deposition direction normal to the tensile test force.

As can be seen in the figure, the test results showed excellent repeatability for all the samples for the elastic region and through the plastic deformation region, making it almost impossible to distinguish between the data sets. The yield strengths (YS) for these tests lies between 113 MPa and 120 MPa, with a mean YS of 116 MPa. The only thing that set these test results apparat was the ultimate fracture point. Tables 5.1 and 5.2 show the fracture points of the samples and figure 5.12 displays a scatter plot of that data. The lowest fracture point occurred at 257 MPa with 0.1466 percent elongation and the largest fracture point occurred at 266 MPa with 0.1668 percent elongation. It should be noted that magnesium and magnesium-aluminum alloys show anelastic behavior, making the estimation of yield stresses and elastic moduli more challenging than with materials that display perfectly linear elastic behavior. For the 0.2% offset, the secant method was used in this study.

Table 5.1: Stress and strain at fracture point of tensile test samples from Wall A

	S1	S2	S3	S4	S5	S6
Stress (MPa)	261	258	265	266	266	263
Strain	0.163	0.139	0.189	0.175	0.167	0.158

Table 5.2: Stress and strain at fracture point of tensile test samples from Wall C

	S1	S2	S3	S4	S5	S6	S7
Stress (MPa)	264	265	262	259	257	265	260
Strain	0.169	0.172	0.162	0.138	0.147	0.170	0.163

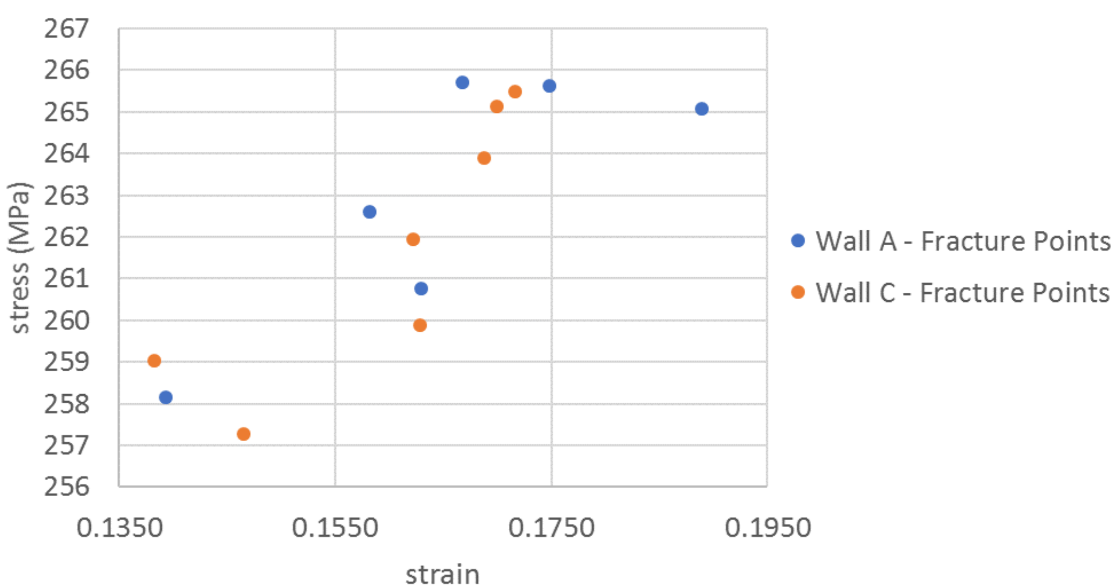

Figure 5.12: Scatter plot of fracture points for tensile test specimens from Walls A and C.

Ten tensile tests were performed for the parallel-to-pull-force test group from Walls B and D, with 6 samples coming from Wall B and 4 from Wall D. Figure 5.13 shows the combined stress-strain curves for 6 samples of Wall B and 3 samples from Wall D. One test result was omitted from these results due to apparent gripping issues at the beginning of the test, even though the test result was very similar to those of the rest.

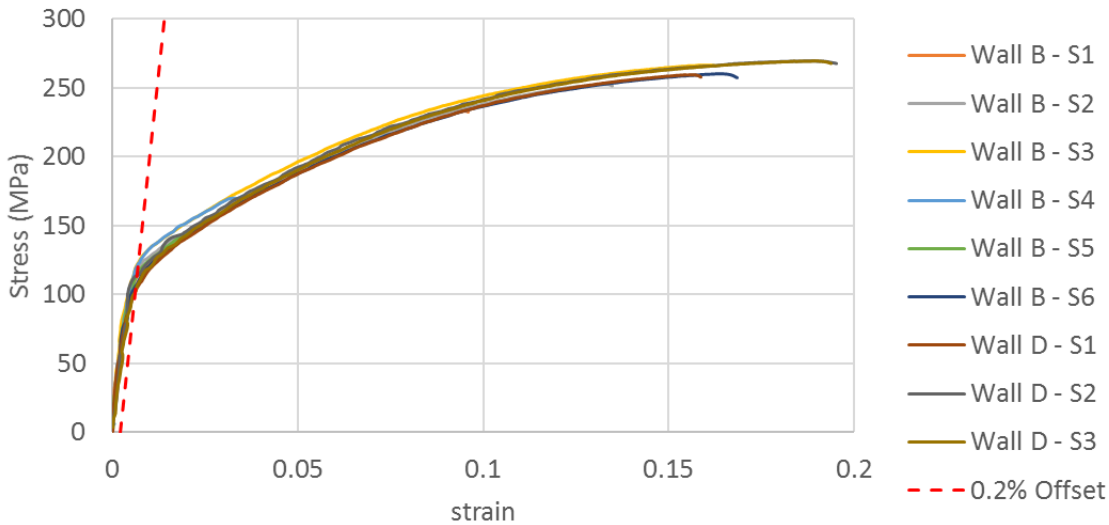

Figure 5.13: Stress-strain curves for 9 samples extracted from magnesium walls with build deposition direction in-line with the tensile test force.

Results for this group added an additional interesting find. While the results for wall B showed the same range of YS as the previously presented samples, ranging from 113 MPa to 122 MPa with a mean YS of 117 MPa, the determined YS of the three samples that came out of Wall D were slightly lower, with YS values of approximately 102 MPa to 106 MPa. This can be explained by examining the key difference in deposition for these two walls: the torch travel speed. It has been shown by Dong et. al [90], that an increase in TTS at the same IER can lead to a reduced YS. In their experiment, an increase in TTS from 402 mm/min to 600 mm/min at constant WFS resulted in a decrease in YS from 282 MPa to 261 MPa. In this experiment, wall B was deposited at the same set welding parameters as wall D, but wall B was deposited with a TTS of 300 mm/min while wall D was deposited with a TTS of 450 mm/min this resulting in a lowered YS.

As with the normal-to-pull-force group before, the main difference between the tensile test results for walls B and D are the fracture points, which are shown in figure 5.14. Most of the samples fractured at a similar stress as those determined before, with the exception of some of the samples from wall B. This can be explained by examining the machining challenge encountered when this sample was created, which was previously shown in figure 5.2. This wall suffered from extreme chatter problems during machining. It is very likely that due to the high magnitude and repeated impact from chatter that this wall exposed to, that cracks were created within the sample at some locations. These cracks would result in the lower fracture strength that was seen in this experiment. Table 5.3 shows the fracture points of these samples and figure 5.14 displays a scatter plot of that data.

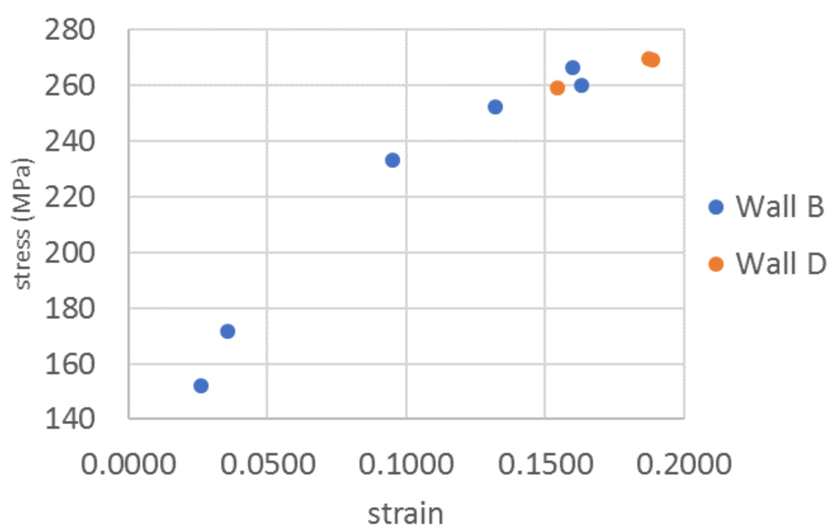

Figure 5.14: Scatter plot of fracture points for tensile test specimens from Walls B and D.

Table 5.3: Stress and strain at fracture point of tensile test samples from Walls B and D

	B-S1	B-S2	B-S3	B-S4	B-S5	B-S6	D-S1	D-S2	D-S3
Stress (MPa)	233	252	267	171	152	260	259	270	269
Strain	0.095	0.132	0.160	0.036	0.026	0.163	0.155	0.187	0.189

5.2.2 Large-block tensile test results

Tensile tests for the larger samples were again performed in the Instron 5582. The short-bead specimens with the print direction normal to the pull force were tested first. Tensile testing for these samples was considerably more challenging. Initial tests failed due to clamping issues. As can be seen in figure 5.15, the material was so soft that the Instron clamps could not hold on to the samples because they deformed the material. The cross-sectional area for these samples was four times larger than that of the thin-wall samples, and the increased required force from the Instron made it much harder for the clamps to hold on. This problem was mostly corrected when subsequent test specimens had a slightly larger portion of the grip length inserted into the clamps. Testing the samples with the longer grip length did not suffer from this problem as frequently, but unfortunately multiple data sets obtained from the Instron were not usable due to the clear presence of slipping of the sample. Figure 5.15 gives and example of how the clamps were unable to hold on to the samples causing many of them to slip during testing.

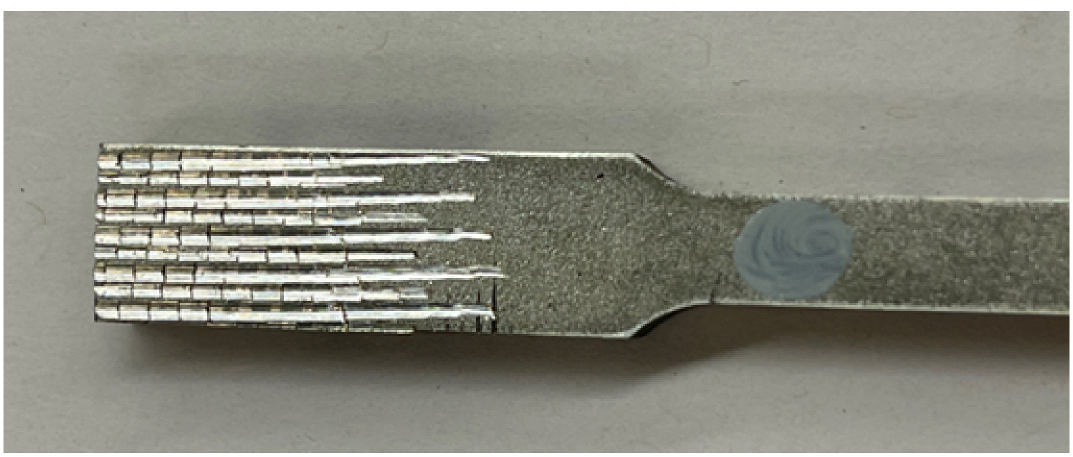

Figure 5.15: Damaged tensile test specimen grip due to slippage in the Instron 5582 clamps as tensile test force was applied.

Figure 5.16, left image, displays the combined test results for all samples that were extracted from the MRML blocks. As can be seen, one of these samples suffered from minor oscillations in the elastic region but still yielded usable results in line with the other data. The yield strength for the material was determined to be in the range of 120 MPa to 130 MPa. Determination of the exact ultimate tensile strength proved problematic due to fracture of these samples occurring at different stress magnitudes. This is due to the crack propagation that takes place inside these sample during the strain-hardening phase of the tensile test. Voids in these samples can be in the form of different size cracks, and their size and location will ultimately determine when the specimen fails. Since these samples were machined out of large printed blocks with dozens of overlapping beads, the chances of larger defects occurring were great. SEM analysis performed after these tensile tests was able to identify some of the internal defects that ultimately led to the premature fracture of the material. Even with this shortcoming, the material behavior in the elastic region during these tests remained consistent for all samples. The pattern in the plastic region also remained the same, with the primary difference being the point of fracture. The highest measured stress at the point of fracture was 174 MPa for the small-bead group, while the long-bead specimens, that were printed in-line with the Instron pull direction, reached a stress of up to 217 MPa before fracture. As previously stated, the long-bead samples also had minor cracks, but since these cracks were in-line with the applied test force, the cracks did not propagate across the test area as the material had better continuity along the direction of the pull force.

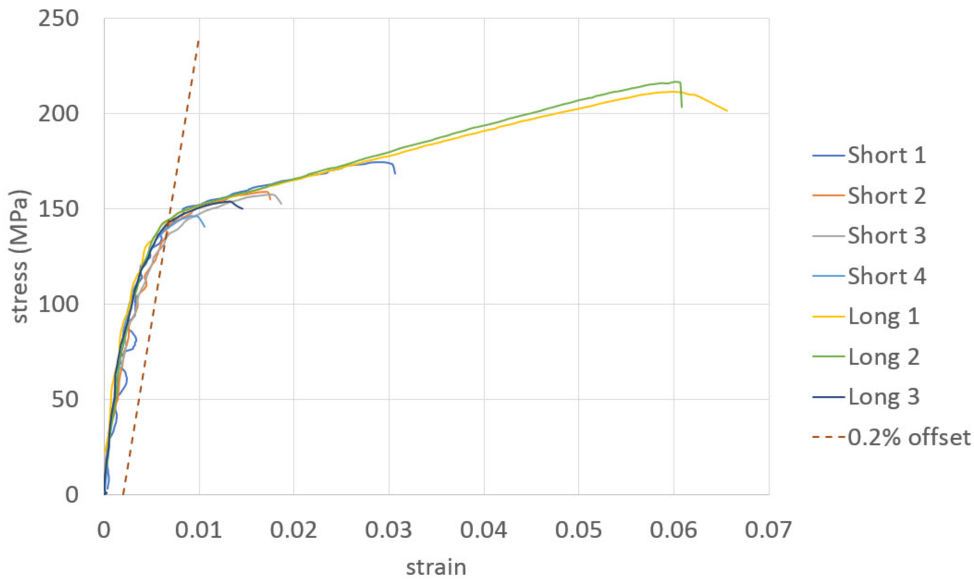

Figure 5.16: Stress-strain curve for coupons extracted from MRML blocks printed with short-beads normal to the tensile pull force direction and long-beads in line with the pull force direction.

5.3 SEM and microstructure results

5.3.1 SEM analysis

SEM analysis was performed on the fracture surface. This was not only used to determine the material behavior, but also to inspect the material for imperfections left behind from the deposition process. The following figures inspect the fracture surfaces of MRML blocks. Figure 5.17 shows two images of the fully fused surface of single wall and MRML block fracture surfaces, with the equiaxed dimples present demonstrating the behavior of ductile material.

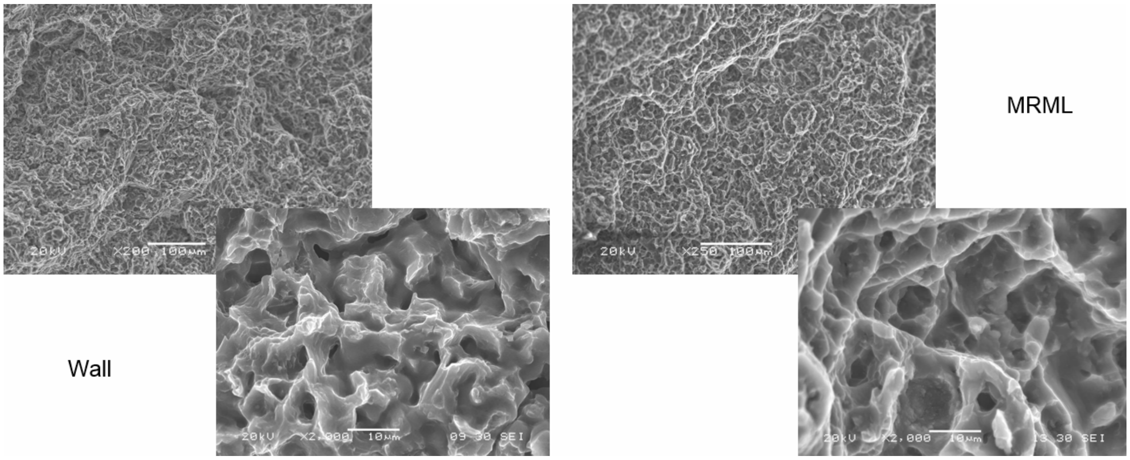

Figure 5.17: SEM images of the fracture surface of tensile test specimens extracted from thin walls (left) and of test coupons extracted from large MRML blocks (right).

The imperfections found during the SEM investigation were considerably more interesting. One of the biggest problems in both welding-AM and powder-bed AM, is the presence of spatter. Spatter can form quickly and spread to different build areas on a part. Spatter is especially a concern when working with magnesium, which is very difficult to control, especially at a rapid deposition rate and high temperatures. As mentioned before, due to the low viscosity of the magnesium alloy, it has the tendency to flow over previously deposited material before it solidifies, instead of solidifying with the weld pool. One of the dangers with this is that it could potentially trap soot or spatter inside the built part. When this happens, that trapped spatter ball creates a large air pocket inside the part. Figure 5.18 shows what appears to be a trapper spatter ball inside the structure. There is no fusion between surfaces surrounding this spatter ball as it created an air pocket around it when the melted magnesium solidified on top of it. This spatter ball is very small, only 20 μm to 40 μm in diameter, but it still managed to stay intact and cause this defect. In this research, magnesium spatter balls with diameters of up to 4 mm were observed when the process parameters were not being controlled properly. When the size of the spatter is that large, it is easily visible by the human eye. It can therefore be easily removed from the part before the next layer is being added. Of course, this correction can only take place if the spatter was not already trapped underneath a side flow layer of material.

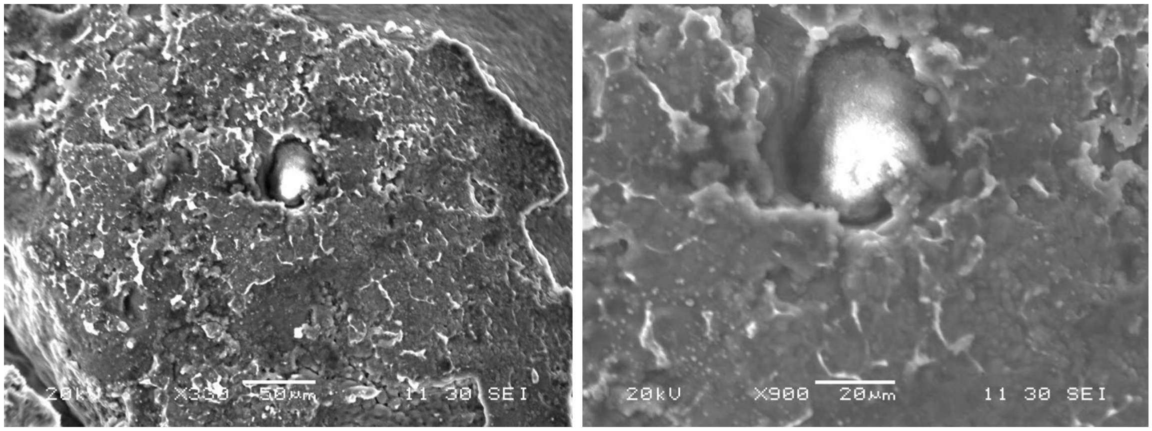

Figure 5.18: SEM image of a trapped spatter ball inside the welded material located at the fracture surface.

The presence of smaller cracks and hollow voids was also discovered, as can be seen in Figure 5.19. The left side of the image shows a small crack in the surface. Cracks and delamination are frequent defects in welding operations. These cracks can form during the cooling process or can develop from voids that are present post welding due to trapped gas. The crack in this image was almost 0.1 mm in length. The right image in figure 5.19 shows the presence of a considerably larger internal void. This void could either also stem from trapped gas or could be a channel crack that is present due to improper fusion when a channel layer was deposited. All these imperfections could be removed, but as mentioned before, this would require a custom-built inverter that can be specifically tuned for the deposition of this material. Commercially available machines can do a decent job with single or double stacked beads, but for multi-layer deposition, a custom machine would be required.

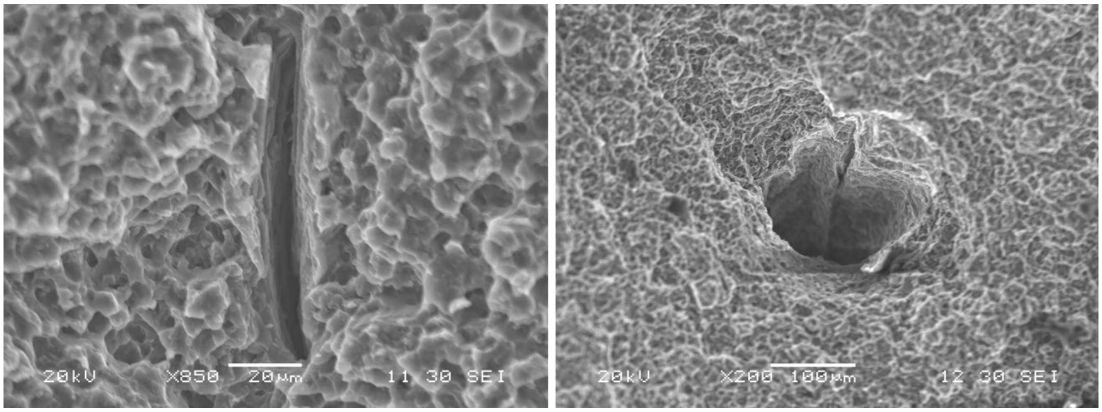

Figure 5.19: SEM images of the tensile test fracture surface revealing defects such as cracks (left) and voids (right).

SEM images were also taken of the thin-wall specimen fracture surfaces. As with the MRML blocks, the observed equiaxed dimples at the fracture surface indicate ductile behavior. Unlike with the MRML blocks, fusion occurred throughout the fracture surface, indicating that material failure at the fracture point for the thin-wall samples was not due to large defects as it was the case with the MRML blocks. These can be seen in figure 5.20.

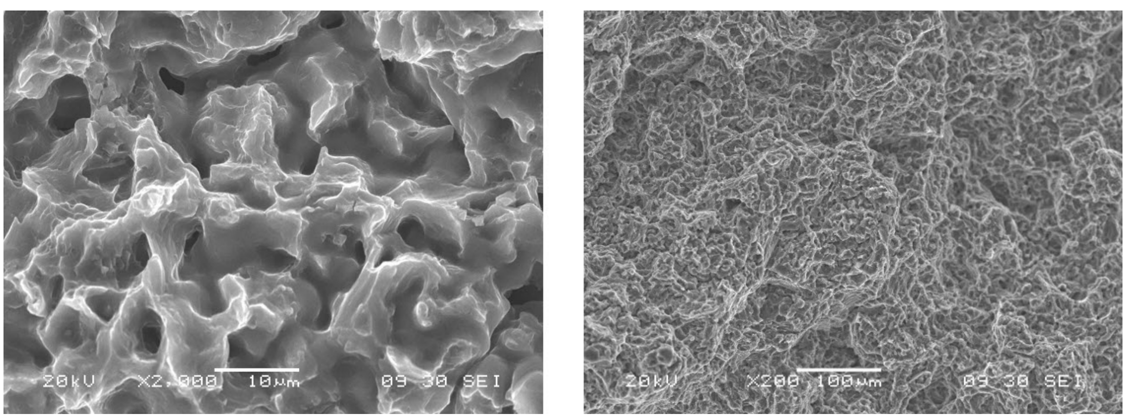

Figure 5.20: Fracture surface SEM images for thin-wall printed magnesium samples at 2,000x (left) and 200x (right).

5.3.2 Microstructure analysis

Optical micrographs were obtained from both the wall specimens and the large block specimens. Analyses were performed to examine the grain structure for the printed magnesium. Samples were prepared with sandpaper and subsequently polished. For etching of the AZ61a weld wire, it was found that a Nital solution was able to achieve the desired results. Two and four percent Nital solutions were used depending on the sample that was being investigated. The necessary etching time was 5 to 10 seconds with the four-percent solution and up to 35 seconds with the two-percent solution. These agents only worked for the AZ61a samples, which was found while attempting the analysis of the interface between the AZ61a wire material and the AZ31b substrate. A Picral etchant solution was tested to etch both materials simultaneously but was also not able to etch the substrate. However, the Picral agent was able clearly etch both the AZ61a and the interfacial layer towards the substrate, as will be seen later this section. After unsuccessful attempts to etch the substrate with the recommended etchants, Keller's solution, typically used on Aluminum, was introduced and provided excellent results for the substrate by immersing the sample for 30 seconds. While this worked for the substrate, this etchant decimated the AZ61a material. Thus, the analysis of the interface between substrate and weld material is done using three different etchants and across three separate micrographs. This analysis is located at the end of this section.

The following figures show images of the micrographs obtained for the thin-wall printed weld material samples that were analyzed. The Image Processing software Fiji-ImageJ was used to determine the average grain size for the samples that were manufactured in this manner. Some samples were also analyzed via the trainable segmentation software WEKA to get a clearer view of the final results. The AM material analysis is broken up into two section: the bulk material and the fusion zone material. As layers are added to the parts, reheating of material occurs and changes the microstructure in the interface-fusion area between these layers. This results in significant grain refinement at this interface between the deposited layers, as can be seen in the right image of figure 5.21. Figure 5.22 shows bulk-material microstructure away from the interface of the AM material for both below the interface (top right) and above the interface (top left). The bottom images in figure 5.22 show these images after being analyzed by WEKA. This was done primarily to determine the percentages of the magnesium rich α-phase and the precipitated β-phase, which consists of $Al_{12}Mg_{17}$, that are present in these samples. The α and β-phases are identified in the left image of figure 5.21.

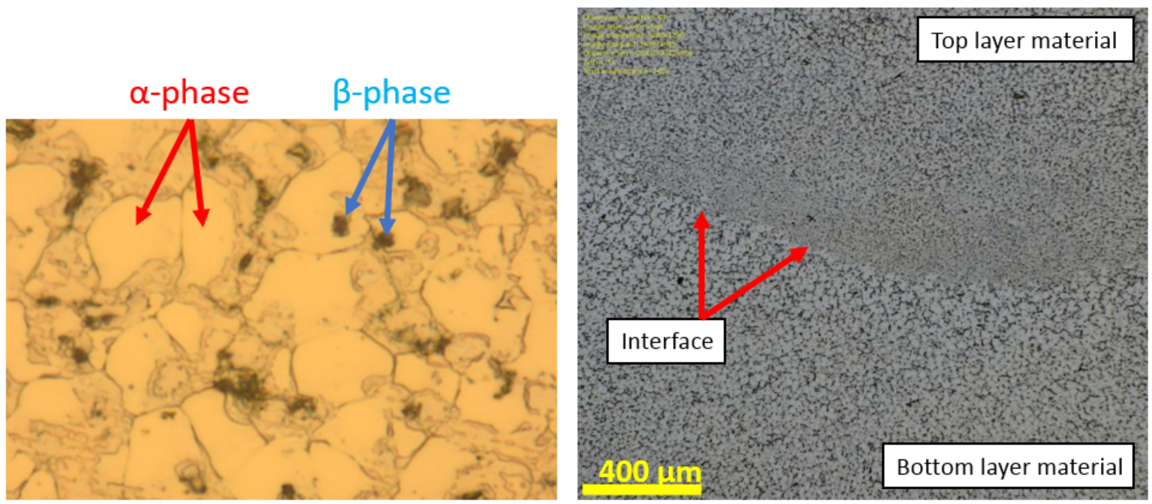

Figure 5.21: Identification of the magnesium rich α-phase and the $Al_{12}Mg_{17}$ β-phase of the microstructure (left) and the interface between two AZ61 layers showing the grain refinement at the interface due to heterogeneous nucleation due to the presence of dispersoid particles and the grain growth away from the interface layer toward the bulk material (right).

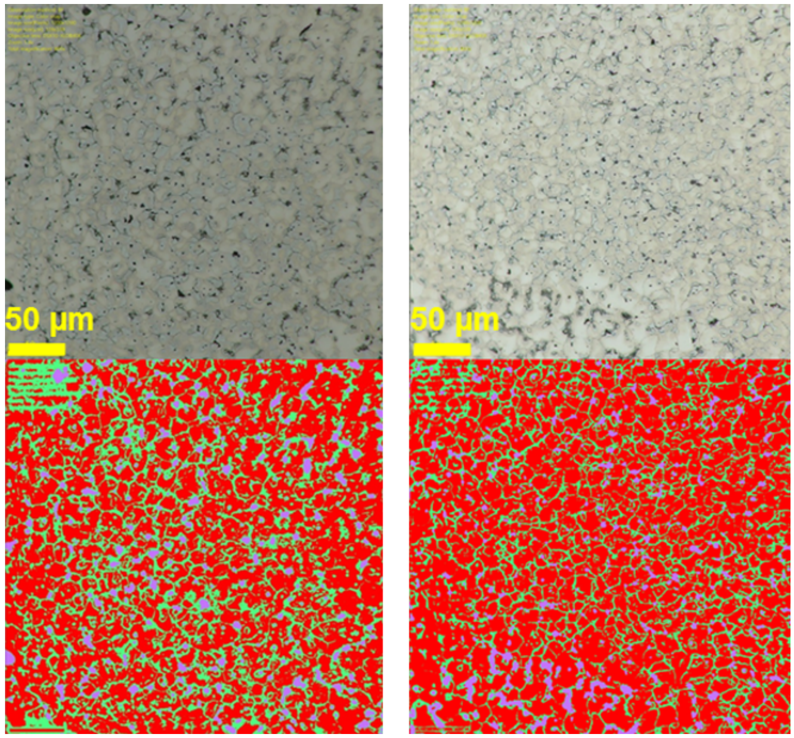

Figure 5.22: Microstructure and WEKA analysis of the bulk material above the AZ61a bead interface (left) and below the bead interface (right), used to determine grain size and phase composition.

The three classes shown in the WEKA images are α-phase grains, β-phase precipitates, and grain boundaries. By analyzing the pixel count for each class, it was established that the β-phase comprises 6.6% of the microstructure by volume, which yields a calculated weight percentage of 8.0%. Literature reviews and phase-diagram analysis of magnesium-aluminum-zinc alloys resulted in an expected AZ61a β-phase content of 7.5%, showing that the trained WEKA model accomplished its purpose.

An average grain size of 35 μm to 40 μm for the bulk-material was determined. The grain-size in the newly deposited material on the top layer refines downward to as little as 15 μm at the interface. Due to the small weld wire, the pre-weld microstructure can't be determined. However, Rajakumar et al [101] did a similar analysis of weld joints when joining two thin AZ61a plates using pulsed-GTMW. In this analysis they found that the AZ61a pre-weld material had a grain diameter of about 38 μm. Thus, while the bulk-material exhibited no change in grain size, a considerable grain size decrease as high as 23 μm, or 61 percent, was observed at the interface. The reason for the formation of this fine-grain layer was studied by Ram et al. [162] while investigating this fusion zone grain refinement in aluminum welds. Before welding, there are dispersoid particles in the material. These particles are usually dissolved by the heat of the welding process, but in a small region at the interface they survive without getting melted. Since the interface region has unique fluid flow and thermal conditions when compared to the rest of the weld material, these dispersoids are not dissolved and are also not pushed into the bulk of the weld pool. Therefore, it is by heterogeneous nucleation on these particles that these fine grains at the interface are created. Additional micrographs for the thin-walled samples are shown in Appendix D.

The following figures show the results of the microstructure analysis performed on samples from the larger MRML blocks. ImageJ was used again to determine the grain size for these samples. Figure 5.23 shows an example of the microstructure of these samples. A grain size of 12.1 μm was determined on average, with a sample measurement standard deviation of 1.1 μm. Figure 5.24 shows an additional data set from a different sample analyzed with a different optical microscope demonstrating the repeatable results. Our large block samples show significant grain refinement throughout, as the grain size was reduced by close to a factor of 3.5. This is most likely due to the relatively rapid cooling process. Since only one bead at a time was deposited with considerable interpass time being allowed, plus the addition of forced convective cooling, the bead loses its heat fast due to conduction to the surrounding material and due to the forced convection by the externally mounted fan. The presence of β-phase precipitates is prominently present in these images as well. It should be noted that grain refinement for the PGTMW method used in [67] resulted in a grain refinement down to 28 μm.

The difference in welded material grain size between the thin-wall and MRML samples is substantial. The reason for this was discussed in the literature and [8]. When building multilayer structures, the directions in which heat transfer can occur decreases, especially for conduction heat transfer. This is even more true for the single-bead thin walls that were being printed, where the only direction that conduction can take place is downward. For the MRML blocks, however, heat transfer can occur to both adjacent beads in the addition to downward into the thicker material and substrate. A simple heat transfer model was created in COMSOL multiphysics to demonstrate how the shape of the part being printed impacts the cooling rates, which in turn will impact the microstructure, as is the case in this work. The results of this model are shown in Appendix F. Additionally, convective cooling was not applied to the thin-walled builds. Due to all these reasons, the heat removal rate for the MRML prints is considerably higher throughout the process, which in turn results in more grain refinement.

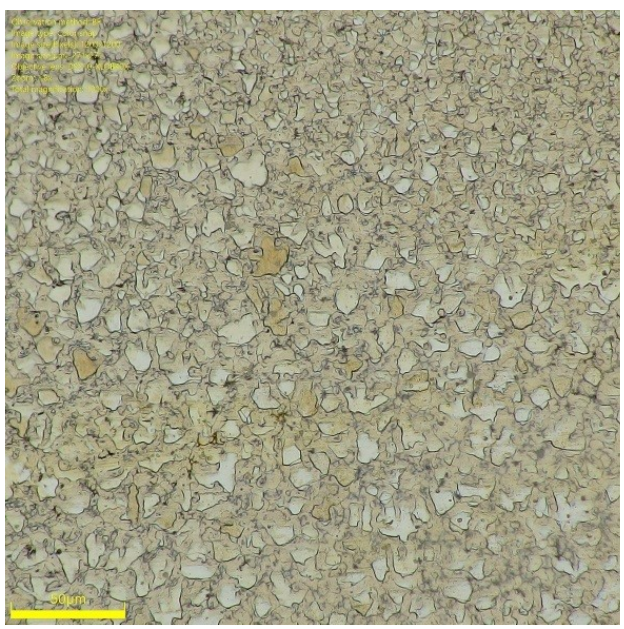

Figure 5.23: Optical micrograph of large welded magnesium block AM material etched with a 2% Nital solution for 35 seconds.

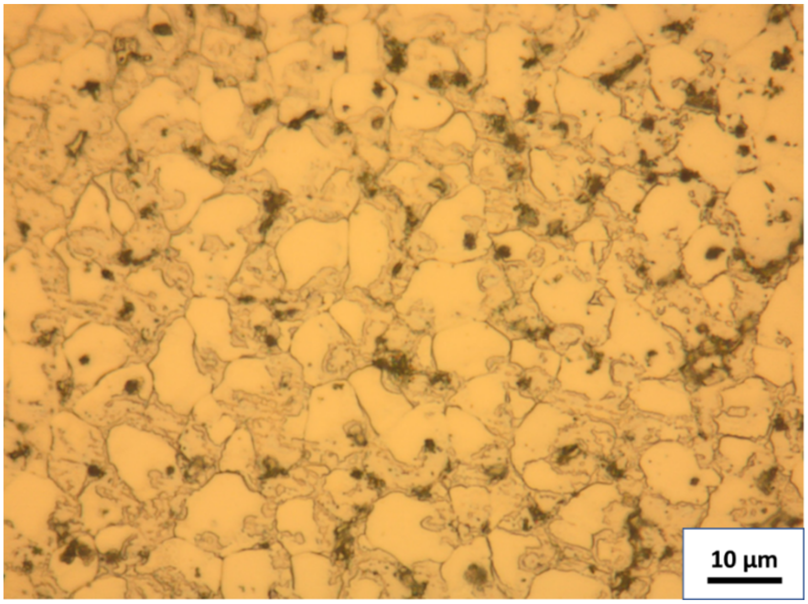

Figure 5.24: Optical micrograph of MRML magnesium block 100x etched with a 4% Nital solution for 10 seconds, showing good grain refinement for these thick printed blocks.

Lastly, an attempt was made to inspect the interface between the AZ31b substrate and the AZ61a welding material. For this analysis, samples from the MRML blocks were used because the higher input energy used while building these blocks led to deeper penetration of the substrate. Unfortunately, it was not possible to etch both materials using the available etchants, as explained at the beginning of this section. Figure 5.25 displays the interface after etching with the originally used 4% Nital solution. As can be seen in figure 5.25 (left), the weld wire material on top was nicely etched while the substrate material was unaffected by the agent. The right image in figure 5.25 shows the interface after polishing.

Figure 5.25: Interface between AZ31b substrate and AZ61a weld wire after etching with 2% Nital solution (left) and after polishing (right).

Using Picral Etch, which consists of 4% picric acid in ethanol, it was possible to clearly define both the AZ61a material, the interface boundary, and the interfacial layer. Figure 5.26 shows these zones of the interface region. As can be seen, the AZ31b substrate is not affected by the etchant. As is the case with many joining methods of two materials, there sometimes forms a thin oxide layer between the material from metal vapor. This thin layer appears only at the substrate to AM material interfaces and was not observed in any micrographs containing only AM material. The interfacial layer observed in figure 5.26 is also unique to the interfaces with the substrate. This layer is formed due to the differences in the materials. Even though AZ61a and AZ31b differ in material composition only by their individual aluminum content, this layer still forms. The particles of the two materials are mixed via fusion at the interface of the weld pool.

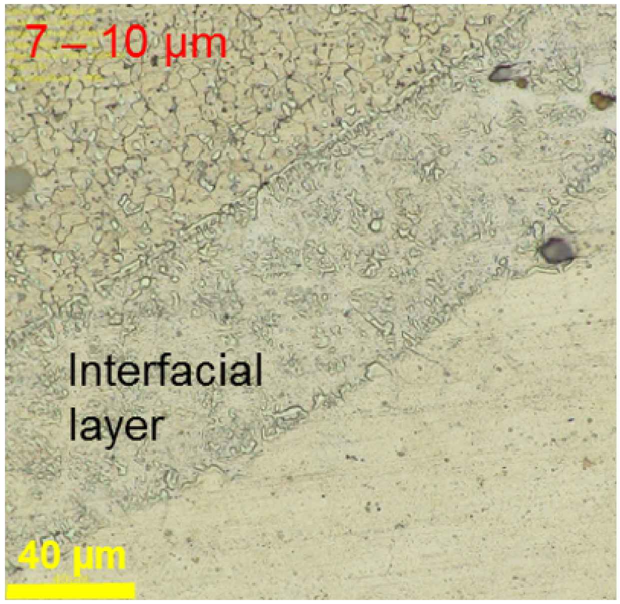

Figure 5.26: AZ31b-AZ61a interface from a MRML block etched with Picral etchant showing the development of a interfacial layer between the two alloys as well as grain refinement of the weld material down to 6 microns.

A third etchant had to be included in order to get the microstructure of the base-plate itself, AZ31b-H24. It is speculated that the heat treatment of this material is what made the etching process more challenging. Keller's Etchant, which is the ASTME Standard E-407 etchant for aluminum, was used on the interface surface. While this etchant provided good results for the AZ31b substrate, it destroyed the microstructure image of the AZ61a, as can be seen in figure 5.27. The micrograph of the substrate itself can be seen in the left image of figure 5.28, while the WEKA trained image can be seen in the right image of the same figure.

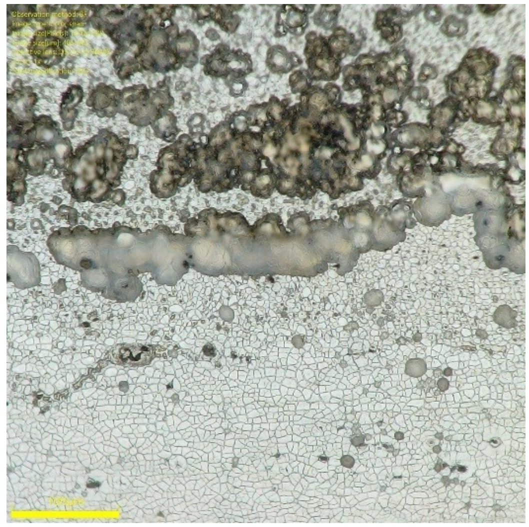

Figure 5.27: AZ31b-AZ61a interface etched with Kellers agent, which defined the grain boundaries of the AZ31b substrate but damaged with the interfacial layer and the AZ61a filler metal.

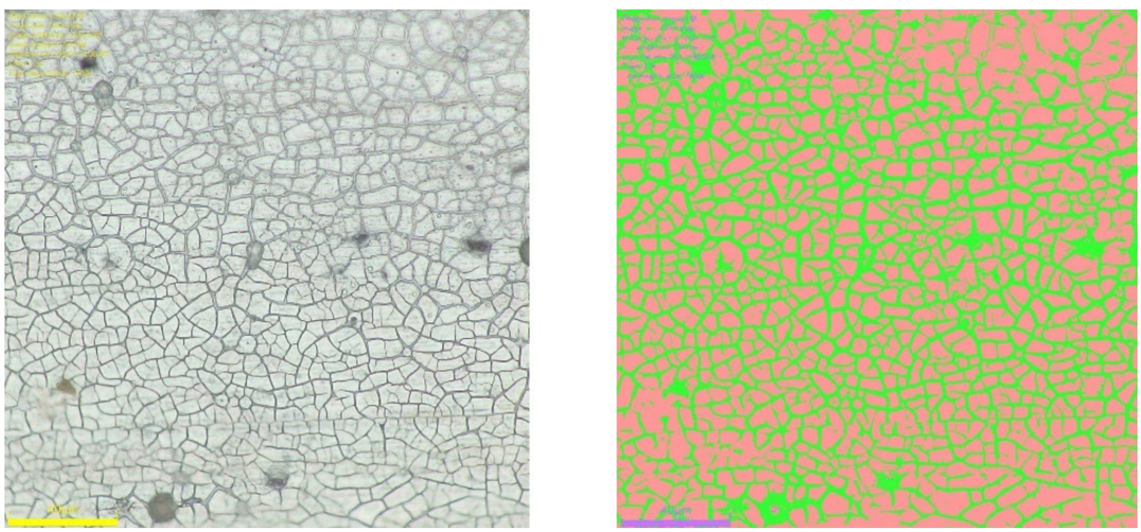

Figure 5.28: Micrograph and trained WEKA image of the bulk AZ31b microstructure.

Close to the interface, grain sizes are in the range of 6 to 8 μm. Moving away from the interface, these grains grow up toward 14 to 16 μm. As indicated in the name, H24, the substrate was partially strain hardened, resulting in the finer overall grain size seen away from the interface in the not affected zone. Grain refinement towards the interface was again also present in for the substrate.

5.4 XCT scan results - porosity

The thick-walled printed magnesium cylinder test specimens depicted in figure 5.10 were analyzed with a Zeiss Metrotom 800 CT scanner. The smaller sections were analyzed with a voxel size of 20 μm and by layer spacings measuring the same length. The larger ring was analyzed with a voxel size of 46 μm with the same length used for layer spacing. The data was analyzed using Image Processing in the 3D Segmentation module WEKA in Fiji-ImageJ to determine the %-porosity for this magnesium manufacturing method. Not much data exists on porosity in the arc welding of magnesium, so past research done on aluminum in GMAW was used to have a direct method comparison for the results of this study. In aluminum welding, a first-grade weld criteria part should have less than 0.5 %-porosity [163]. For TIG welding of magnesium, the best porosity measurements of 0.03% to 0.8% have been reported.

The image stack for each individual small section was uploaded and a training sequence was established. The three classes that the software was trained to detect were material, voids, and background. Gaussian blur, Mean, Variance, and Median training features were implemented for the qualification of the three class types. The Difference of Gaussian training feature was added to aid in the detection of borders. The training of the program was completed in iterative steps until comparison between the raw-data images and the trained-data images yielded a satisfactory result. Three separate training programs were created and executed for each of the cylinder sections, and the results for porosity were recorded. Figure 5.29 shows two examples of how the trained final program was able to detect even the smallest voids. Voids in the raw images that were virtually undetectable were picked up by the trained software. For easier reference, some of the voids in the raw-image have been circled in red.

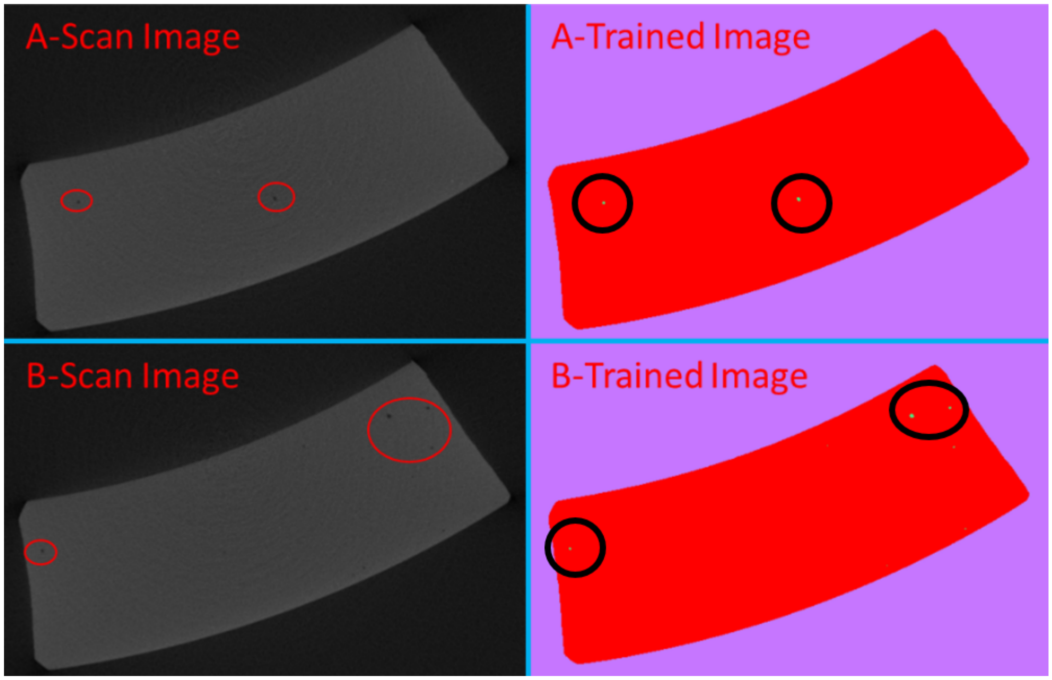

Figure 5.29: Example of two CT scan layers and their trained 3D WEKA Segmentation results for void and material identification to determine porosity of the printed cylinder segments.

After the final iteration of each training program, the %-porosity was determined in two ways. A histogram was created detailing the pixel count for each of the three classes. This histogram program includes the pixel count for all the image slices that were included in the image sequence being analyzed. The background pixel count is removed from the data, and based on the material and void classes the %-porosity is calculated. A MATLAB code was then written to calculate and plot the %-porosity for each individual layer and plot the results. As previously stated, these steps were taken for all 3 times the WEKA program was trained and the mean results are being presented in this paper.

The first segment being analyzed had a total part porosity of 0.039 %. The 3D image-stack representation of this part can be seen in figure 5.30, left image. For segment 1, 77 % of all layers have a porosity below 0.04 %, as shown in the right image of figure 5.31. The layer with the highest porosity of 0.42 % porosity was located and analyzed. This layer can be seen in the right image of figure 5.30. As can be seen in this figure, the defect is non-circular in nature and could have come from an overlapping-loafing issue during deposition caused by a defect in the weld wire.

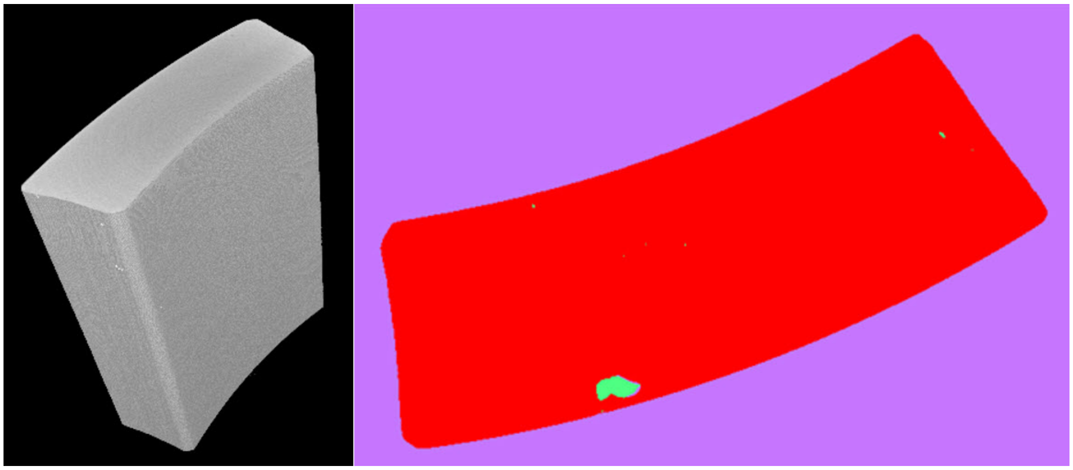

Figure 5.30: 3D representation of combined image sequence of layers from cylinder segment 1 (left) and the layer containing the highest %-porosity from segment 1 (right).

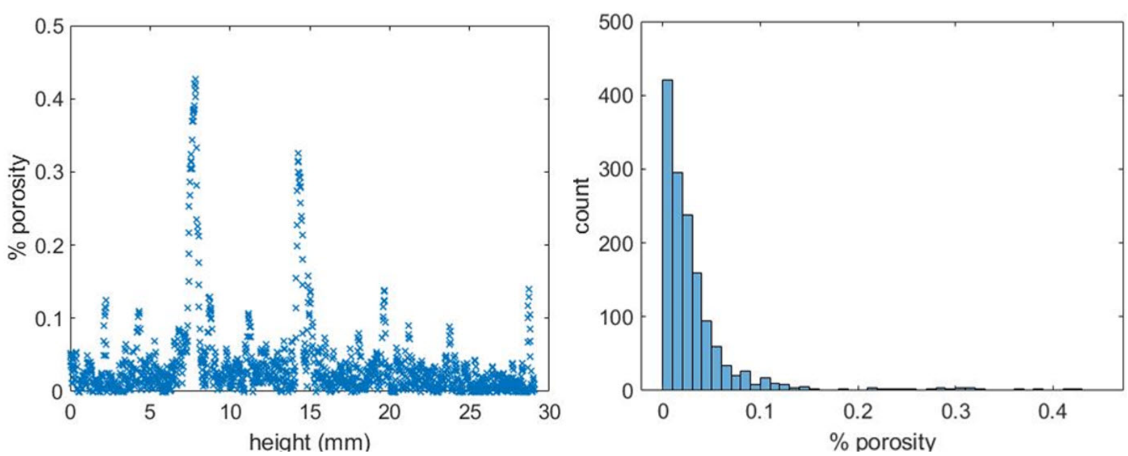

Figure 5.31: Percent porosity for segment 1 by layer slice along the length of the part (left) and frequency of percent porosity for segment 1 (right).

The other two cylinder segments were analyzed in the same way as the first. The porosity for the entire volume of section 2 was 0.039 %, with 66 % of all layers having a porosity of below 0.04 %. Figure 5.32 shows both the %-porosity by layer (left) and the histogram of the data (right). Section 3 had an elevated total porosity for the part volume of 0.07 %. Additionally, this segment also only has 50% of its layers with a porosity percentage of under 0.04 %. This section was part of a closure-zone while printing the part, which explains the increased porosity and size of defect. Figure 5.33 displays the data plots for this section. The largest defect from section 3 can be seen in figure 5.34. It is a perfectly circular defect with a radius of 0.76 mm, making it by far the biggest defect detected in any of the parts, but is by no means much larger than defects found in normal welding operations. It can be assumed that this defect occurred due to contaminants on the weld wire as the circular void indicates a trapped gas bubble. Additionally, since this location is at a closure juncture, there is already a layer of deposited vapor covering the material from when deposition began, further increasing the risk of such a defect. In order to remove such closure-zone defects, that region would need to be cleaned before closure occurs, which could be possible with an add-on to a CNC.

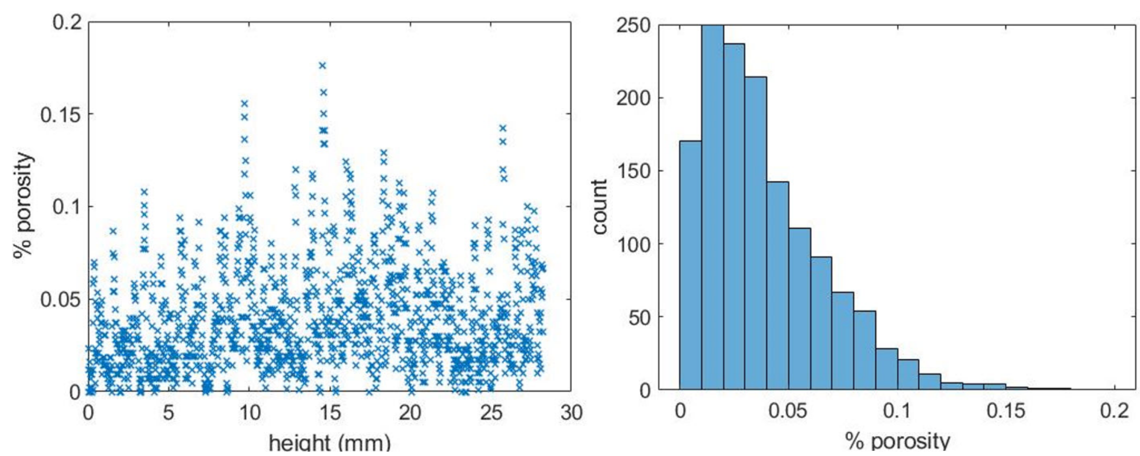

Figure 5.32: Cylinder segment 2 porosity by layer along the length of the part (left) and segment 3 porosity by layer (right).

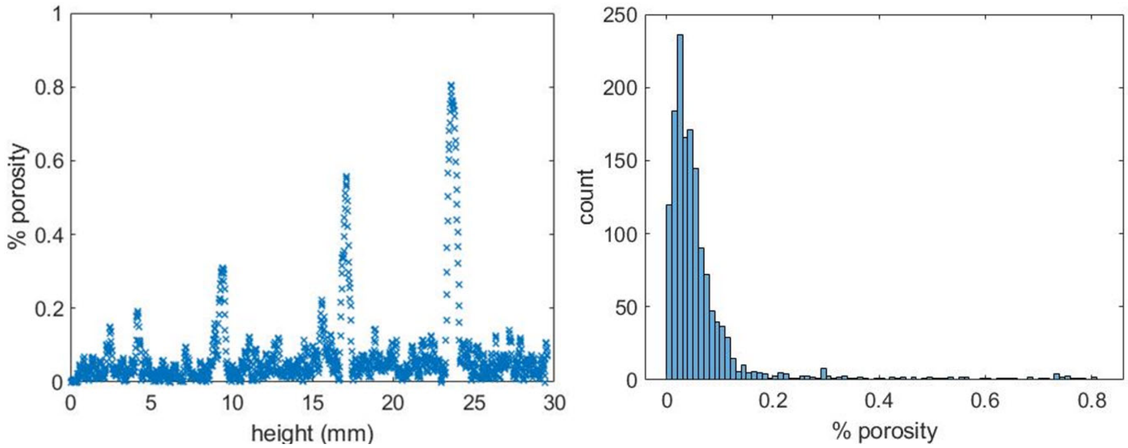

Figure 5.33: Cylinder segment 3 porosity by layer along the length of the part (left) and segment 3 porosity by layer (right).

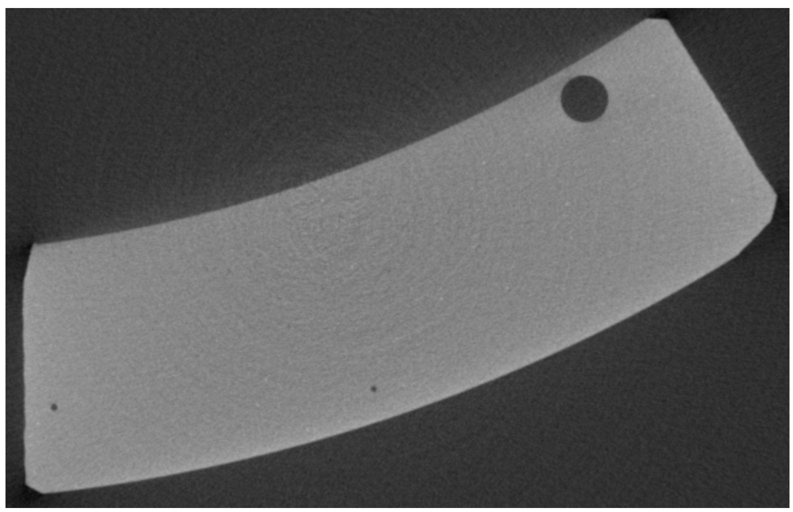

Figure 5.34: Large internal defect in cylinder segment 3 caused by the magnesium oxide layer that was deposited onto the bottom bead at the beginning of the new layer.

Analysis of the larger ring that was scanned with a voxel size of 46 μm was performed. Initial image inspection showed virtually no porosity, with a few exceptions. Due to this, the percent porosity for this specimen is not being reported because it would provide too low results. However, these scans did show the closure regions that were discussed earlier. Figure 5.35 shows the complete scan of the ring along with the marked closure regions for this printed part. For this cylinder print, the layer start locations were spaced 180 degrees apart, which in the case of the scan is the top and the bottom region of the image. Figure 5.36 shows a close up view of the defects that occur in these zones at the interfaces between beads.

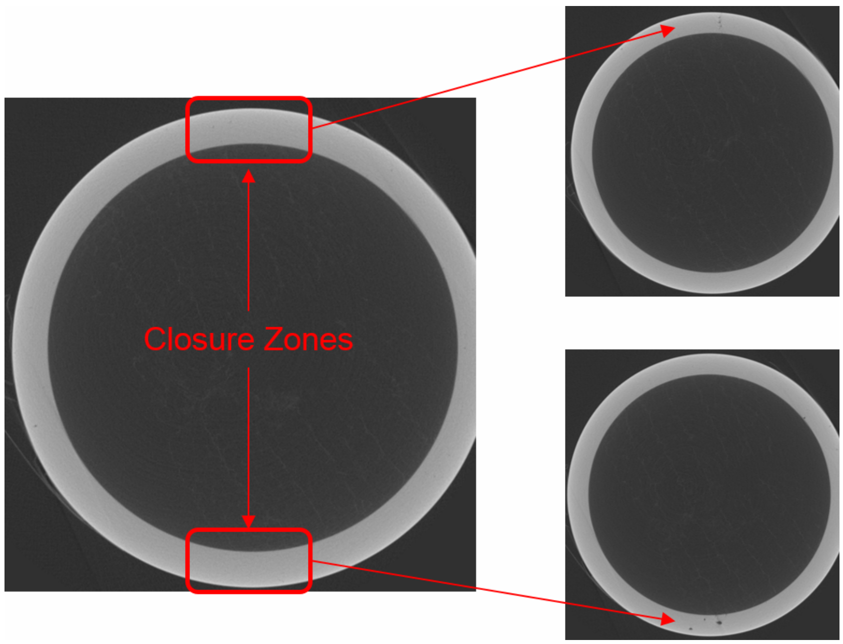

Figure 5.35: CT scan with 46 μm voxel size of cylinder indicating the location of the closure-zones for the printed part and the expected defects within this zones.

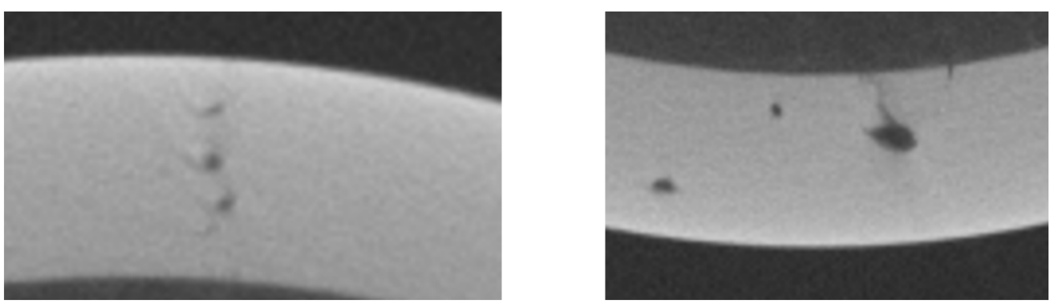

Figure 5.36: Top and bottom closure-zone defects during bead closure.

CHAPTER 6: MODELING OF MATERIAL DEPOSITION AND HEAT TRANSFER

Developing a new manufacturing method is a time consuming process. It is often beneficial to be able to create predictive models once the basic methodology of the developed process has been established. Instead of conducting numerous experiments, simulations can be used to predict what the outcome would be when certain input parameters are changed. For this exact same purpose, a multiphysics FEA model of the welding-AM deposition process was developed as part of this research. With this model, the thermal history of the printed part can be studied to determine appropriate interpass cooling times to avoid overheating issues. Additionally, the correct thickness of substrate can be selected given the desired input to reduce the chance of part distortion which can lead to internal cracking and delamination of the deposited layers. The model presented in this chapter is the first step towards a sequentially coupled thermo-mechanical simulation that can predict the heat-transfer, thermal expansion, and residual stresses remaining in multilayer WAAM produced parts. The model uses the same energy inputs, deposition parameters, and geometry of beads and substrates in order to eventually use it to predict how changes in input parameters will alter the part quality and strength.

6.1 Model geometry

Modelling of the welding process is inherently complicated as it involves multiple physics aspects, multiple transient heat transfer aspects, as well as a unique material deposition method. The material deposition in MIG welding is not via the conversion of material from one state into the next at the same location, such as in LPBF.

Instead, the filler material drops at random time steps from the tip of the weld wire onto the substrate. The substrate is heated up with the welding arc so that the weld droplets can fuse with it. COMSOL Multiphysics was used to setup a model that could simulated the material deposition and calculate the heat transfer, thus tracking the thermal history of the part. The primary goal was to develop a model that would get as close as possible to simulating the deposition process and subsequent heat transfer as it would occur in real life. The FEA model includes a 20 cm x 10 cm x 1 cm substrate onto which 9 beads are deposited, similar to how the MRML blocks were built in the experimental section. The geometry for the simulation can be seen in figure 6.1.

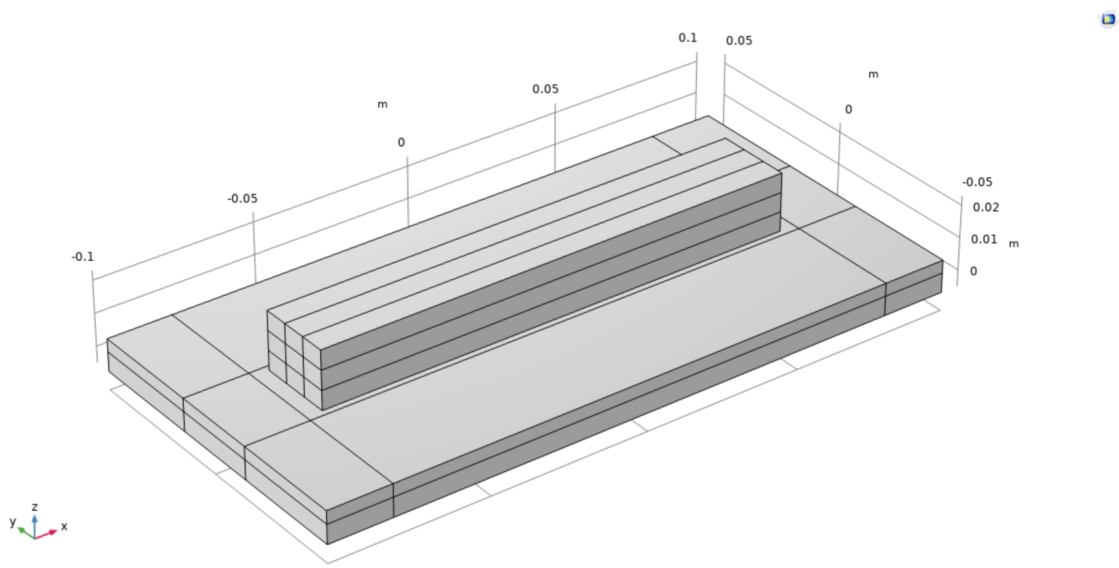

Figure 6.1: Model Geometry for additive welding operation consisting of a substrate with nine weld beads deposited in a 3x3 layer configuration.

The individual beads have a width of 8 mm, a height of 6 mm, and a length of 150 mm. They are deposited with the torch moving in the positive x-direction. Figure 6.2 shows the order in which the beads are deposited. Beads 1, 6 and 7 are deposited at y = -8 mm, beads 2, 5 and 8 are deposited at y = 0 mm, and beads 3, 4 and 9 are deposited at y = 8 mm. Therefore, this simulation would be equivalent to a zero-percent overlap deposition method.

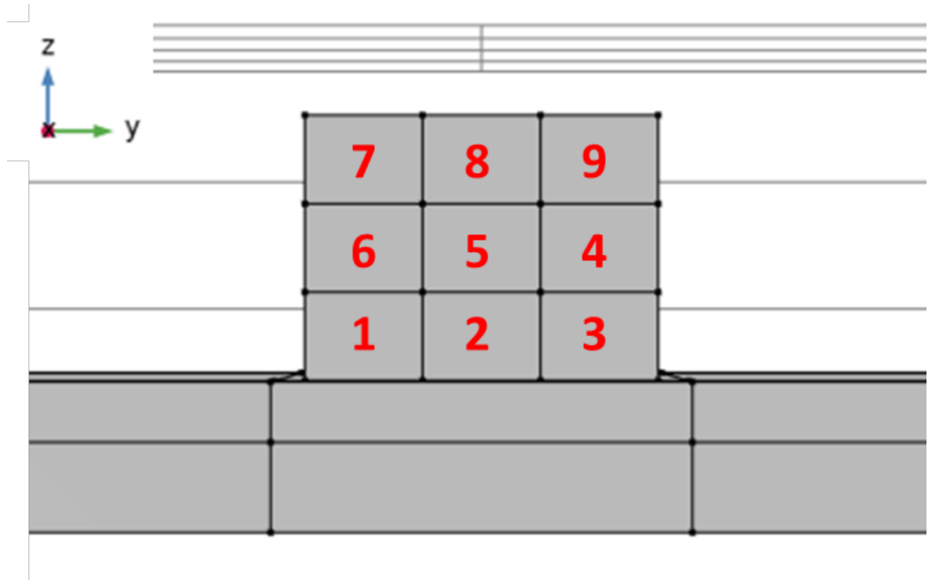

Figure 6.2: Order of the bead deposition for the FEA simulation.

6.2 Heat sources and material deposition

The primary heat source used in this simulation is the Goldak double-ellipsoid model [111]. The governing equations for the front and the rear halves of the heat source are represented by equations 6.2 and 6.3. The total input power in this simulation is 2700 W, which is the power provided by the welder. It is assumed that this power gets split into two parts: heat to melt the weld wire and heat to melt the substrate, thus creating the base of the weld pool. For initial calculation, it was assumed that the weld wire would fall off the weld wire when it reached 50 K above its melting temperature, which occurs at a temperature of 973 K. Equation 6.1 was used to determine the total energy required to get each bead to this temperature.

$$J_{input} = Lwh\rho(C_P\Delta T + H_f) \tag{6.1}$$

L, w, and h represent the length, width, and height of a bead, respectively. ρ and C_P are the density and specific heat capacity, while ΔH_f is the latent heat of fusion.

With the change in temperature of 678 K, the total input energy required to get the entire bead to a melted temperature of 923 K is 10,831 J. Given the time per bead deposition of 11.25 s, this means that 962 W from the total input power are used to get the bead to its droplet temperature and 1737 W are utilized to penetrate and melt the substrate material, which is the magnitude of Q in equations 6.2 and 6.3 of the Goldak heat source.

As previously stated, the Goldak heat transfer model is split up into two halves, one representing the front half of the ellipsoid and one representing the back half. In equations 6.2 and 6.3, f_f and f_r represent the fractional factors of the deposited heat. The constraint $f_f + f_r = 2$ must be maintained. The ellipsoid gets its shape from the constants a, b, c_r, and c_f. The constant a represents the maximum half-width of the heat source, 4mm, and the constant b represents the maximum penetration depth of the heat source, 4 mm. The length of the front section is represented by c_f, 4 mm, and the length of the rear section is represented by c_r, 16 mm. x_{focus}, y_{focus}, and z_{focus} represent the center of the double ellipsoid as it moves along the weld path. The weld path in this simulation is along the x direction. A image depicting the contour shape of the heat source is provided in figure 6.3.

$$f_1 = \frac{6sqrt3 f_f Q}{abc_f \pi \sqrt{\pi}} exp\left(\frac{(x - x_{focus})^2}{c_f^2} + \frac{(y - y_{focus})^2}{a^2} + \frac{(z - z_{focus})^2}{b^2}\right) \tag{6.2}$$

$$f_2 = \frac{6sqrt3 f_r Q}{abc_r \pi \sqrt{\pi}} exp\left(\frac{(x - x_{focus})^2}{c_r^2} + \frac{(y - y_{focus})^2}{a^2} + \frac{(z - z_{focus})^2}{b^2}\right) \tag{6.3}$$

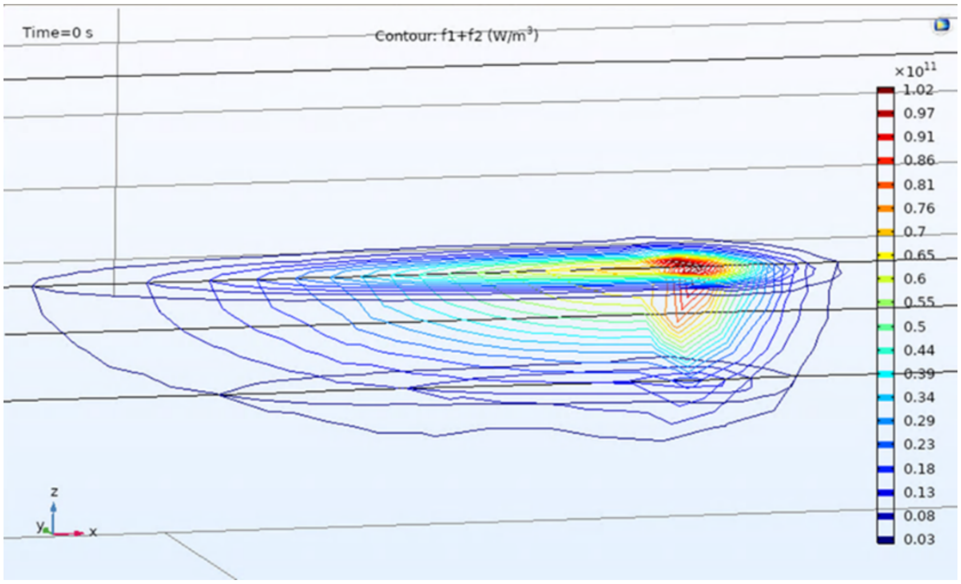

Figure 6.3: Goldak double-ellipsoid heat input contour plot showing how the heat distribution across the double-ellipsoid volume is being applied to the heated layers.

The velocity of the heat source, x_{focus}, for this simulation was 0.0133 m/s, or 800 mm/min. The model was set up so that different weld conditions could be simulated by having to change as few parameters as possible. The parameter *bead-time* is calculated by dividing the length of the bead by the velocity of the heat source. The *interpass-time*, which is the parameter that sets the time between bead deposition, can be set to the desired duration. Using these two variables the parameters for the welding start and end times of the beads are automatically calculated. The start and end times of the beads are used in the piecewise functions that computes x_{focus} and y_{focus}. While the y_{focus} piecewise function only switched between the constants that represent the three possible center y-locations of the beads (-8mm, 0 mm, 8 mm), the x_{focus} piecewise function was a simple linear position function of time. For example, the x_{focus} function for bead 2 was x_{focus2} = *-0.075[m] + vel*(t-t$_{2start}$)*.

The Goldak functions f_1 and f_2 were constrained both in time and space to lower computational costs. The values of f_1 and f_2 were only calculated for each bead during the actual deposition process. Additionally, the computational region for the heat input was also restricted to nodes with coordinates xyz that were within the double ellipsoid volume during the current time step. The Goldak heat input was also restricted to the substrate, or to the previously deposited bead onto which the new bead is being deposited. This was done to simulate only the heat input caused by the welding arc. The heating/melting of the bead material itself will be discussed later in this chapter. Lastly, in order to make the simulation results smoother, the heat input was ramped-up and ramped-down at the beginning and end of each bead. This was done with the addition of a smoothed step function with a transition zone of 100 ms.

As mentioned in the chapter introduction, depositing material in a welding simulation is not simply a matter of converting already present material in one form into another form (powder - liquid - solid). Welding involves the deposition of new material. What was not there before, must suddenly appear, and do so in a physical state representing reality. Several steps were taken to simulate this process as realistically as possible. A bead activation function, bead-function, was created to activate the elements as they would appear during deposition. This was done by activating the elements as a function of x_{focus} position, time, and domain. The first few terms of this function are shown in equation 6.4, with activation of the remaining 7 beads following the same logic.

$$f(bead) = (X_{focus} > X) * (dom == 13) + (X_{focus2} > X) * (dom == 16) * (t > t2_{start}) + \ldots \tag{6.4}$$

This function, along with the COMSOL constraint *solid.wasactive*, was used in the Solid Mechanics Element Activation setting. Only domains representing the individual beads were selected for this function. Elements that are not active are simulated as being air, with the proper properties assigned to them by the function. For example, to switch between the density of metal and the density of air during element activation, the material property activation function *if(solid.isactive,mat1.def.rho(T),mat2.def.rho-gas(T))* was used. This had to be done because all elements that constitute the final geometry of the part had to be included in the domain and mesh of the model at every time step. Thus, even though the elements are not active, heat transfer is being calculated for them. This made the process more challenging as will be shown in the following section on heat transfer. A big issue as well occurs when elements are activated and change their material properties, because this causes some instabilities in temperature results.

What remains to be modeled is the starting temperature of newly activated elements. It is not possible to set an initial temperature condition for newly activated elements at every time step. Therefore, the inactive elements had to already be at the desired temperature of 973 K. To accomplish this, an artificial heat source was created that heats up the inactive elements to the desired temperature right before they get activated. As such, it is applied only to inactive elements that have the property of air. This general heat source is applied through an if-statement in the COMSOL code represented in equation 6.5, where Q_{bead} is a general internal heat source to achieve the desired final temperature of the bead material for the moment it gets activated. As can be seen, the heat source only gets applied to the inactive elements 3 mm ahead of the x_{focus} from the Goldak heat source and keeps the temperature of these elements at around 1000 K. Figures 6.4 and 6.5 illustrate this process as a slice plot through the center of bead 1 during deposition.

$$if\left((X < (x_{focus} + 3) * (x_{focus} < X) * (T < 1100[K]) * (t < t_{end} - 0.2[s]), Q_{bead}, 0\right) \tag{6.5}$$

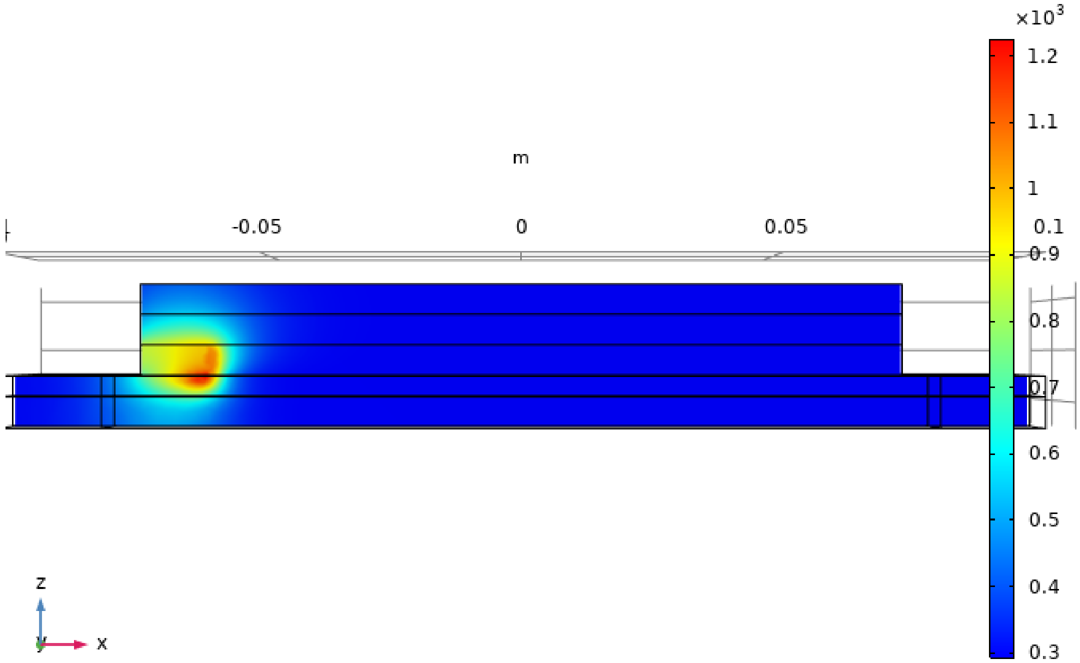

Figure 6.4: Temperature in degrees Kelvin at the center of bead 1 during deposition, whole model.

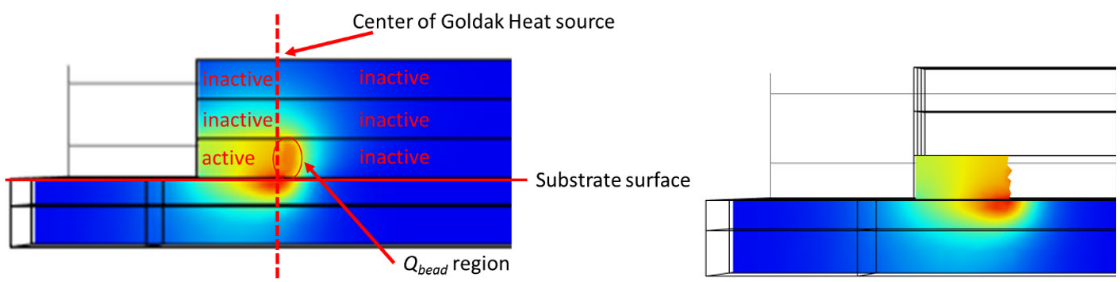

Figure 6.5: Zoomed in region showing bead heating, element activation status, and temperature profile (left) and temperature profile of only active beads (right).

As can be seen in these figures, the bead heat source does not get applied to any of the already active elements. Furthermore, due to the inactive elements having the properties of air, there is virtually no impact that this heat has on the temperature of the active material below it. In the initial 2D simulation tests to determine if this was a valid approach, this artificial heat source was applied to all inactive elements for the entire length of bead deposition. It was shown that there was virtually no heat transfer from the preheated inactive elements of air to the solid layers below.

This can be seen in figure 6.6, which shows the temperature distribution of the model towards the end of the bead deposition.

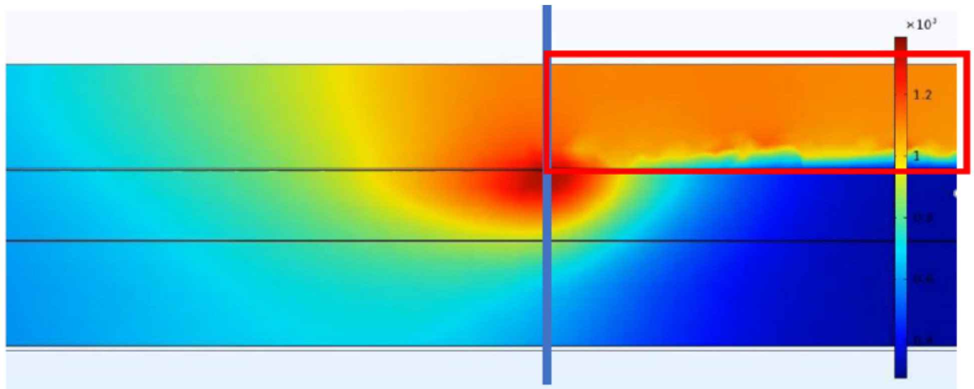

Figure 6.6: Example of applying the bead heating function to the entire bead for the duration of the simulation does not impact the active elements below due to the different thermal and mechanical properties that are assigned to active and inactive elements.

6.3 Heat transfer setup and mesh

As stated in the previous section, the instantaneous switch of the material properties when activating an element resulted in instabilities. However, it was determined that only the thermal conductivity, k, was causing this problem. The thermal conductivity for the solid is in the range of 150 to 180 $Wm^{-1}K^{-1}$, while the range for air is between 0.025 to 0.07 $Wm^{-1}K^{-1}$. Both are a function of temperature. The instabilities in the computation of the temperatures when using these low thermal conduction values for air can be seen in figure 6.7, which shows the result of temperature probes assigned to the bead and substrate domains. Probes for maximum and minimum node temperatures were assigned to each of the domains of these domains. It is worth noting that these spikes are not the general trend of the temperature distribution and represent only a single node within each of the domains. It was still decided to attempt to reduce these random spikes, especially for the probes measuring the minimum temperatures. The model that resulted in the result displayed in figure 6.7 also applied the Goldak heat source to both the beads and the substrate, resulting in equal temperatures for both sides of the interface, which is not as realistic as the bead heat input function proposed in this research.

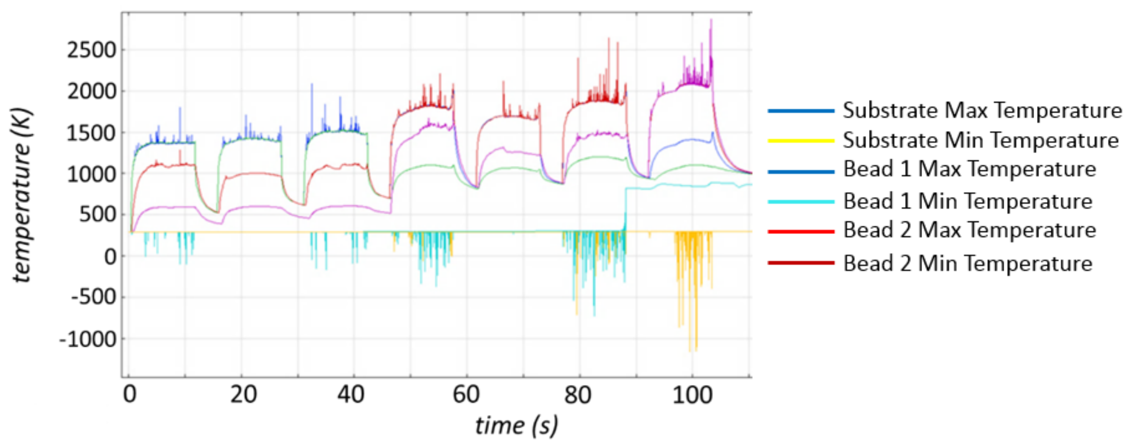

Figure 6.7: Instabilities in temperature calculations caused by large jumps in thermal conductivity when elements switch from inactive to active.

Minimum bead temperatures reached negative spikes as low as -1400 K, making this model unrealistic. This instability was removed by determining and setting a constant thermal conductivity variable for air of 0.5 to 2 Wm-1K-1. This ensured smooth computation results while still maintaining 2 orders of magnitude separation between the k for the solid and that of air. As will be shown later, this low thermal conductivity coefficient did not impact the conductive heat transfer through the inactive elements.

For the substrate, two boundary conditions were used. All surfaces that were exposed to the ambient air had a radiation heat transfer and a convection heat transfer boundary condition assigned to them, using a material emissivity of $\epsilon = 0.2$ for radiation, and a coefficient of h $= 80$ $Wm^{-2}K^{-1}$ for the forced convection. This convection coefficient was used to simulate the forced air being applied to the material during the weld interpass windows. The conditions for the individual beads was more complicated. It is not possible to apply boundary conditions in COMSOL to internal boundaries, so other steps had to be taken to simulate heat transfer to the environment as beads were deposited during the simulation. For this, each bead interface had to be assigned a unique heat transfer condition based on time and element activation of itself and of the surrounding beads. Figure 6.8 will be used as an example of how these boundary conditions were applied to the fourth bead.

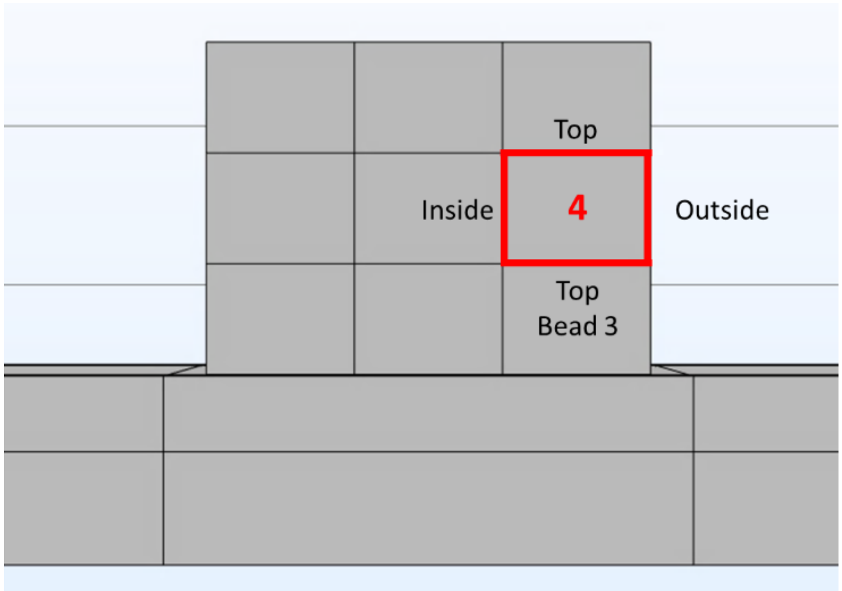

Figure 6.8: Example of how heat transfer boundary conditions are applied to the internal bead boundaries by using bead 4 as an example.

Activation of the outside boundary conditions for bead 4 only required that the elements themselves were active. Both surface-to-ambient (radiation) heat transfer and convective heat transfer were applied to that side of the bead using the requirement *solid.isactive* in COMSOL. The outside boundary will have these boundary conditions for the remainder of the simulation since the outside boundary will always remain exposed to ambient conditions. The inside and top boundaries needed additional requirements. For example, the inside boundary would also have surface-to-ambient and convection applied to it, but only if i.) the solid is active and ii.) the material deposited for bead 5 in the center does not exist yet. This was done by making the application of the boundary conditions dependent on the location of the heat sources for beads 4 and 5. An example of how this was applied to the radiation heat transfer equation for the inside boundary is *if((xfocus5>=X)*(X<=xfocus4)*(t<t5end),0.1,0)*. The same logic applies to the top boundary of bead 4, but that boundary is dependent

of the material deposition of bead 9 instead of bead 5. The boundary heat transfer for the bottom of bead 4 is included in the top boundary conditions for bead 3 and follows the same logic as that for the top of bead 4.

6.4 Heat transfer and deposition results

The method by which the simulation was set up captured the element deposition and heat transfer of the process successfully. To illustrate the results, the following figures show the heat transfer and element activation during the deposition of several beads.

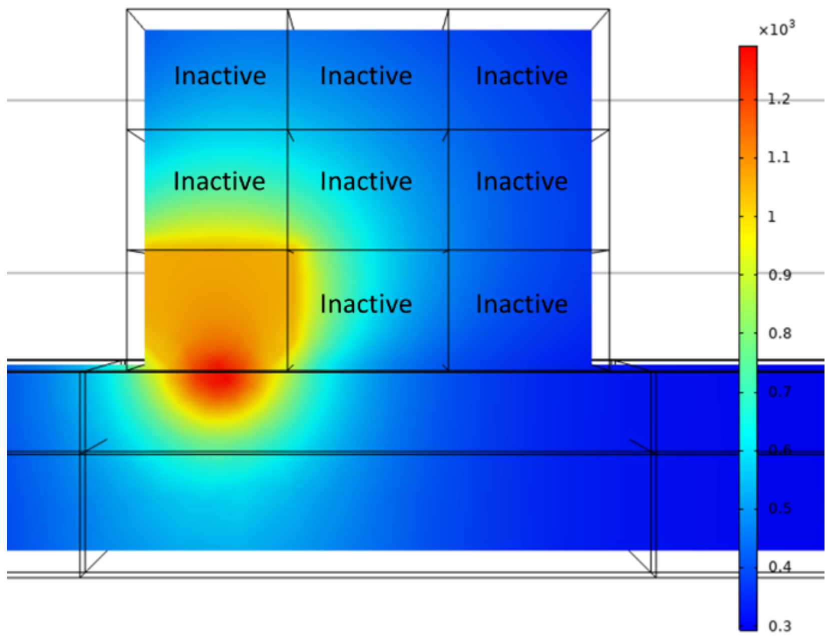

Figure 6.9: ZY-plane cross-section view of temperature distribution in bead 1 at the moment the elements in that plane are activated, showing the event temperature distribution and enabling the identification of the HAZ zone.

Figure 6.9 shows the temperature distribution halfway through the deposition of the first bead of the block. The shape of the fusion and heat affected zones can be clearly seen. The temperatures of the newly deposited bead are slightly below that of the heat input supplied by the Goldak heat source, as expected. The heat transfer downward into active elements of the substrate and to the ambient side can be seen as well. At this point in the simulation, only the substrate and portions of the first bead have active elements. The fact that the heat distribution appears symmetric with the COMSOL boundary conditions on the left and the custom inside and top bead boundary conditions to the right and top of the bead, indicates that the specially created conditions work as intended. There is of course a very small amount of conduction being calculated across the inactive beads since the thermal conductivity coefficient could not be set to zero, but the impact this has on the temperature profile was shown to be negligible. The temperatures during this operation show the expected values during deposition for this low heat input GMAW process. Figures 6.10 and 5.11 show the evolution of the material deposition and depict the state of the process when it has reached bead 7 of the top layer

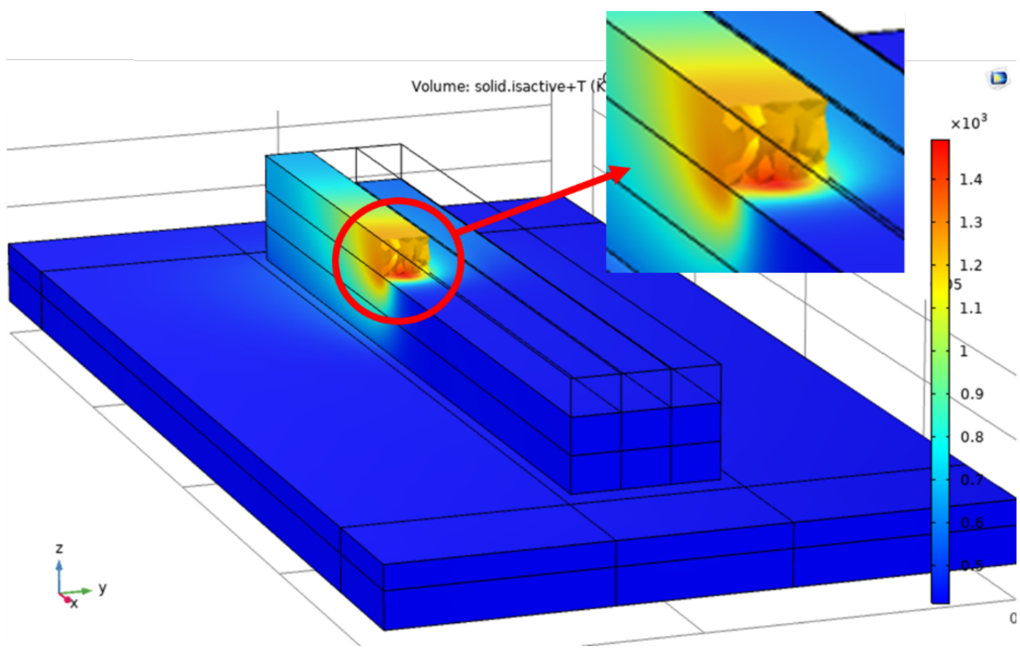

Figure 6.10: Bead 7 profile and temperature distribution during deposition showing how the model performs on top of newly activated elements.

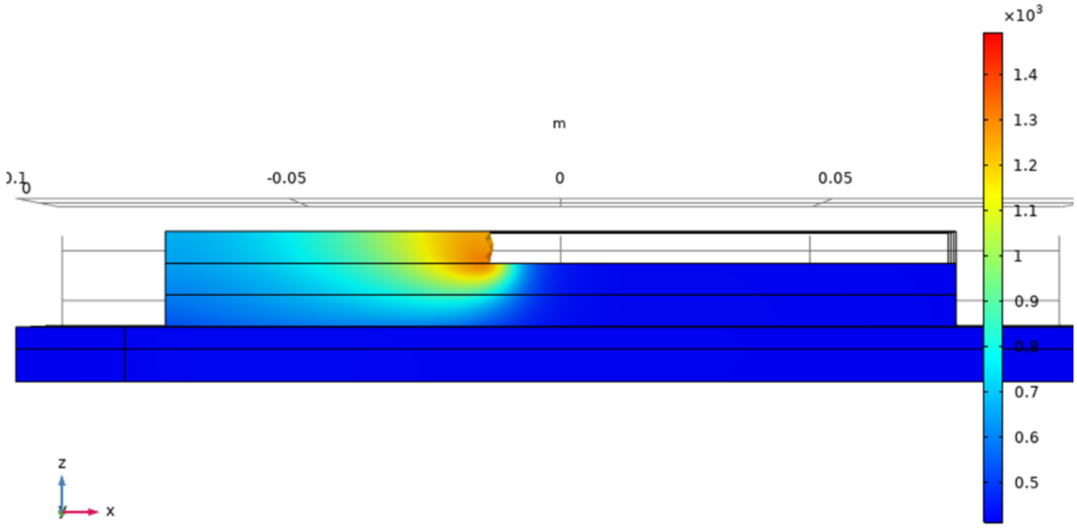

Figure 6.11: Side view of element activation and the temperature profile of bead 7, showing depth of heat source penetration and heat transfer behavior.

These two figures show how the deposition and temperature distribution continue to resemble the expected results for this process. It is important to note that the interpass time for this simulation was set to only 60 seconds to reduce the duration of the simulation. For real world applications, the interpass time must be at least two to four times that value to avoid overheating of the material. Sufficient time must be given so that the input heat has time to leave the material. If interpass times are too short, the material will melt too rapidly and, in the case of magnesium, potentially ignite. These results do present an additional benefit of this simulation. The simulation can now be used to determine the best interpass duration that would allow the material to return to the desired starting temperature for continued deposition. This would eliminate the need for excessive experimental testing and save time and money spent on material.

As stated above, the computational time for this model is considerable. The results shown for this model took 16 hours to obtain. There were 359,969 domain elements in the model, including 39,876 boundary elements. The model solved for 60,024 degrees of freedom, plus 48,236 degrees of freedom due to the prescribed internal heat transfer boundary conditions that are time and position dependent. Computations took place using a 3.3 GHz processor with 10 cores and 128 GB of available RAM. Figure 6.12 shows the mesh that was used in this simulation. A simplified version of this model that reduces the physical similarities between the model and the real world was also developed, requiring less than a quarter of the time and yielding similar results. The model showed similar results but does deviate from the true physics of heat transfer that are to be expected during the welding deposition. Due to the considerably lower computation time however, this model should still be considered once coupling with the structural mechanics module is tested. The model will be presented at the end of this chapter.

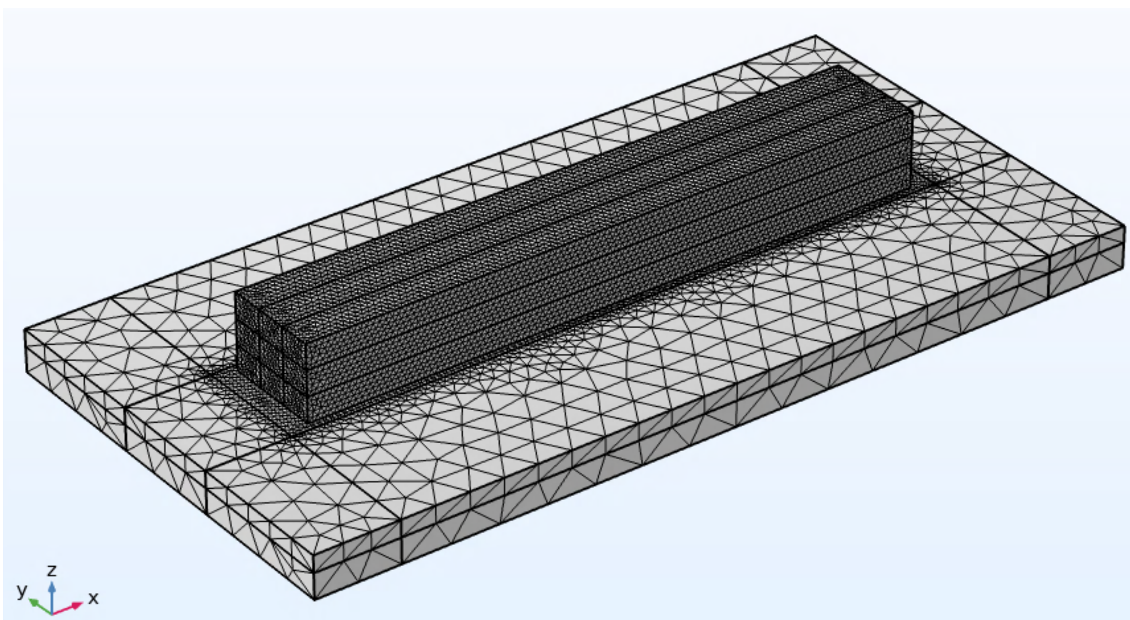

Figure 6.12: Mesh for the model showing a very fine mesh for the elements that are impacted directly by the heat source functions and a coarser mesh for elements along the substrate.

The Goldak heat source has a very small volume and it was important to capture as much of the heat source as possible. This meant that the mesh for the beads and for the part of the substrate that deposition was on had to be very small. A maximum element size of 1.5 mm was used for the Goldak input domains. The remaining substrate could be meshed with significantly larger elements.

As in the previous simulation, probes were used again to measure the maximum and minimum node temperatures in all the domains of the model. Figure 6.13 shows these results for the simulations. In this plot, bead 5 was omitted to show the rate of the temperature decrease more clearly during longer interpass windows. As can be seen, even with a 130 second cool down window, the maximum temperature in the beads is still 400 K and even the minimum temperatures are still above 300 K. It takes over four minutes until the bead temperatures are back to the ambient temperature of 293.15 K. This was also the case during the experimental part of the project, where cool down took several minutes depending on interpass duration between previously deposited beads. Bead 4 in the simulation showed a particularly large jump in maximum temperature due to it being deposited directly on top of the previous bead, which has not had enough time to cool down.

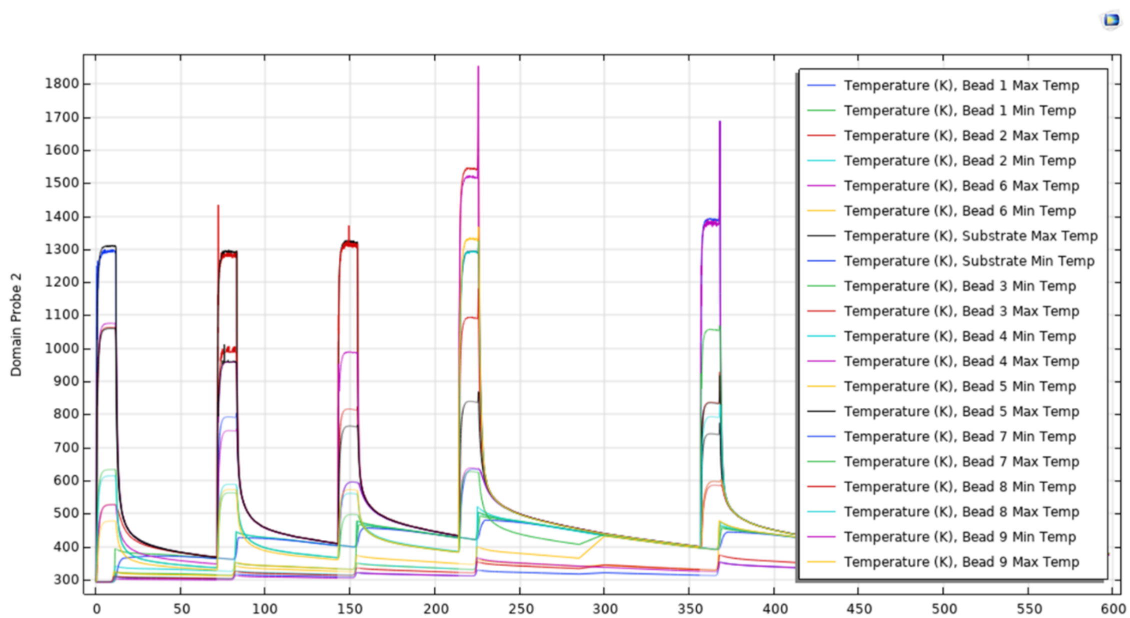

Figure 6.13: Maximum and minimum temperature probe results for all model elements for each time step of the simulation.

This setup did remove the big drops in minimum temperature of the previous simulation, which dropped as low as -1400 K. However, there are still spikes at the end of each bead deposition phase. This is because as the heat source reaches the end of the bead, the boundary condition there does not allow the heat to be removed at a rate fast enough, causing a sudden buildup of energy in the inactive elements. This is depicted in figure 6.13 where it can be clearly seen how the maximum temperatures suddenly jumps up t the very end of the bead and sometimes at the beginning of the beads. This could be removed by adding a time dependent heat flux to the back boundary of the welded block that allows the excess heat to be removed more rapidly as the Goldak heat source approaches the end of the bead. One could also edit the ramp down rate of the Goldak heat source and/or the bead heating source. However, since only a few inactive elements were affected by this phenomenon, there has been no attempt made as of now to try and remove these spikes. Only plotting active elements shows that these spikes are not part of the solid material that is of interest in this simulation, which will be seen in the next part of this section. The future work of using the results of this model as input parameters to a structural mechanics analysis will be discussed in chapter 6.

This model can be significantly simplified to greatly reduce computational time, but this comes at the expense of realism. Instead of having all the convective and radiation heat transfer taking place at the bead boundaries structured as functions of time, deposition states, and torch position, they can be prescribed as binary on/off conditions that only depend on the bead being fully deposited and the state of deposition of the neighboring beads. Using figure 6.8 as an example again, all five boundaries of bead 4 would have their convective and radiative heat transfer functions activated all at the same time when all of bead 4 has been deposited, with no heat transfer taking place across those boundaries during bead deposition. The inside boundary would have heat transfer take place until all of bead 5 has deposited, and the top boundary would stay active until all of bead 9 has been deposited. Additionally, the bead heat source can also be greatly reduced, relying on the front part of the Goldak heat source to bring the beads to the correct temperature before they are activated. By making these two modification, the simulation time drops from over 16 hours to just over 3 hours, but it comes at a cost.

Doing so, will not impact the realistic results of bead activation temperature for the first bead on every layer, but it will impact the rest of the beads as the conduction heat transfer towards the side with active solid elements is far greater as that towards the inactive elements of air. This can be seen in figure 6.14, where the left side of the bead has cooled substantially compared to the right side. Figure 6.15 gives a look at how heat transfer continues after the heat source has passed, but the right side has yet to be activated.

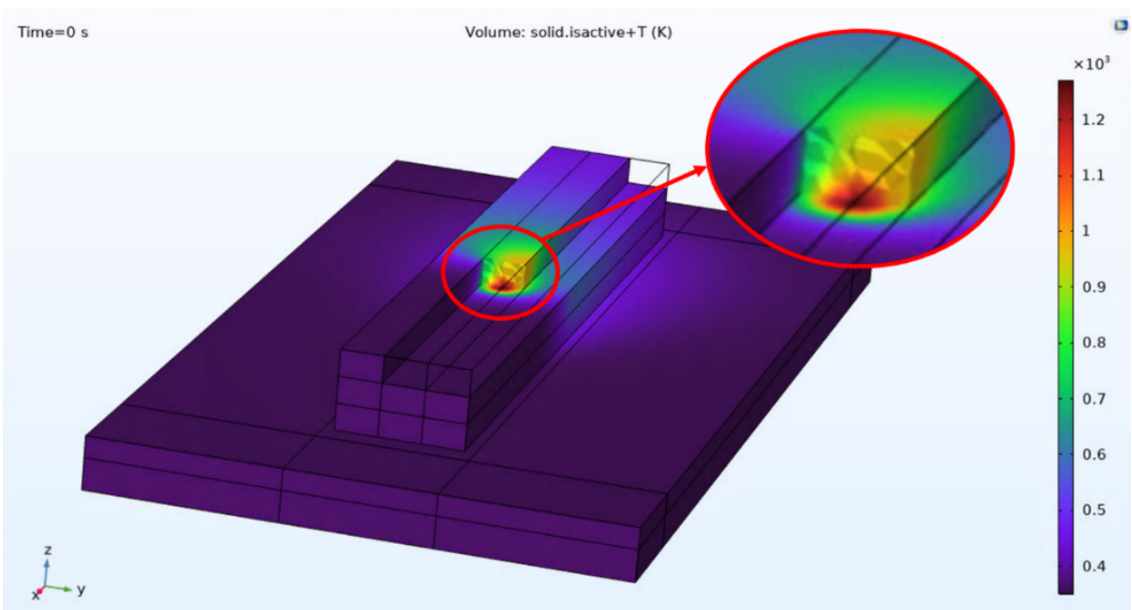

Figure 6.14: Deposition and heat transfer during bead deposition without active convection and radiation boundary conditions while the bead is being deposited, showing an uneven temperature distribution across the face of the newly activated bead.

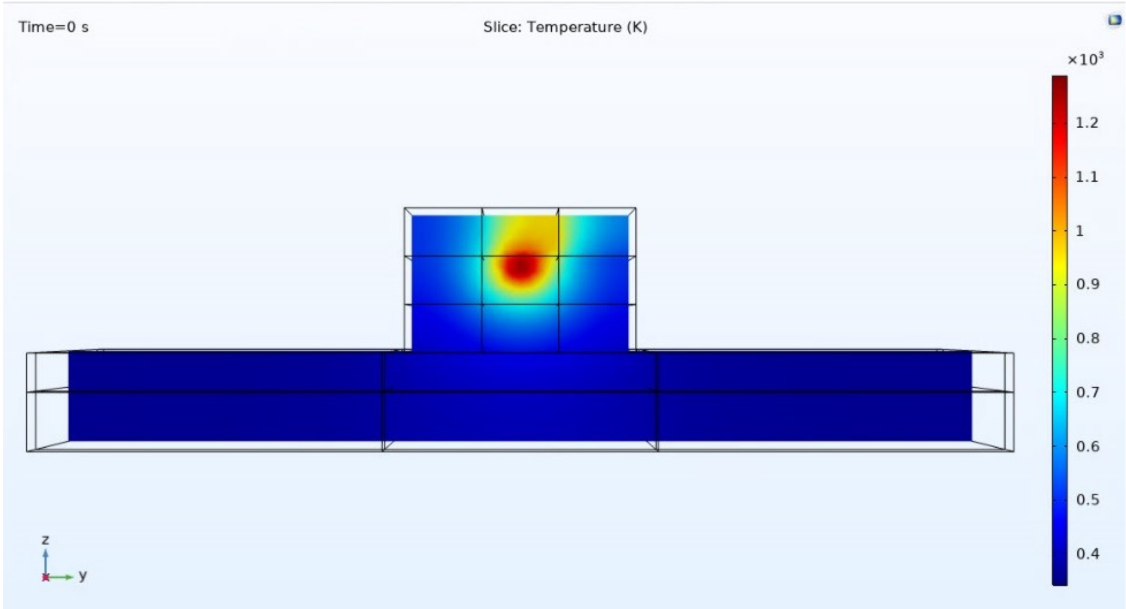

Figure 6.15: Heat transfer after the heat source has passed with inactive convective and radiation heat transfer boundaries, showing how with this modified model the bead cooling is much fasted on the side where conduction to the neighboring bead can take place while the other side is effectively treated as insulated.

The heat transfer pattern as observed in figure 6.15 is still realistic of the physical process being modeled. Rapid heat removal due to conduction towards the left bead cools down the newly deposited bead at a fast pace while the right side of the bead, with convection and radiation removed, can only transfer heat via conduction to the elements possessing the properties of air. In reality, this heat transfer distribution across the newly activated bead would have the same pattern, but with more heat being removed on the right edge of the bead. Since this boundary is only inactive for 11 seconds, the slight impact this makes on final computation results may be worth the reduction in computational costs. Removing or lowering the impact the bead heat source has on the model, however, has a greater impact on the reality of the welding process. The beads that fall onto the deposition area should have the same temperature distribution across their area. Without applying this heat source, there is a large temperature loss due to conduction that takes place towards the left side before the bead is activated. This results in an activation temperature of around 800

K on the left boundary and 950 K on the right boundary.

Figure 6.16 shows the impact that these changes have on the maximum and minimum temperatures seen by the active elements in this model. For this simulation, an interpass time of 120 seconds was selected. The model captures the expected increase in temperatures for the fourth and seventh bead due to the reduction in directions that heat transfer can take place since these beads are the first beads on layers 2 and 3, respectively. Overall maximum and minimum temperatures remain similar to the first model presented. The jumps in temperature are not present here, but this is because this figure, unlike figure 6.13, plots only the temperatures of the activated elements that are of interest.

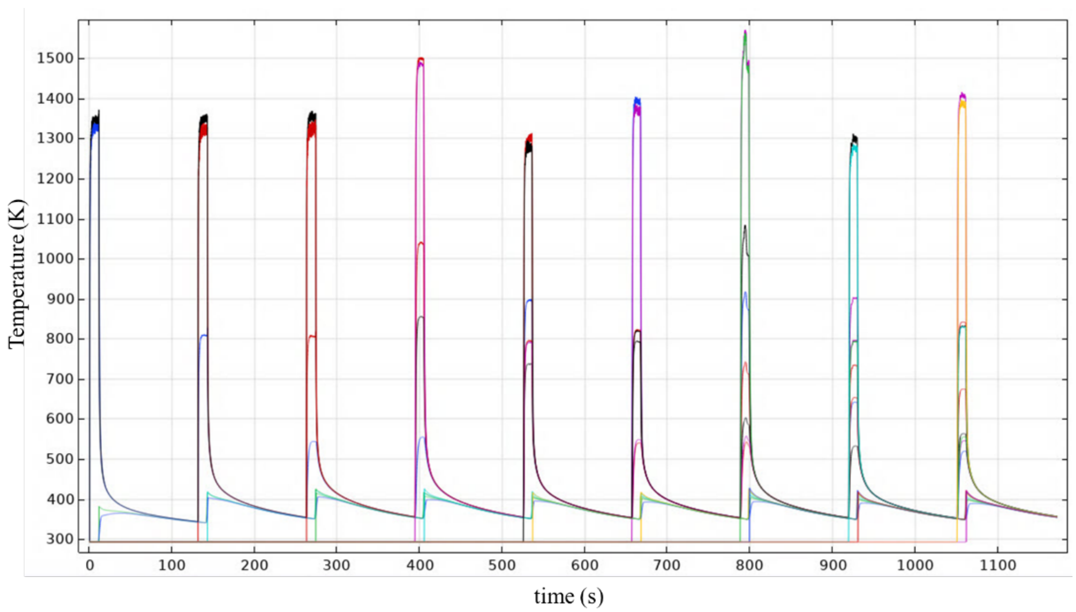

Figure 6.16: Bead temperatures for only active elements during deposition process for the simplified model showing a similar overall heat transfer behavior and numerically stable results.

CHAPTER 7: CONCLUSION AND FUTURE WORK

7.1 Conclusion

Additively manufacturing components out of magnesium alloys by utilizing generic GMAW has been shown as a viable method, even though having been dismissed as such in the past. The method of course does come with several challenges to overcome, as this research has shown, but it nevertheless is possible to produce parts with consistent shapes and material properties.

This process is especially useful for prints that require a wall thickness slightly less than that of a weld bead. Layer-by-layer deposition was shown to be consistent for parts up to 80 mm in height. Taller prints would easily be possible but could not be completed as the prototype CNC that was built and used for this body of work had limitations in the vertical build direction. Tensile tests performed on single wall structures showed the consistency across different parts in elastic response to load and yield strength. The isotropic quality of the printed magnesium parts was also confirmed by the performance of tensile tests where the applied load was both in-line with, and normal-to, the direction of the bead deposition. The impact that other input parameters have on the material properties has also been confirmed. Changes in torch travel speed at same power-inputs resulted in changes to the YS of the material, with increases of TTS weakening the material. While the welding AM process in general does considerably reduce the YS of the manufactured part, it needs to be noted that this research did not apply any post-weld or in-process treatments to the printed parts, which would significantly improve the material properties. In-process cold rolling or post weld heat treatments could be easily applied to make such improvements.

Closed-form parts were also printed in the form of hollow cylinders. The problem of connecting the beads at their start and end point was eventually reduced by alternating the start and end positions of each consecutive layer and adding a one second dwell at the end of the bead to account for layer closure. Applying this process enabled the builds of magnesium cylinders with heights of up to 80 mm. This was also accomplished at different heat-input energy rates, producing both ultra-thin walled cylinders with a wall thickness of 1.5 mm, and thicker walled cylinders with up to 5 mm wall thickness.

Finally, multi-row/multi-layer blocks of magnesium were printed while utilizing numerous input parameters and stagger/layer patterns. Blocks were successfully printed, but with more porosity than their single-wall counterparts. This was primarily due to the side-flow problem that is caused due to the low viscosity of melted magnesium. The material flows out of the weld pool at a much faster pace than other weldable metals, especially during weld overlapping. Even with this problem, large blocks consisting of well over 100 beads were printed, machined, and tested. Material properties for the elastic region and yield strength were once again consistent and independent on print direction, but the presence of larger voids resulted in much earlier fracture than with the single-walled test specimens. This, however, can be fixed, and will be addressed in the following section.

What makes this process so attractive is its speed. Many other WAAM methods can claim some of the same benefits as unaltered GMAW, such as the virtually limitless print size of parts. The deposition rate in GMAW, however, is faster than most other such AM methods. In this experiment, parts like the hollow cylinder examined in the XCT analysis were printed at a WFS of close to 17 m/min, which is well above that of typical WAAM processes. That means the process can deposit almost 1 kilometer of wire per hour, and with a wire diameter of 1.2 mm this results in an hourly deposition of almost 2 kg. That is the equivalent to depositing 2.93 kg/hr. of aluminum or 8.36

kg/hr. of steel, when examining equal volume.

The primary hindrance in perfecting this method lies with limited availability of equipment and welding wire. Commercial welders are optimized primarily for steel, aluminum and titanium. Due to the many challenges that come hand-in-hand with working with magnesium, the material has yet to find a spot in the wire-materials library on available inverters, making it near to impossible to determine the proper heat-input rate for a successful bead deposition. Therefore, most of the welding that is being done with magnesium is done by TIG welding, where the heat input on a welder will not change based on the wire material because the wire itself is not the electrode for the process. TIG welding, however, is not nearly as fast as GMAW, which is why it is not suitable for AM purposes, at least not on a mass production scale.

If one succeeds in finding suitable welding parameters for magnesium with a GMAW machine, then the next challenge will be the quality of the available wire. Welding is not the only manufacturing process that struggles with utilizing magnesium. The difficulties in working with this material also show themselves in the drawing process which is used to create the MIG wire. Being riddled with defects, this magnesium wire can abruptly halt the deposition process during AM, leading to unfixable flaws in the part, requiring it to be scrapped. This is especially costly with a material that is as expensive as magnesium. However, as the demand for magnesium continues to rapidly increase across the globe, this cost and availability issue will balance itself. As demand increases, supply will increase as well, and this will reduce the costs and bring with it an increase in quality.

7.2 Future work

7.2.1 Magnesium dedicated GMAW machine and MIG wire drawing

Before any additional research should be done, a magnesium dedicated inverter should be designed and built, or a currently existing welder should be modified to allow for optimized wire material settings. As stated previously, the Welbee was purchased for this exact purpose but the author was not given access to this option. With such a machine, the weld parameters that were established in this research could be used as a starting point for tuning and improving the deposition process. This would result in a reduction of spatter and side-flow due to better temperature control.

Additionally, until the availability of quality magnesium wire increases as well, it is of great benefit to attempt to produce test wire in-house. Many researchers have already started to do so in order to control the quality of the material. If this process is not possible, a wire-cleaning machine should be developed. This would not only benefit magnesium applications, but any weld wire material that has a tendency to oxidize and/or rust. The design and build of such a machine will be proposed to the Senior Design committee at UNC-Charlotte for design to start in the spring semester of 2024. An in-process wire defect metrology method will also be integrated with this machine. This can be accomplished either via visual inspection or by measuring wire diameter or roughness.

7.2.2 Five-axis CNC

Some of the issues with porosity in this research did not stem from incorrect welding parameters, but rather from problems with the overlapping of the beads. The heat must be carefully controlled with GMAW of magnesium as to not cause evaporation of the material. Since the temperature must be kept at a lower magnitude, many beads take on a caterpillar like shape, as seen in Chapter 3, figure 3.15. This may not be a big problem for single wall structures, but when printing parts that have wall thicknesses that are multiple times the thickness of a single weld bead, the beads need to be overlapped. With these caterpillar-like bead shapes, long voids along the weld direction could start to form as there is no fusion taking place. This was also shown in Chapter 3, figure 3.15. With the addition of another axis, the build plate and substrate could be tilted, allowing for additional rows of material to be deposited in the bead gaps between the bead and substrate. This process was used in this experiment while determining welding parameters by hand and showed great promise. Given the open nature of the current GMAW-CNC used, it would be possible to raise the Z-axis and add an additional tilting axis onto which to mount the substrate. Changes in expected heat transfer for interpass cooling rates would have to be considered.

An in-process part cleaning method would need to be integrated with the CNC as well. Due to the high vapor deposition seen with magnesium and even aluminum welding, the part needs to be cleaned after every weld pass, which is much too labor intensive. Integrating another axis dedicated to brushing the part clean or using a simple robotic arm mounted to the side of the machine would greatly reduce the labor involved and make the process much faster.

7.2.3 Interpass cooling methods

Different interpass cooling methods need to be investigated to reduce print time and research their impact on microstructure and material properties. Forced air convection via a simple fan was the only external cooling method applied in this research. The result was unnecessary downtime between bead deposition to allow the material to get back to ambient temperature. This was especially important with magnesium due to dangers of low viscosity when melted, as well as the possibility of material ignition leading to continuously burning fires. Increasing the cooling rate and determining its impact on part quality would yield very meaningful data.

7.2.4 Thermo-mechanical multiphysics analysis

The results from the validated heat transfer and material deposition model, coupled with COMSOLs Thermal Expansion module, need to used as input parameters to a mechanical analysis. The ultimate goal in this sequential model is to determine not only part distortion induced by the WAAM process but also to back out residual stresses that remain in the part. Figure 7.1 shows the flow chart for this process. Modelling phase transformations in multi-pass welds is much more challenging than single pass-welds because of repeated phase transformations as new weld passes affect the HAZ from the previous weld passes. Additionally, the simulation of the clamping adds additional challenges as the part distortion will not occur until those boundary conditions are released, which will require an additional spring-back simulation to determine the actual final part distortion.

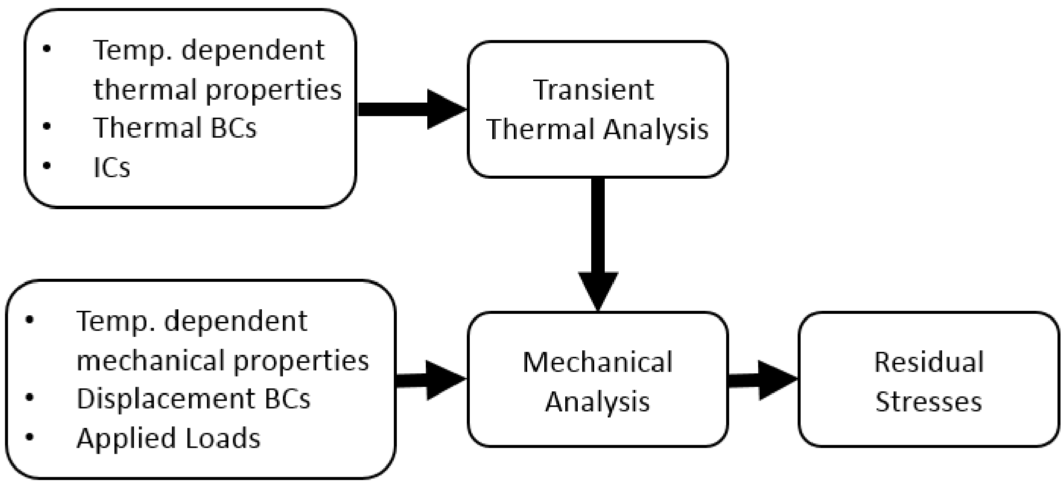

Figure 7.1: Thermo-mechanical model flow chart.

REFERENCES

[1] J. Milewski, "Additive manufacturing of metals: From fundamental technology to rocket nozzles, medical implants, and custom jewelry," *Additive Manufacturing of Metals*, 2017.

[2] S. W. Williams, F. Martina, A. C. Addison, J. Ding, G. Pardal, and P. Colegrove, "Wire + arc additive manufacturing," *Materials Science and Technology*, vol. 32, pp. 641–647, 2016.

[3] K. Treutler and V. Wesling, "The current state of research of wire arc additive manufacturing (waam): A review," *Applied Sciences*, vol. 11, 2021.

[4] D. Liu, B.-Y. Lee, A. V. Babkin, and Y. Chang, "Research progress of arc additive manufacture technology," *Materials (Basel)*, vol. 14, pp. 1415–1415, 2021.

[5] Q. Han, J. Gao, C. Han, G. Zhang, and Y. Li, "Experimental investigation on improving the deposition rate of gas metal arc-based additive manufacturing by auxiliary wire feeding method.," *Welding in the World*, vol. 65, pp. 35–45, 2020.

[6] B. Gomes, P. Morais, V. Ferreira, M. Pinto, and L. Almeida, "Wire-arc additive manufacturing of al-mg alloy using cmt and pmc technologies," in *MATEC Web of Conferences*, 2018.

[7] Z. Hu, X. Qin, Y. Li, J. Yuan, and Q. Wu, "Multi-bead overlapping model with varying cross-section profile for robotic gmaw-based additive manufacturing.," *Journal of Intelligent Manufacturing*, vol. 31, pp. 1133–1147, 2019.

[8] Z. Hu, X. Qin, Y. Li, and M. Ni, "Welding parameters prediction for arbitrary layer height in robotic wire and arc additive manufacturing.," *Journal of Mechanical Science and Technology*, vol. 34, pp. 1683–1695, 2020.

[9] B. A. Szost, S. Terzi, F. Martina, D. Boisselier, A. Prytuliak, T. Pirling, M. Hofmann, and D. J. Jarvis, "A comparative study of additive manufacturing techniques: Residual stress and microstructural analysis of clad and waam printed tiâ6alâ4v components.," *Materials Design*, vol. 89, pp. 559–567, 2016.

[10] F. Martina, M. Roy, P. Colegrove, and S. W. Williams, "Residual stress reduction in high pressure interpass rolled wire+arc additive manufacturing ti-6al-4v components," *Repositories.lib.utexas.edu*, 2014.

[11] B. Cong, J. Ding, and S. Williams, "Effect of arc mode in cold metal transfer process on porosity of additively manufactured al-6.3%cu alloy.," *The International Journal of Advanced Manufacturing Technology*, vol. 76, pp. 1593–1606, 2014.

[12] J. Xiong, Y. Lei, H. Chen, and G. Zhang, "Fabrication of inclined thin-walled parts in multi-layer single-pass gmaw-based additive manufacturing with flat position deposition.," *Journal of Materials Processing Technology*, vol. 240, pp. 397–403, 2017.

[13] B. Xu, X. Tan, X. Gu, D. Ding, Y. Deng, Z. Chen, and J. Xu, "Shape-driven control of layer height in robotic wire and arc additive manufacturing.," *Rapid Prototyping Journal*, vol. 25, pp. 1637–1646, 2019.

[14] J. Plangger, P. SchabhÃŒttl, T. Vuherer, and N. Enzinger, "Cmt additive manufacturing of a high strength steel alloy for application in crane construction," *Metals*, vol. 9, 2019.

[15] E. J. Soderstrom and P. Mendez, "Humping mechanisms present in high speed welding.," *Science and Technology of Welding and Joining*, vol. 11, pp. 572–579, 2006.

[16] A. Adebayo, J. Mehnen, and X. Tonnellier, "Limiting travel speed in additive layer manufacturing.," in *Conference: 9th International Conference on Trends in Welding Research American Society for Metals*, 2012.

[17] B. Wu, D. Ding, Z. Pan, D. Cuiuri, H. Li, J. Han, and Z. Fei, "Effects of heat accumulation on the arc characteristics and metal transfer behavior in wire arc additive manufacturing of ti6al4v.," *Journal of Materials Processing Technology*, vol. 250, pp. 304–312, 2017.

[18] Y. Bandari, T. Charrett, F. Michel, J. Ding, S. Williams, and R. Tatam, "Compensation strategies for robotic motion errors for additive manufacturing (am)," in *Proceedings of the 27th annual solid freeform fabrication symposium*, 2016.

[19] T. DebRoy, H. L. Wei, J. S. Zuback, T. Mukherjee, J. W. Elmer, J. O. Milewski, A. M. Beese, A. Wilson-Heid, A. De, and W. Zhang, "Additive manufacturing of metallic components â process, structure and properties," *Progress in Materials Science*, vol. 92, pp. 112–224, 2018.

[20] Y. M. Zhang, Y.-P. Yang, W. Zhang, and S. Na, "Advanced welding manufacturing: A brief analysis and review of challenges and solutions," *Journal of Manufacturing Science and Engineering*, vol. 142, 2020.

[21] G. Casalino, "Advances in welding metal alloys, dissimilar metals and additively manufactured parts," *Metals*, vol. 7, 2017.

[22] Z. Zeng, M. Salehi, A. Kopp, S. Xu, M. Esmaily, and N. Birbilis, "Recent progress and perspectives in additive manufacturing of magnesium alloys," *Journal of Magnesium and Alloys*, vol. 10, pp. 1511–1541, 2022.

[23] M. K. Kulekci, "Magnesium and its alloys applications in automotive industry," *The International Journal of Advanced Manufacturing Technology*, vol. 39, pp. 851–865, 2007.

[24] a. L. Bruce Gwynne, “Magnesium alloys in aerospace applications, past concerns, current solutions,” in *Triennial International Aircraft Fire Cabin Safety Research Conference*, 2007.

[25] K. Wei, Z. Wang, and X. Zeng, “Element loss of az91d magnesium alloy during selective laser melting process,” vol. 52, pp. 184–190, 2016.

[26] Y. Guo, G. Quan, M. Celikin, L. Ren, Y. Zhan, L. Fan, and H. Pan, “Effect of heat treatment on the microstructure and mechanical properties of az80m magnesium alloy fabricated by wire arc additive manufacturing.,” *Journal of Magnesium and Alloys*, vol. 10, pp. 1930–1940, 2022.

[27] Y. Guo, G. Quan, Y. Jiang, L. Ren, L. Fan, and H. Pan, “Formability, microstructure evolution and mechanical properties of wire arc additively manufactured az80m magnesium alloy using gas tungsten arc welding,” *Journal of Magnesium and Alloys*, vol. 9, pp. 192–201, 2017.

[28] T. Klein, A. Arnoldt, M. Schnall, and S. Gneiger, “Microstructure formation and mechanical properties of a wire-arc additive manufactured magnesium alloy,” *The Journal of The Minerals, Metals Materials Society*, vol. 73, pp. 1126–1134, 2021.

[29] X. Fang, J. Yang, S. Wang, C. Wang, K. Huang, H. Li, and B. Lu, “Additive manufacturing of high performance az31 magnesium alloy with full equiaxed grains: Microstructure, mechanical property, and electromechanical corrosion performance.,” *Journal of Materials Processing Technology*, vol. 300, 2022.

[30] J.-W. Li, Y. Qiu, J. Yang, Y. Sheng, Y. Yi, X. Zeng, L. Chen, F. Yin, S. Jiangzhou, T. Zhang, X. Tong, and B. Guo, “Effect of grain refinement induced by wire and arc additive manufacture (waam) on the corrosion behaviors of az31 magnesium alloy in nacl solution.,” *Journal of Magnesium and Alloys*, vol. 11, pp. 217–229, 2023.

[31] H. Takagi, H. Sasahara, T. Abe, H. Sannomiya, S. Nishiyama, S. Ohta, and K. Nakamura, “Material-property evaluation of magnesium alloys fabricated using wire-and-arc-based additive manufacturing.,” *Additive Manufacturing*, vol. 24, pp. 498–507, 2018.

[32] X. Yang, J. Liu, Z. Wang, X. Lin, F. Liu, W. Huang, and E. Liang, “Microstructure and mechanical properties of wire and arc additive manufactured az31 magnesium alloy using cold metal transfer process.,” *Materials Science and Engineering: A*, vol. 774, 2020.

[33] J. Guo, Y. Zhou, C. Liu, Q. Wu, X. Chen, and J. Lu, “Wire arc additive manufacturing of az31 magnesium alloy: Grain refinement by adjusting pulse frequency,” *Materials*, vol. 9, p. 823, 2016.

[34] X. Meng, G. Qin, and Z. Zou, “Investigation of humping defect in high speed gas tungsten arc welding by numerical modelling.,” *Materials Design*, vol. 94, pp. 69–78, 2016.

[35] T. C. Nguyen, D. C. Weckman, D. A. Johnson, and H. W. Kerr, “The humping phenomenon during high speed gas metal arc welding.,” *Science and Technology of Welding and Joining*, vol. 10, pp. 447–459, 2005.

[36] X. Shen, G. Ma, and P. Chen, “Effect of welding process parameters on hybrid gmaw-gtaw welding process of az31b magnesium alloy.,” *The International Journal of Advanced Manufacturing Technology*, vol. 94, pp. 2811–2819, 2017.

[37] H. Dong, C. Liao, and L. Yang, “Microstructure and mechanical properties of az31b magnesium alloy gas metal arc weld,” *Transactions of Nonferrous Metals Society of China*, vol. 22, pp. 1336–1341, 2012.

[38] D. Wagner and Y. K. Yang, “Spatter and porosity in gas-metal arc welding of magnesium alloys : Mechanisms and elimination.,” *Semantic Scholar*, 2013.

[39] T. Ying, Z. Zhao, P. Yan, J. Wang, and X. Zeng, “Effect of fabrication parameters on the microstructure and mechanical properties of wire arc additive manufactured az61 alloy.,” *Materials Letters*, vol. 307, 2022.

[40] A. Razal Rose, K. Manisekar, V. Balasubramanian, and S. Rajakumar, “Prediction and optimization of pulsed current tungsten inert gas welding parameters to attain maximum tensile strength in az61a magnesium alloy,” *Materials Design*, vol. 37, pp. 334–348, 2012.

[41] A. Becker, “Metals material modelling: Welding simulation and residual stresses,” in *University of Nottingham, UK, year=2021*.

[42] Y. Ogino, S. Asai, and Y. Hirata, “Numerical simulation of gmaw process from the heat source to the weld pool formation,” *Materials Science Forum*, vol. 941, pp. 674–678, 2018.

[43] Y. Ogino, Y. Hirata, and A. B. Murphy, “Numerical simulation of gmaw process using ar and an arâco2 gas mixture,” *Welding in the World*, vol. 60, pp. 345–353, 2016.

[44] J. Goldak, A. Chakravarti, and M. Bibby, “A finite element model for welding heat sources,” *Metallurgical Transactions B*, vol. 15, pp. 299–305, 1984.

[45] M. Grujicic, S. Ramaswami, J. S. Snipes, C.-F. . Yen, B. A. Cheeseman, and J. S. Montgomery, “Multiphysics modeling and simulations of mil a46100 armor-grade martensitic steel gas metal arc welding process,” *Journal of Materials Engineering and Performance*, vol. 22, pp. 2950–2969, 2013.

[46] T. Zacharia, A. H. Eraslan, D. K. Aidun, and S. A. David, "Three-dimensional transient model for arc welding process," *Metallurgical Transactions B*, vol. 20, pp. 645–659, 1989.

[47] F. Montevecchi, G. Venturini, A. Scippa, and G. Campatelli, "Finite element modelling of wire-arc-additive-manufacturing process," in *Procedia CIRP*, 2016.

[48] J. Martin, B. Yahata, J. Hundley, J. Mayer, T. Schaedler, and T. Pollock, "3d printing of high-strength aluminium alloys," *Nature*, vol. 549, no. 7672, pp. 365–369, 2017.

[49] G. C. Anzalone, C. Zhang, B. Wijnen, P. G. Sanders, and J. M. Pearce, "A low-cost open-source metal 3-d printer," *IEEE Access*, vol. 1, pp. 803–810, 2013.

[50] S. Dahat, K. Hurtig, J. Andersson, and A. Scotti, "A methodology to parameterize wire + arc additive manufacturing: A case study for wall quality analysis," *Journal of Manufacturing and Materials Processing*, vol. 4.14, 2020.

[51] K. S. Derekar, "A review of wire arc additive manufacturing and advances in wire arc additive manufacturing of aluminium," *Materials Science and Technology*, vol. 34, pp. 895–916, 2018.

[52] a. K. M. Mohebbi, M. S. and V. Ploshikhin, "A thermo-capillary-gravity model for geometrical analysis of single-bead wire and arc additive manufacturing (waam)," *The International Journal of Advanced Manufacturing Technology*, vol. 109, pp. 877–891, 2020.

[53] Q. Zhan, Y. Liang, J. Ding, and S. Williams, "A wire deflection detection method based on image processing in wire + arc additive manufacturing," *The International Journal of Advanced Manufacturing Technology*, vol. 89, pp. 755–763, 2016.

[54] B. Silwal, A. Nycz, C. Masuo, M. W. Noakes, D. C. Marsh, and D. Vaughan, "An experimental investigation of the effectiveness of ar-co2 shielding gas mixture for the wire arc additive process," *The International Journal of Advanced Manufacturing Technology*, vol. 108, 2020.

[55] P. Shukla, B. Dash, D. V. Kiran, and S. Bukkapatnam, "Arc behavior in wire arc additive manufacturing process," *Procedia Manufacturing*, vol. 48, pp. 725–729, 2020.

[56] P. Shukla, B. Dash, D. V. Kiran, and S. Bukkapatnam, "Arc behavior in wire arc additive manufacturing process," *EWI*, 2023.

[57] C. Y. Kim, J.-S. Kim, H.-U. Hong, W. Y. Lee, S. Kim, and Y. M. Cho., "Behavior of weld pool convection and columnar-to-equiaxed grain transition in gas tungsten arc welds of ferritic stainless steels with different aluminum contents," *Journal of Materials Processing Technology*, vol. 289, pp. 116946–116946, 2021.

[58] K. Nomura, K. Fukushima, T. Matsumura, and S. Asai, "Burn-through prediction and weld depth estimation by deep learning model monitoring the molten pool in gas metal arc welding with gap fluctuation," *Journal of Manufacturing Processes*, 2020.

[59] M. J. Bermingham, D. Kent, H. Zhan, D. H. StJohn, and M. S. Dargusch, "Controlling the microstructure and properties of wire arc additive manufactured tiâ6alâ4v with trace boron additions," *Acta Materialia*, vol. 91, pp. 289–303, 2015.

[60] A. R. Paul, R. Manivannan, M. Mukherjee, S. Kundu, and A. Chatterjee, "Development of y-shape hybrid frame model using wire and arc additive manufacturing process.," *Materials Today: Proceedings*, vol. 44, pp. 4342–4348, 2021.

[61] P. Liu, L. Huang, L. Gan, and Y. Lei, "Effect of plate thickness on weld pool dynamics and keyhole-induced porosity formation in laser welding of al alloy.," *The International Journal of Advanced Manufacturing Technology*, vol. 111, pp. 735–747, 2020.

[62] X. Fang, H. Li, X. Li, K. Huang, L. Zhang, and B. Lu, "Effect of post heat treatment on the microstructure and mechanical properties of wire-arc additively manufactured a357 alloy components.," *Materials Letters*, vol. 269, 2020.

[63] A. Ortega, L. C. Galvan, F. Deschaux-Beaume, B. Mezrag, and S. Rouquette., "Effect of process parameters on the quality of aluminium alloy al5si deposits in wire and arc additive manufacturing using a cold metal transfer process.," *Science and Technology of Welding and Joining*, vol. 23, 2018.

[64] K. S. Derekar, A. Addison, S. S. Joshi, X. Zhang, J. Lawrence, L. Xu, G. Melton, and D. Griffiths, "Effect of pulsed metal inert gas (pulsed-mig) and cold metal transfer (cmt) techniques on hydrogen dissolution in wire arc additive manufacturing (waam) of aluminium.," *The International Journal of Advanced Manufacturing Technology*, vol. 107, pp. 311–331, 2020.

[65] M. Morakabiyan Esfahani, A. Farzadi, and S. R. Alavi Zaree, "Effect of welding speed on gas metal arc weld pool in commercially pure aluminum: Theoretically and experimentally.," *Russian Journal of Non-Ferrous Metals*, vol. 59, pp. 82–92, 2018.

[66] A. Adebayo, J. Mehnen, and X. Tonnellier, "Effects of solid lubricants on wire and arc additive manufactured structures. proceedings of the institution of mechanical engineers, part b.," *Journal of Engineering Manufacture*, vol. 228, pp. 563–571, 2013.

[67] A. Queguineur, J. Marolleau, A. Lavergne, and G. Ruckert, "Evaluation of tandem controlled short-circuit gmaw for improved deposition in additive manufacture of large nickel aluminium bronze naval components.," *Welding in the World*, vol. 64, pp. 1389–1395, 2020.

[68] H. Wei, H. Bhadeshia, S. A. David, and T. Debroy., "Harnessing the scientific synergy of welding and additive manufacturing.," *Science and Technology of Welding and Joining*, vol. 24, pp. 361–366, 2019.

[69] C. Zhang, C. Shen, X. Hua, F. Li, Y. Zhang, and Y. Zhu, "Influence of wire-arc additive manufacturing path planning strategy on the residual stress status in one single buildup layer.," *The International Journal of Advanced Manufacturing Technology*, vol. 111, pp. 797–806, 2020.

[70] P. Sequeira Almeida and S. Williams, "Innovative process model of ti6al4v additive layer manufacturing using cold metal transfer (cmt).," in *Proceedings of the 21st Annual International Solid Freeform Fabrication Symposium*, 2010.

[71] X. Chen, G. Yu, X. He, and S. Li, "Investigation of thermal dynamics for different leading configuration in hybrid laser-mig welding.," *Optics Laser Technology*, vol. 134, 2021.

[72] C. Lee, W. Woo, J. Baek, and E. Kim, "Laser and arc manufacturing processes: A review.," *International Journal of Precision Engineering and Manufacturing*, vol. 17, pp. 973–985, 2016.

[73] L. Y. . L. S. Han, R., "Macro-micro modeling and simulation for the morphological evolution of the solidification structures in the entire weld.," *International Journal of Heat and Mass Transfer*, vol. 106, pp. 1345–1355, 2017.

[74] A. B. Murphy, F. F. Chen, J. Xiang, H. Wang, D. Thomas, and Y. Feng, "Macrosegregation in the weld pool in metal inert-gas welding of aluminium.," *Journal of Manufacturing Processes*, vol. 61, pp. 111–127, 2021.

[75] O. V. Panchenko, L. A. Zhabrev, D. V. Kurushkin, and A. A. Popovich, "Macrostructure and mechanical properties of AlSi, AlMgSi, and AlMgMn aluminum alloys produced by electric arc additive growth.," *Metal Science and Heat Treatment*, vol. 60, pp. 749–754, 2019.

[76] R. Zhang, X. Tang, L. Xu, F. Lu, and H. Cui, "Mechanism study of thermal fluid flow and weld root hump suppression in full penetration laser welding of al alloy with alternating magnetic field support.," *International Journal of Heat and Mass Transfer*, vol. 166, 2021.

[77] W. E. Frazier, "Metal additive manufacturing: A review.," *Journal of Materials Engineering and Performance*, vol. 23, pp. 1917–1928, 2014.

[78] F. Wang, S. Williams, P. Colegrove, and A. A. Antonysamy, "Microstructure and mechanical properties of wire and arc additive manufactured ti-6al-4v.," *Metallurgical and Materials Transactions*, vol. 44, pp. 968–977, 2012.

[79] P. A. Colegrove, H. E. Coules, J. Fairman, F. Martina, T. Kashoob, H. Mamash, and L. D. Cozzolino, "Microstructure and residual stress improvement in wire

and arc additively manufactured parts through high-pressure rolling.," *Journal of Materials Processing Technology*, vol. 213, pp. 1782–1791, 2013.

[80] G. Zhang, H. Xiong, H. Yu, R. Qin, W. Liu, and H. Yuan, "Microstructure evolution and mechanical properties of wire-feed electron beam additive manufactured ti-5Al-2Sn-2Zr-4Mo-4Cr alloy with different subtransus heat treatments.," *Materials Design*, vol. 195, 2020.

[81] Q. Gao, C. Jin, and Z. Yang, "Morphology and texture characterization of grains in laser welding of aluminum alloys.," *Welding in the World*, vol. 65, pp. 475–483, 2021.

[82] L. Wang, Y. Huang, D. Yang, H. Li, Y. Peng, and K. Wang, "Multi-scale simulation of grain growth during laser beam welding of nickel-based superalloy.," *Journal of Materials Research and Technology*, vol. 9, pp. 15034–15044, 2020.

[83] S. Galjaard, S. Hofman, and S. Ren, "New opportunities to optimize structural designs in metal by using additive manufacturing.," *Advances in Architectural Geometry 2014*, pp. 79–93, 2015.

[84] J. Bai, H. L. Ding, J. L. Gu, X. S. Wang, and H. Qiu, "Porosity evolution in additively manufactured aluminium alloy during high temperature exposure.," in *IOP Conference Series: Materials Science and Engineering*, 2017.

[85] S. Galjaard, S. Hofman, and S. Ren, "Practical case of rapid prototyping using gas metal arc welding.," 1994.

[86] A. B. Murphy and D. G. Thomas, "Prediction of arc, weld pool and weld properties with a desktop computer model of metalâinert-gas welding.," *Welding in the World*, vol. 61, pp. 623–633, 2017.

[87] J. Reimann, P. Henckell, Y. Ali, S. Hammer, A. Rauch, J. Hildebrand, and J. P. Bergmann, "Production of topology-optimised structural nodes using arc-based, additive manufacturing with gmaw welding process.," *Journal of Civil Engineering and Construction*, vol. 10, pp. 101–107, 2021.

[88] J. Reimann, P. Henckell, Y. Ali, S. Hammer, A. Rauch, J. Hildebrand, and J. P. Bergmann, "Additive manufacturing for large-scale metal components, development and deployment of metal big area-additive-manufacturing," 2016.

[89] M. Bahr, J. Buhl, G. Radow, J. D. Schmidt, M. Bambach, M. BreuÃ, and A. FÃŒgenschuh., "Stable honeycomb structures and temperature based trajectory optimization for wire-arc additive manufacturing.," *Optimization and Engineering*, vol. 22, pp. 913–974, 2020.

[90] C. R. Cunningham, J. M. Flynn, A. Shokrani, V. Dhokia, and S. T. Newman, "Invited review article: Strategies and processes for high quality wire arc additive manufacturing.," *Additive Manufacturing*, vol. 22, pp. 672–686, 2018.

[91] A. Farzadi, M. M. Esfahani, and R. Alavi, "Theoretical and experimental investigation of gas metal arc weld pool in commercially pure aluminum: Effect of welding current on geometry.," *Journal of Central South University*, vol. 24, pp. 2556–2564, 2017.

[92] D. Klobcar, S. Balos, M. Basic, A. Djuric, M. Lindic, and A. Scetinec, "Waam and other unconventional metal additive manufacturing technologies.," *Advanced Technologies Materials*, vol. 45, pp. 1–9, 2020.

[93] X. Cao, M. Jahazi, J. P. Immarigeon, and W. Wallace, "A review of laser welding techniques for magnesium alloys.," *Journal of Materials Processing Technology*, vol. 171, pp. 188–204, 2006.

[94] S. Liu and H. Guo, "A review of slmed magnesium alloys: Processing, properties, alloying elements and postprocessing.," *Metals*, vol. 10, 2020.

[95] N. Sezer, Z. Evis, and M. KoÃ§, "Additive manufacturing of biodegradable magnesium implants and scaffolds: Review of the recent advances and research trends.," *Journal of Magnesium and Alloys*, vol. 9, pp. 392–415, 2020.

[96] R. Karunakaran, S. Ortgies, A. Tamayol, F. Bobaru, and M. P. Sealy, "Additive manufacturing of magnesium alloys.," *Bioactive Materials*, vol. 5, pp. 44–54, 2020.

[97] D. Lu, Y. Huang, Q. Jiang, M. Zheng, J. Duan, and B. Hou, "An approach to fabricating protective coatings on a magnesium alloy utilising alumina.," *Surface and Coatings Technology*, vol. 367, pp. 336–3404, 2019.

[98] F. Qian, "Current research situation and prospect for thermoplastic molding technology of az series magnesium alloys.," in *Proceedings of the 2018 3rd International Workshop on Materials Engineering and Computer Sciences*, 2018.

[99] X. C. Luo, L. M. Kang, H. L. Liu, Z. J. Li, Y. F. Liu, D. T. Zhang, and D. L. Chen, "Enhancing mechanical properties of az61 magnesium alloy via friction stir processing: Effect of processing parameters.," *Materials Science and Engineering: A*, vol. 797, 2020.

[100] S. Saini, J. S. Chohan, and K. S. Boparai, "Evaluating the microstructural characteristics in friction stir welding of magnesium az61a alloy.," in *Materials Today: Proceedings*, pp. 1762–1768, 2022.

[101] S. Rajakumar, V. Balasubramanian, and A. Razalrose, "Friction stir and pulsed current gas metal arc welding of az61a magnesium alloy: A comparative study.," *Materials Design*, vol. 49, pp. 267–278, 2013.

[102] L. Commin, M. Dumont, J. Masse, and L. Barrallier, "Friction stir welding of az31 magnesium alloy rolled sheets: Influence of processing parameters.," *Acta Materialia*, vol. 57, pp. 326–334, 2009.

[103] J. Song, J. She, D. Chen, and F. Pan, "Latest research advances on magnesium and magnesium alloys worldwide.," *Journal of Magnesium and Alloys*, vol. 8, pp. 1–41, 2020.

[104] S. V. Gnedenkov, S. L. Sinebryukhov, V. S. Egorkin, D. V. Mashtalyar, I. E. Vyaliy, K. V. Nadaraia, I. Imshinetskiy, A. I. Nikitin, E. P. Subbotin, and A. S. Gnedenkov, "Magnesium fabricated using additive technology: Specificity of corrosion and protection.," *Journal of Alloys and Compounds*, vol. 808, pp. 151629–151629, 2019.

[105] X. L. Luo, D. Zhang, W. Zhang, C.-W. Qiu, and D. Chen, "Tensile properties of az61 magnesium alloy produced by multi-pass friction stir processing: Effect of sample orientation.," *Materials Science and Engineering: A*, vol. 725, pp. 398–405, 2018.

[106] H. Shen, J. Yan, and X. Niu, "Thermo-fluid-dynamic modeling of the melt pool during selective laser melting for az91d magnesium alloy.," *Materials*, vol. 13, 2020.

[107] X. L. Luo, D. Zhang, W. Zhang, C.-W. Qiu, and D. Chen, "Tensile properties of az61 magnesium alloy produced by multi-pass friction stir processing: Effect of sample orientation.," *Materials Science and Engineering: A*, vol. 725, pp. 398–405, 2018.

[108] X. L. Luo, D. Zhang, W. Zhang, C.-W. Qiu, and D. Chen, "Tensile properties of az61 magnesium alloy produced by multi-pass friction stir processing: Effect of sample orientation.," *Materials Science and Engineering: A*, vol. 725, pp. 398–405, 2018.

[109] S. Gneiger, J. A. Ãsterreicher, A. R. Arnoldt, A. Birgmann, and M. Fehlbier, "Development of a high strength magnesium alloy for wire arc additive manufacturing.," *Metals*, vol. 10, 2020.

[110] X. Luo, G. Cao, W. Zhang, C. Qiu, and D. Zhang, "Ductility improvement of an az61 magnesium alloy through two-pass submerged friction stir processing.," *Materials*, vol. 10, 2017.

[111] X. Chai, Y. Yang, B. Carlson, and S. Kou, "Gas metal arc welding of magnesium alloys: Oxide films, high crowns, and fingers.," *Welding journal*, vol. 94, 2015.

[112] S. Liu, W. Yang, X. Shi, B. Li, S. Duan, H. Guo, and J. Guo, "Latest research advances on magnesium and magnesium alloys worldwide," *Journal of Magnesium and Alloys*, vol. 808, 2019.

[113] J. Song, J. She, D. Chen, and F. Pan, "Experimental investigation on improving the deposition rate of gas metal arc-based additive manufacturing by auxiliary wire feeding method.," *Journal of Magnesium and Alloys*, vol. 8, pp. 1–41, 2020.

[114] C. R. Ng, M. M. Savalani, H. C. Man, and I. R. Gibson, "Layer manufacturing of magnesium and its alloy structures for future applications," *Virtual and Physical Prototyping*, vol. 5, pp. 13–19, 2010.

[115] X. Chai, "Liquation and liquation cracking in partially melted zones of magnesium welds.," *Welding Journal*, 2016.

[116] J. Bi, J. Shen, S. Hu, Y. Zhen, F. Yin, and X. Bu, "Microstructure and mechanical properties of az91 mg alloy fabricated by cold metal transfer additive manufacturing.," *Materials Letters*, vol. 276, pp. 128185–128185, 2020.

[117] Y. Guo, H. Pan, L. Ren, and G. Quan, "Microstructure and mechanical properties of wire arc additively manufactured az80m magnesium alloy.," *Materials Letters*, vol. 247, pp. 4–6, 2019.

[118] M. Rethmeier, B. Kleinpeter, and H. Wohlfahrt, "Mig welding of magnesium alloys metallographic aspects," *Welding in the World*, vol. 48, pp. 28–33, 2004.

[119] Z. Wang, J. Wei, and L. Wang, "Optimization of current parameters during variable polarity gmaw of magnesium alloy.," *Modern Physics Letters B*, vol. 33, 2019.

[120] G.-W. Song and P. Wang, "Pulsed mig welding of az31b magnesium alloy.," *Materials Science and Technology*, vol. 27, pp. 518–524, 2011.

[121] Y. Yang, X. Xiong, J. Chen, X. Peng, D. Chen, and F. Pan, "Research advances in magnesium and magnesium alloys worldwide in 2020," *Journal of Magnesium and Alloys*, vol. 9, pp. 705–747, 2020.

[122] G.-W. Song, P. Wang, and L. Liu, "Study on ac-pmig welding of az31b magnesium alloy.," *Science and Technology of Welding and Joining*, vol. 15, pp. 219–225, 2010.

[123] L. Liu, *Welding and joining of magnesium alloys.* Woodhead Publishing in Materials, 2010.

[124] P. Wang, H. Zhang, H. Zhu, Q. Li, and M. Feng, "Wire-arc additive manufacturing of az31 magnesium alloy fabricated by cold metal transfer heat source: Processing, microstructure, and mechanical behavior.," *Journal of Materials Processing Technology*, vol. 288, 2021.

[125] S. Patel, P. Reddy, and A. Kumar, "A methodology to integrate melt pool convection with rapid solidification and undercooling kinetics in laser spot welding," *International Journal of Heat and Mass Transfer*, vol. 164, 2021.

[126] Y. Li, C. Su, X. Zhou, and C. Wu, "A more precise unified model to describe comprehensive multiphysics and multiphase phenomena in plasma arc welding," *Journal of Manufacturing Processes*, vol. 59, pp. 668–678, 2020.

[127] S. H. Nikam, J. Quinn, and S. McFadden, "A simplified thermal approximation method to include the effects of marangoni convection in the melt pools of processes that involve moving point heat sources," *Numerical Heat Transfer, Part A: Applications*, vol. 79, pp. 537–552, 2021.

[128] A. Ebrahimi, C. R. Kleijn, and I. G. Richardson, "A simulation-based approach to characterise melt-pool oscillations during gas tungsten arc welding," *International Journal of Heat and Mass Transfer*, vol. 164, pp. 120535–120535, 2021.

[129] A. R. Lawrence and P. Michaleris, "Effects of thermal transport in computation of welding residual stress and distortion," *Science and Technology of Welding and Joining*, vol. 16, pp. 215–220, 2011.

[130] S. Marimuthu, D. Clark, J. W. Allen, A. M. Kamara, P. Mativenga, L. Li, and R. Scudamore, "Finite element modelling of substrate thermal distortion in direct laser additive manufacture of an aero-engine component," in *Proceedings of the Institution of Mechanical Engineers, Part C: Journal of Mechanical Engineering Science*, 2012.

[131] M. Grujicic, A. Arakere, S. Ramaswami, J. S. Snipes, R. Yavari, C.-F. Yen, B. A. Cheeseman, and J. S. Montgomery, "Gas metal arc welding process modeling and prediction of weld microstructure in mil a46100 armor-grade martensitic steel," *Journal of Materials Engineering and Performance*, vol. 22, pp. 1541–1557, 2012.

[132] X. Wang, J. Huang, Y. Huang, D. Fan, and Y. Guo, "Investigation of heat transfer and fluid flow in activating tig welding by numerical modeling," *Applied Thermal Engineering*, vol. 113, pp. 27–35, 2017.

[133] P. Jiang, S. Gao, S. Geng, C. Han, and G. Mi, "Multi-physics multi-scale simulation of the solidification process in the molten pool during laser welding of aluminum alloys," *International Journal of Heat and Mass Transfer*, vol. 161, 2020.

[134] Y. Saadlaoui, A. Delache, E. Feulvarch, J.-B. Leblond, and J.-M. Bergheau, "New strategy of solid/fluid coupling during numerical simulation of thermo-mechanical processes," *Journal of Fluids and Structures*, vol. 99, pp. 103161–103161, 2020.

[135] D. Wang and H. Lu, "Numerical analysis of internal flow of molten pool in pulsed gas tungsten arc welding using a fully coupled model with free surface," *International Journal of Heat and Mass Transfer*, vol. 165, 2021.

[136] O. Mokrov, O. Lysnyi, M. Simon, U. Reisgen, G. Laschet, and M. Apel, "Numerical investigation of droplet impact on the welding pool in gas metal arc welding," *Materialwissenschaft und Werkstofftechnik*, 2018.

[137] L. Li, B. Li, L. Liu, and Y. Motoyama, "Numerical modeling of fluid flow, heat transfer and arcâmelt interaction in tungsten inert gas welding," *High Temperature Materials and Processes*, vol. 36, pp. 427–439, 2017.

[138] S. Zhang, G. Ma, X. Peng, and Y. Xiang, "Numerical simulation of the effects of bypass current on droplet transfer during az31b magnesium alloy de-gmaw process based on fluent," *The International Journal of Advanced Manufacturing Technology*, vol. 90, pp. 857–863, 2016.

[139] H. Jing, P. Ge, Z. Zhang, J. Chen, Z. Liu, and W. Liu, "Numerical studies of the effects of the substrate structure on the residual stress in laser directed energy additive manufacturing of thin-walled products," *Metals*, vol. 12, pp. 462–462, 2022.

[140] D. Wang and H. Lu, "Numerical analysis of internal flow of molten pool in pulsed gas tungsten arc welding using a fully coupled model with free surface," *International Journal of Heat and Mass Transfer*, vol. 165, pp. 120572–120572, 2021.

[141] C. Wang, X. Yu, M. Jiang, Z. Xing, and C. Wang, "Numerical and experimental investigation into the evolution and distribution of residual stress in laser transmission welding of pc/cu/pc," *Optics Laser Technology*, vol. 136, 2021.

[142] M. Ohno and K. Matsuura, "Quantitative phase-field modeling for dilute alloy solidification involving diffusion in the solid," *Physical Review E*, vol. 79, 2009.

[143] P. Michaleris, "Modeling metal deposition in heat transfer analyses of additive manufacturing processes," *Finite Elements in Analysis and Design*, vol. 86, pp. 51–60, 2014.

[144] J.-S. Kim, D. Van, J. Lee, J. Yim, and S. H. Lee, "The effect of a hot-wire in the tandem gmaw process ascertained by developing a multiphysics simulation model," *Journal of Mechanical Science and Technology*, vol. 35, pp. 267–273, 2021.

[145] T. Kaneko and M. Suzuki, "Automotive applications of magnesium alloys. materials science forum," *Materials Science Forum*, pp. 419–422, 2003.

[146] K. Hirai, H. Somekawa, Y. Takigawa, and K. Higashi, "Effects of ca and sr addition on mechanical properties of a cast az91 magnesium alloy at room and elevated temperature," *Materials Science and Engineering A-Structural Materials Properties Microstructure and Processing*, vol. 403, pp. 276–280, 2005.

[147] Y. Uematsu, K. Tokaji, M. Kamakura, K. Uchida, H. Shibata, and N. Bekku., "Effect of extrusion conditions on grain refinement and fatigue behaviour in magnesium alloys.," *Materials Science and Engineering: A*, vol. 434, pp. 131–140, 2006.

[148] D. Mao, B. Zhang, J. Li, Z. Li, and C. Shi, “Effect of hot-rolling and warm-rolling process on properties of cast-rolling az31b magnesium alloy strip,” in *Procedia Engineering 27*, 2012.

[149] S.-J. Huang, M. Subramani, and C.-C. Chiang, “Effect of hybrid reinforcement on microstructure and mechanical properties of az61 magnesium alloy processed by stir casting method,” *Composites Communications*, vol. 25, 2021.

[150] T. S. Shih, B. Liu, and Y.-J. Chen, “Fatigue of as-extruded az61a magnesium alloy,” *Materials Science and Engineering: A*, vol. 325, pp. 152–162, 2002.

[151] Z. Li, Q. Wang, A. A. Luo, P. Fu, and L. Peng, “Fatigue strength dependence on the ultimate tensile strength and hardness in magnesium alloys,” *International Journal of Fatigue*, vol. 80, pp. 468–476, 2015.

[152] Q. Chen, D. Shu, C. Hu, Z. Zhao, and B. Yuan, “Grain refinement in an as-cast az61 magnesium alloy processed by multi-axial forging under the multitemperature processing procedure,” *Materials Science and Engineering: A*, vol. 541, pp. 98–104, 2012.

[153] T. Yokoyama, “Impact tensile stressâstrain characteristics of wrought magnesium alloys,” *Strain*, vol. 39, pp. 167–175, 2003.

[154] Z. Zeng, N. Stanford, C. H. J. Davies, J.-F. Nie, and N. Birbilis, “Magnesium extrusion alloys: a review of developments and prospects,” *International Materials Reviews*, vol. 64, pp. 27–62, 2018.

[155] T. Xu, Y. Yang, X. Peng, J. Song, and F. Pan, “Overview of advancement and development trend on magnesium alloy,” *Journal of Magnesium and Alloys*, vol. 7, pp. 536–544, 2019.

[156] H. Pan, Y. Ren, H. Fu, H. Zhao, L. Wang, X. Meng, and G. Qin, “Recent developments in rare-earth free wrought magnesium alloys having high strength: A review,” *Journal of Alloys and Compounds*, vol. 663, pp. 321–331, 2016.

[157] H. Friedrich and S. Schumann, “Research for a ânew age of magnesiumâ in the automotive industry,” *Journal of Materials Processing Technology*, vol. 117, pp. 276–281, 2001.

[158] J. Hirsch and T. Al-Samman, “Superior light metals by texture engineering: Optimized aluminum and magnesium alloys for automotive applications,” *Acta Materialia*, vol. 61, pp. 818–843, 2013.

[159] P. Fu, L. Peng, H. Jiang, W. Ding, and X. Zhai, “Tensile properties of high strength cast mg alloys at room temperature: A review,” *China Foundry*, vol. 11, pp. 277–286, 2014.

[160] M. J. Assael, K. Kakosimos, R. M. Banish, J. Brillo, I. Egry, R. Brooks, P. N. Quested, K. C. Mills, S. Y. Nagashima, A., and W. A. Wakeham, "Reference data for the density and viscosity of liquid aluminum and liquid iron," *Journal of Physical and Chemical Reference Data*, vol. 35, pp. 285–300, 2006.

[161] M. Guanbao, A. V. Okhapkin, S. Konstantinova, P. S. A. N., Popel, and L. Pytsze, "Kinematic viscosity of mg-al melts in the magnesium-rich portion," *Russian Metallurgy (Metally)*, vol. 2013, pp. 90–95, 2013.

[162] G. D. Janaki Ram, R. Murugesan, and S. Sundaresan, "Fusion zone grain refinement in aluminum alloy welds through magnetic arc oscillation and its effect on tensile behavior," *Journal of Materials Engineering and Performance*, vol. 8, pp. 513–520, 1999.

[163] G. D. Janaki Ram, R. Murugesan, and S. Sundaresan, "Fusion zone grain refinement in aluminum alloy welds through magnetic arc oscillation and its effect on tensile behavior," *Journal of Materials Engineering and Performance*, vol. 8, pp. 513–520, 1999.

[164] R. D. Ardika, T. Triyono, N. Muhayat, and Triyono, "A review porosity in aluminum welding," in *Procedia Structural Integrity*, 2021.

[165] L. Wang, Y. Liu, C. Yang, and M. Gao, "Study of porosity suppression in oscillating laser-mig hybrid welding of aa6082 aluminum alloy," *Journal of Materials Processing Technology*, vol. 292, pp. 117053–117053, 2021.

APPENDIX A: Stable arc output measurements for high and low-IER

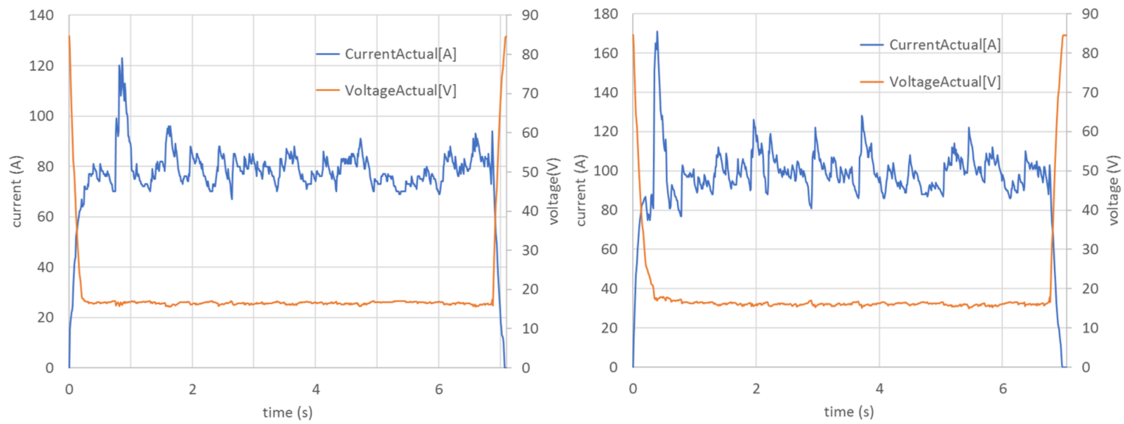

Figure A.1: Stable outputs with low-IER set current/voltage of 130A/15V (left) and set current/voltage of 165A/13V (right).

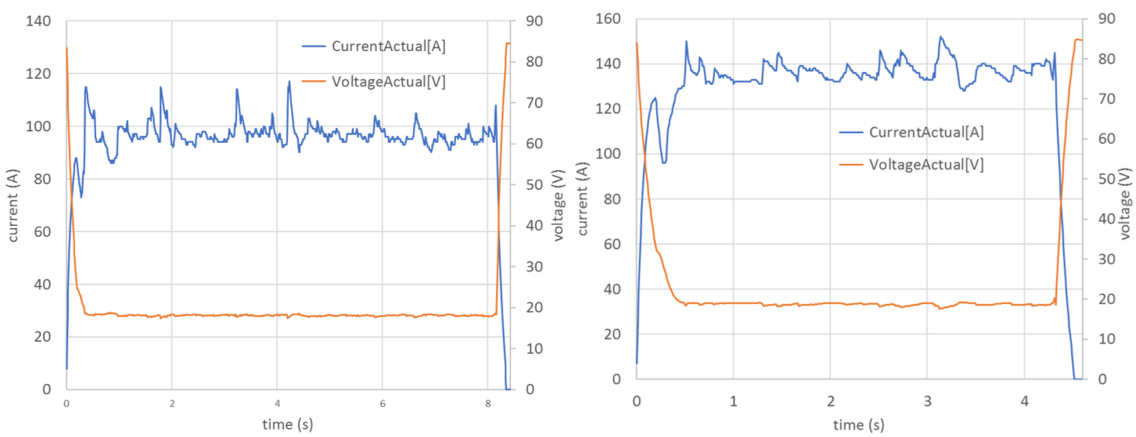

Figure A.2: Stable outputs with low-IER set current/voltage of 165A/15V (left) and high-IER set current/voltage of 220A/15V (right).

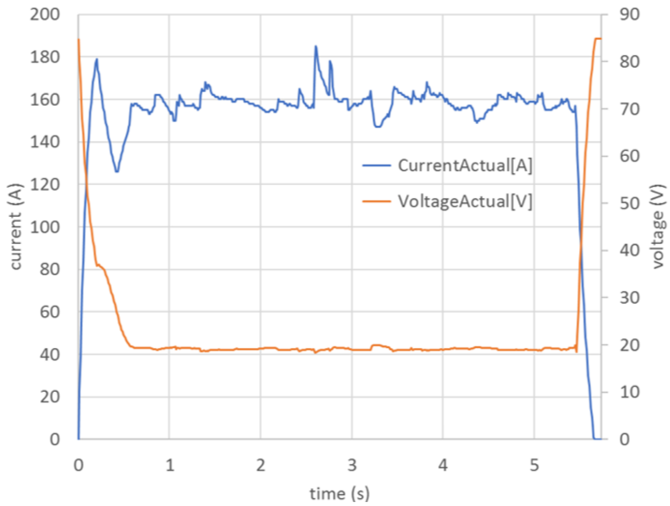

Figure A.3: Stable outputs with high-IER set current/voltage of 250A/15V.

APPENDIX B: Unstable arc output measurements for hi and low-IER

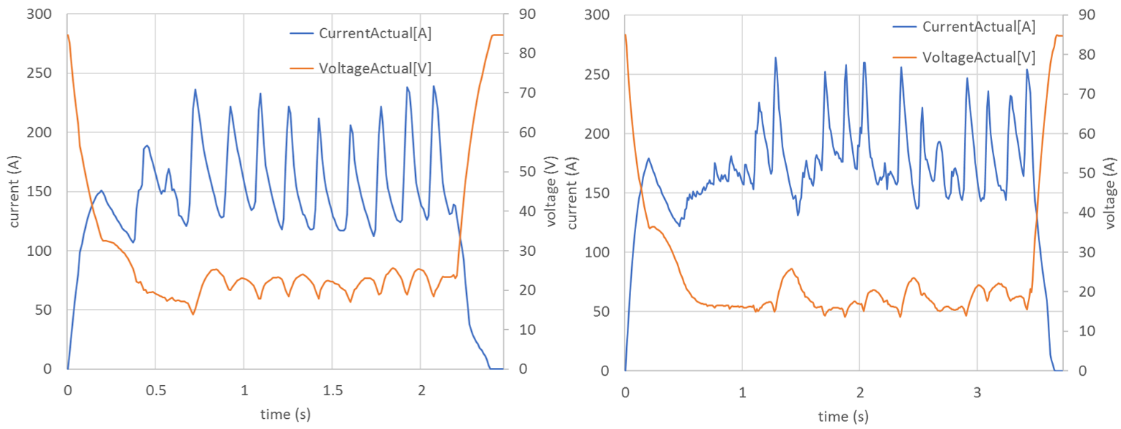

Figure B.1: Unstable outputs with high-IER set current/voltage of 220A/11V (left) and high-IER set current/voltage of 250A/11V (right).

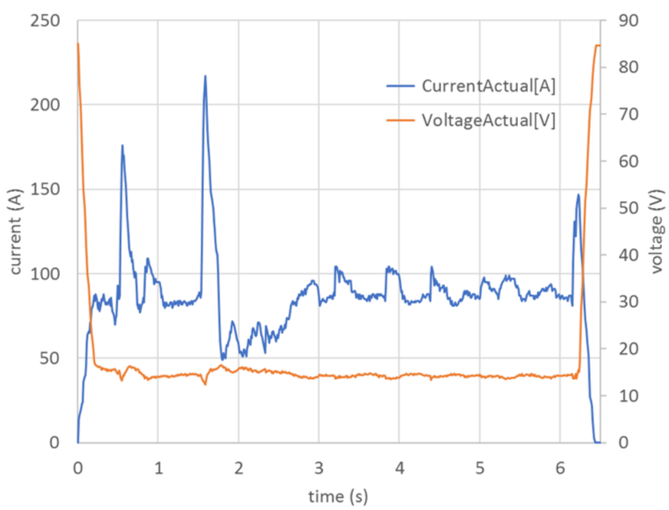

Figure B.2: Initial pushback causing start instability in low-IER set current/voltage of 130A/13V.

APPENDIX C: Supplemental SEM images and micrographs

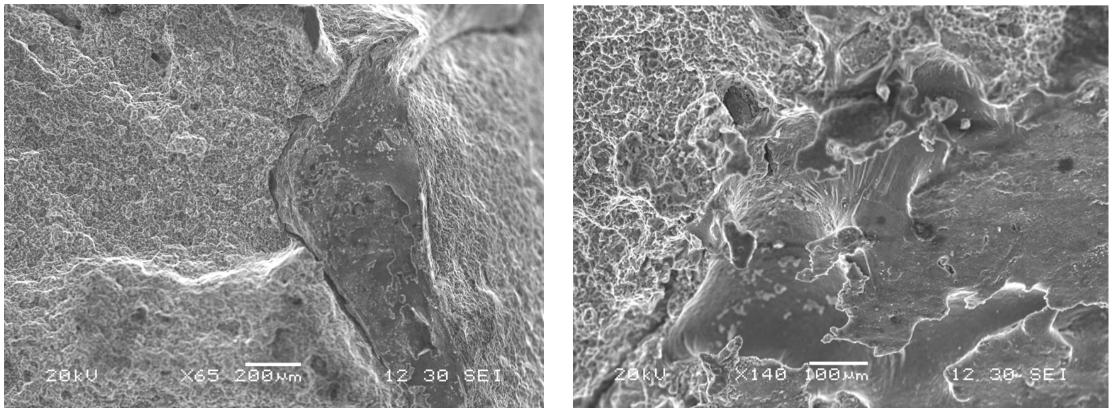

Figure C.1: Unfused regions of the fracture zone from tensile tests.

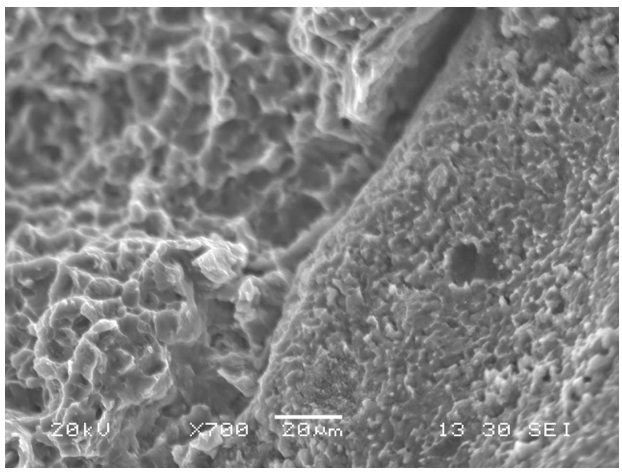

Figure C.2: Transition-zone between fused and unfused fracture surface.

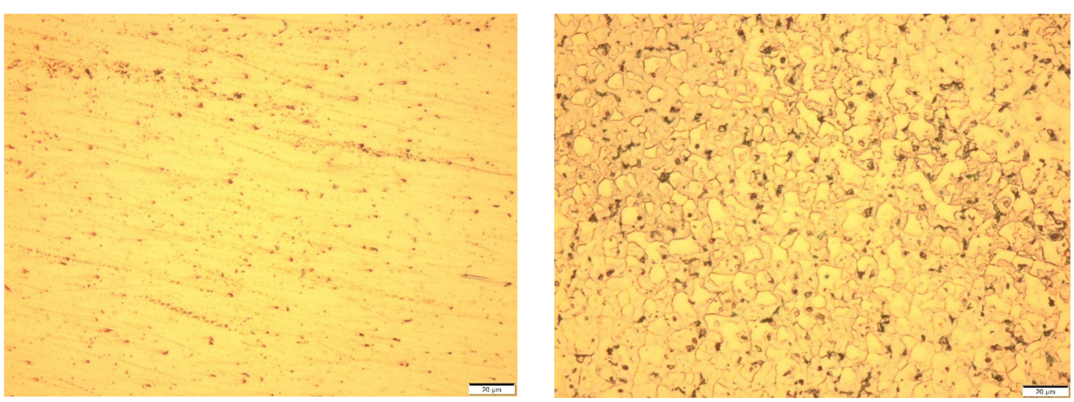

Figure C.3: Micrographs of MRML blocks before and after etching with 4% Nital for 10 s.

APPENDIX D: CAD Model of GMAW-CNC

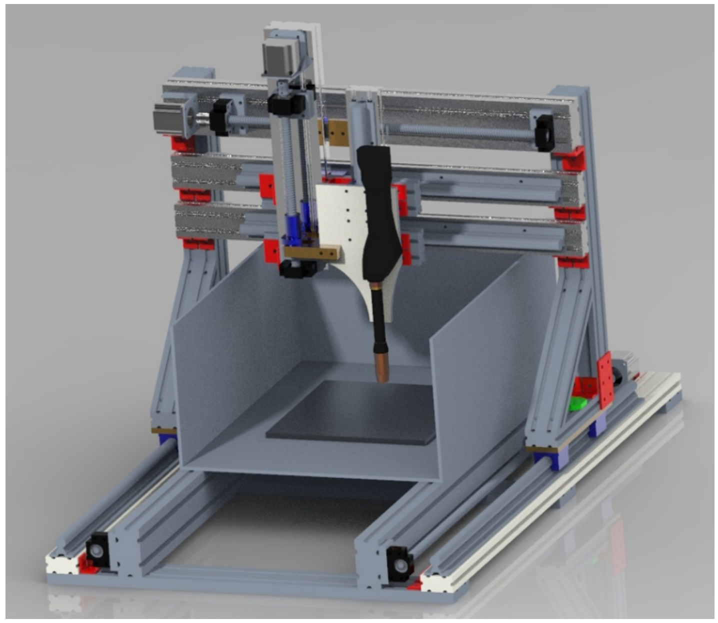

Figure D.1: CAD model of GMAW-CNC â front view.

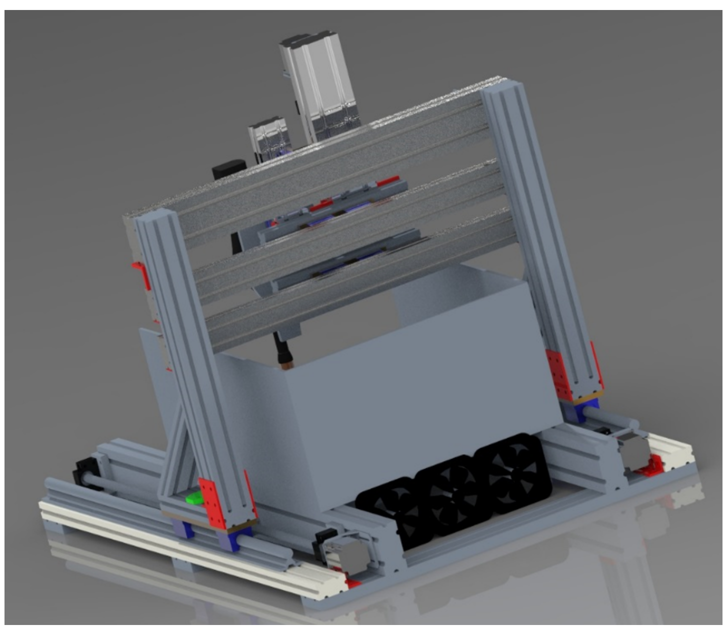

Figure D.2: CAD model of GMAW-CNC â rear view.

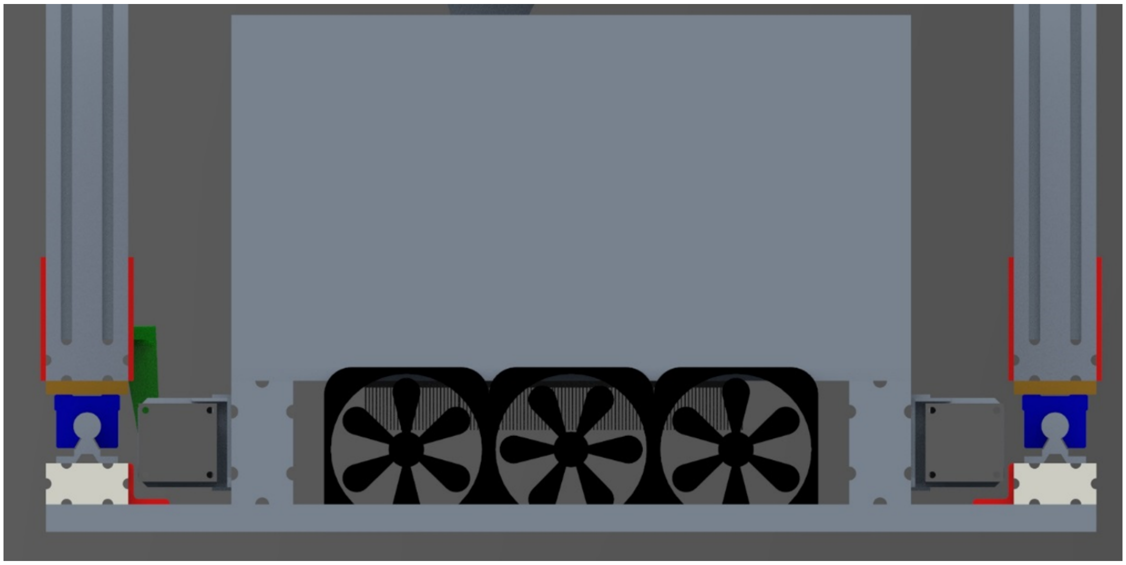

Figure D.3: CAD model of fan-array with heat sinks.

APPENDIX E: Spatter in high-IER deposition

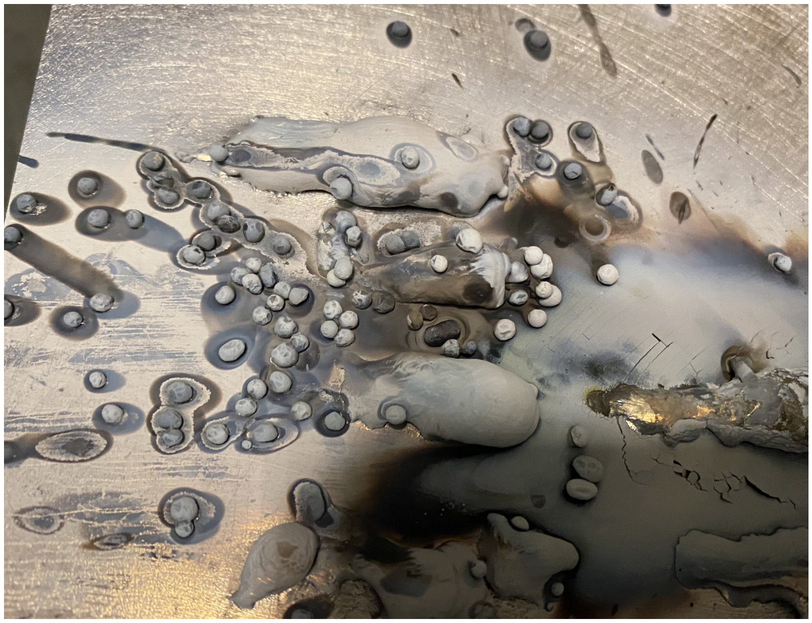

Figure E.1: DC-pulse severe spatter during weld bead deposition.

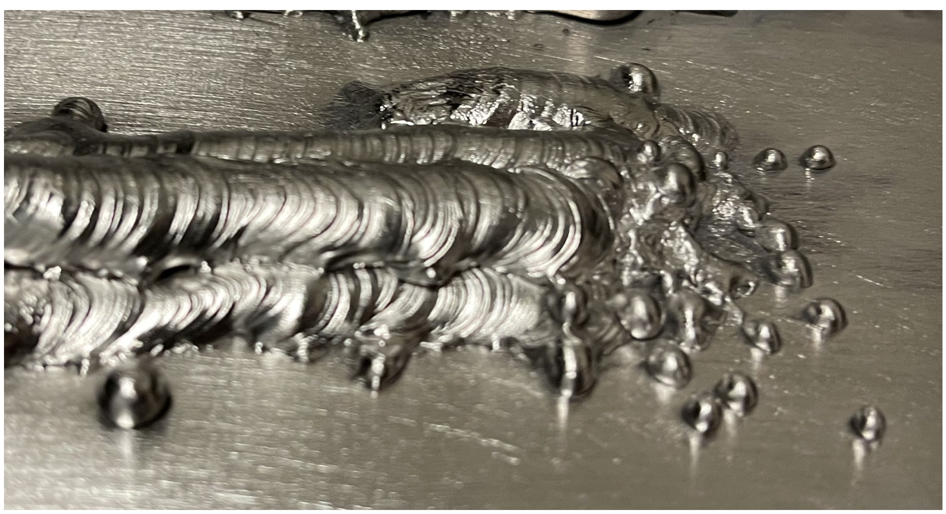

Figure E.2: DC spatter at very high-IER parameters.

APPENDIX F: Wall vs block heat transfer rates

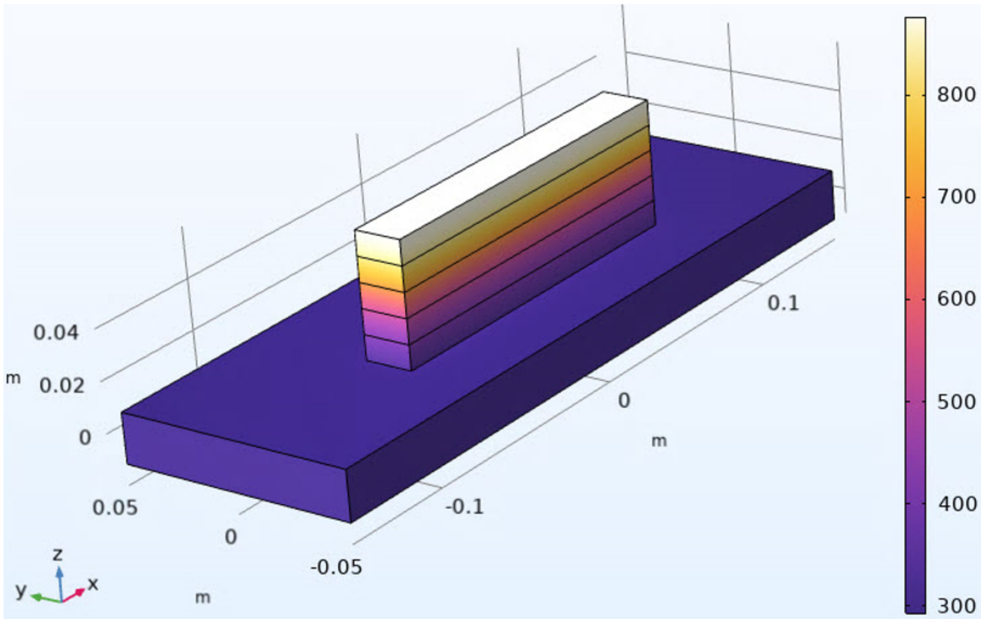

Figure F.1: Wall temperature profile 2 seconds after deposition of 1500 K bead.

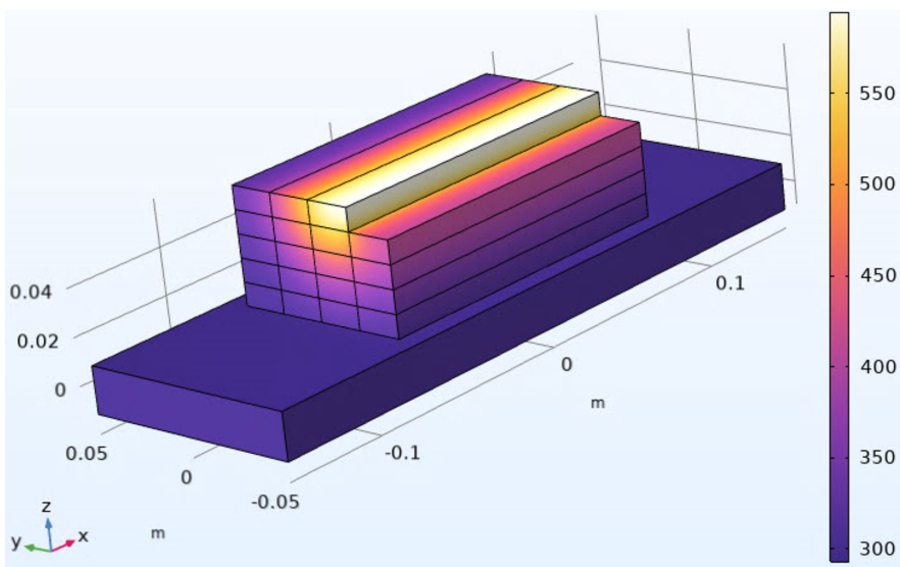

Figure F.2: Block temperature profile 2 seconds after deposition of 1500 K bead.

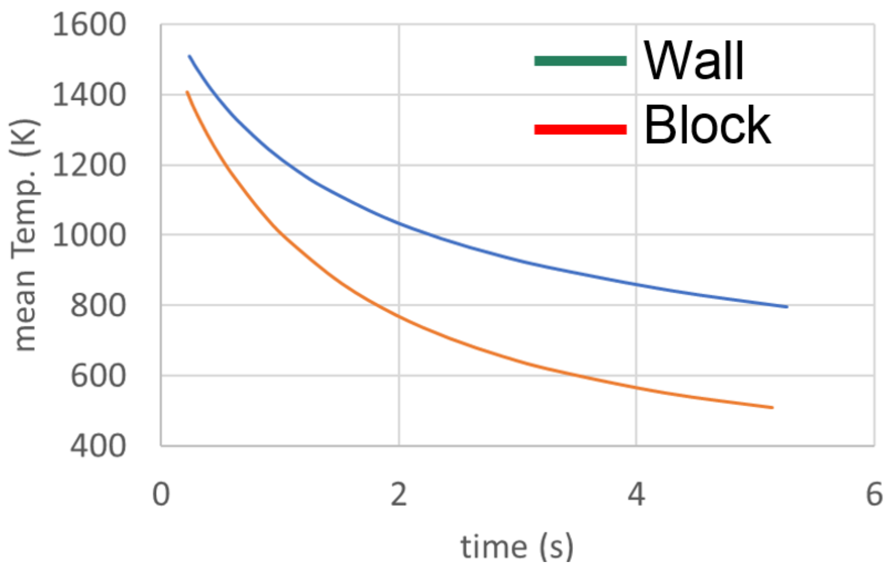

Figure F.3: Mean temperature of newly deposited beads versus time, demonstrating the large difference in cooling rate between wall like structures and thicker block structures.